

One-Dimensional Optical Wave Turbulence: Experiment and Theory

Jason Laurie^{a,*}, Umberto Bortolozzo^b, Sergey Nazarenko^c, Stefania Residori^b

^a*Laboratoire de Physique, École Normale Supérieure de Lyon, 46 allée d'Italie, Lyon, 69007, France*

^b*INLN, Université de Nice, Sophia-Antipolis, CNRS, 1361 route des Lucioles, 06560, Valbonne, France*

^c*Mathematics Institute, University of Warwick, Coventry CV4 7AL, United Kingdom*

Abstract

We present a review of the latest developments in one-dimensional (1D) optical wave turbulence (OWT). Based on an original experimental setup that allows for the implementation of 1D OWT, we are able to show that an inverse cascade occurs through the spontaneous evolution of the nonlinear field up to the point when modulational instability leads to soliton formation. After solitons are formed, further interaction of the solitons among themselves and with incoherent waves leads to a final condensate state dominated by a single strong soliton. Motivated by the observations, we develop a theoretical description, showing that the inverse cascade develops through six-wave interaction, and that this is the basic mechanism of nonlinear wave coupling for 1D OWT. We describe theory, numerics and experimental observations while trying to incorporate all the different aspects into a consistent context. The experimental system is described by two coupled nonlinear equations, which we explore within two wave limits allowing for the expression of the evolution of the complex amplitude in a single dynamical equation. The long-wave limit corresponds to waves with wave numbers smaller than the electrical coherence length of the liquid crystal, and the opposite limit, when wave numbers are larger. We show that both of these systems are of a dual cascade type, analogous to two-dimensional (2D) turbulence, which can be described by wave turbulence (WT) theory, and conclude that the cascades are induced by a six-wave resonant interaction process. WT predicts several stationary solutions (non-equilibrium and thermodynamic) to both the long- and short-wave systems, and we investigate the necessary conditions required for their realization. Interestingly, the long-wave system is close to the integrable 1D nonlinear Schrödinger equation (NLSE) (which contains exact nonlinear soliton solutions), and as a result during the inverse cascade, nonlinearity of the system at low wave numbers becomes strong. Subsequently, due to the focusing nature of the nonlinearity, this leads to modulational instability (MI) of the condensate and the formation of solitons. Finally, with the aid of the probability density function (PDF) description of WT theory, we explain the coexistence and mutual interactions between solitons and the weakly nonlinear random wave background in the form of a wave turbulence life cycle (WTLC).

Keywords: Nonlinear optics, liquid crystals, turbulence, integrability, solitons

Contents

1	Introduction	4
2	The Experiment	8
2.1	Description of the Experimental Setup	8
2.2	The Evolution of the Light Intensity and the Inverse Cascade	10
2.3	The Long Distance Evolution and Soliton Formation	12
2.4	The Probability Density Function of the Intensity	14
2.5	The Relation to Previous Studies of Optical Solitons	15
2.6	The Theoretical Model of the OWT Experiment	16
2.6.1	The Long-Wave Regime	17
2.6.2	The Short-Wave Regime	17
2.7	The Nonlinearity Parameter	18
2.8	The Hamiltonian Formulation	18
2.9	The Canonical Transformation	20
3	Wave Turbulence Theory	22
3.1	Solutions for the One-Mode PDF: Intermittency	24
3.2	Solutions of the Kinetic Equation	24
3.3	Dual Cascade Behavior	25
3.4	The Zakharov Transform and the Power-Law Solutions	26
3.5	Locality of the Kolmogorov-Zakharov Solutions	29
3.6	Logarithmic Correction to the Direct Energy Spectrum	30
3.7	Linear and Nonlinear Times and The Critical Balance Regime	31
3.8	The Differential Approximation and the Cascade Directions	32
3.9	Modulational Instability and Solitons in the Long-Wave Equation	33
4	Numerical results and comparison with the experiment	39
4.1	The Numerical Method	39
4.2	The Long-Wave Equation	41
4.2.1	The Decaying Inverse Cascade with Condensation	41
4.2.2	The PDF of the light intensity	44
4.2.3	The $k - \omega$ Plots: Solitons and Waves	44
4.2.4	Forced and Dissipated Simulations	53
4.3	The Short-Wave Equation	59
5	Conclusions	62
6	Acknowledgements	65
	Appendices	66

*Corresponding author

Email addresses: `jason.laurie@ens-lyon.fr` (Jason Laurie), `umberto@gmail.com` (Umberto Bortolozzo), `s.v.nazarenko@warwick.ac.uk` (Sergey Nazarenko), `stefania.residori@inln.cnrs.fr` (Stefania Residori)

A	The Canonical Transformation	66
B	Details and Assumptions of Weak Wave Turbulence	
Theory		69
B.1	The Weak Nonlinearity Expansion	70
B.2	Equation for the Generating Functional	72
C	The Zakharov Transform	75
D	Expansion of the Long-Wave Six-Wave Interaction Co-	
efficient		76
E	Locality of the Kinetic Equation Collision Integral	77
F	Derivation of the Differential Approximation Model	79
G	The Bogoliubov Dispersion Relation	80
H	Non-Dimensionalization	81
I	The Intensity Spectrum	82
Bibliography		84

1. Introduction

One-dimensional (1D) optical wave turbulence (OWT) is an extremely interesting physical phenomenon whose importance arises from its intrinsic overlap with several strategic research areas. This interdisciplinary nature allows for the application of non-conventional approaches to familiar facts and routes. These areas include wave turbulence (WT), Bose-Einstein condensate (BEC) and lasing, integrable systems and solitons, and, on a more fundamental level, general turbulence, nonlinear optics, equilibrium and non-equilibrium statistical mechanics. A hierarchical diagram showing these areas and their links to 1D OWT is shown in figure 1.

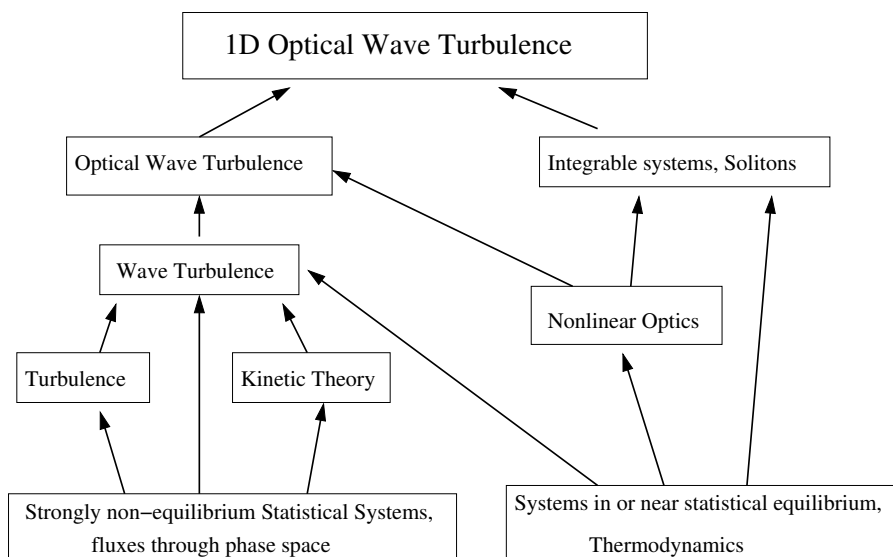


Figure 1: Interconnections of 1D OWT with other research areas.

The main aspects and phenomena in 1D OWT which will be at the focus of the present review include:

- The inverse transfer of wave action (from short to long wave lengths), its relation to the BEC of light, and to WT as an active medium for lasing;
- The role of turbulent cascades (fluxes) versus thermodynamic potentials (temperature and chemical potential) in 1D OWT and in WT in general;
- The proximity to integrability, modulational instability (MI) and the generation of solitons;
- The coexistence, interactions and mutual transformations of random waves and solitons: this constitutes the wave turbulence life cycle (WTLC) and the evolution towards a final single soliton state.

Since WT concepts are central for our review, we will begin by giving a brief introduction to WT. WT can be generally defined as a random set of interacting waves with

a wide range of wave lengths. WT theory has been applied to several physical systems including water surface gravity and capillary waves in oceans [1, 2, 3, 4, 5, 6, 7, 8, 9, 10, 11, 12, 13, 14, 15, 16]; internal, inertial, and Rossby waves in atmospheres and oceans [17, 18, 19, 20, 21, 22, 23, 24, 25]; Alfvén waves in solar wind and interstellar turbulence [26, 27, 28, 29, 30, 31, 32, 33, 34, 35, 36, 37]; Kelvin waves on quantized vortex lines in superfluid helium [38, 39, 40, 41, 42, 43, 44, 45, 46]; waves in BECs and nonlinear optics [47, 48, 49, 50, 51]; waves in fusion plasmas [52, 53, 54, 3]; and waves on vibrating, elastic plates [55]. A thorough and detailed list of examples where the WT approach has been applied, from quantum to astrophysical scales, can be found in the recent book [56]. The most developed part of the WT theory assumes that waves have random phases and amplitudes and that their interactions are weakly nonlinear [3, 56], in which case a natural asymptotic closure arises for the statistical description of WT. The most familiar outcome of such a closure is the kinetic equation (KE) for the wave action spectrum and its stationary solutions describing energy and wave action cascades through scales called Kolmogorov-Zakharov (KZ) spectra [2, 3, 56]. It is the similarity of the KZ spectra to the Kolmogorov energy cascade spectrum in classical three-dimensional (3D) Navier-Stokes turbulence that allows one to classify WT as *turbulence*. On the other hand, in most physical applications, besides weakly nonlinear random waves there are also strongly nonlinear coherent structures which, even when not energetically dominant, interact with the random wave component, i.e. by random-to-coherent and coherent-to-random transformations, which may provide a route to the turbulence sink via wave breaking or wave collapses. In other words, together with the random weakly nonlinear waves, the strongly nonlinear coherent structures are also a fundamentally important part of the WTLC [56].

Let us now discuss realizations of WT in optical systems. Very briefly, we define OWT as the WT of light. As such, OWT is a subject within the more general nonlinear optics field, dealing with situations involving the propagation of light in nonlinear media which is fully or partially random. OWT is a niche area within the nonlinear optics field, and excludes a large section of the field, including systems fully dominated by strong coherent structures, such as solitons. The term *turbulence*, is even more relevant for OWT because of the similarities between the nonlinear light behavior to fluid dynamics, such as vortex-like solutions [57, 58] and shock waves [59]. Although there have been numerous theoretical and numerical studies of OWT [50, 60, 61, 62, 47], there have been few experimental observations to date [51]. OWT was theoretically predicted to exhibit dual cascade properties when two conserved quantities cascade to opposite regions of wave number space [50]. This is analogous to two-dimensional (2D) turbulence, where we observe an inverse cascade of energy and a direct cascade of enstrophy [63, 64]. In the context of OWT, energy cascades to high wave numbers, while wave action cascades towards low wave numbers [50, 60, 61, 62]. An interesting property of OWT is the inverse cascade of wave action which in the optical context implies the condensation of photons - the optical analogue of BEC.

It is the BEC processes that make OWT an attractive and important setup to study. Experimental implementation of BEC in alkali atoms was first achieved in 1995, and subsequently awarded the 2001 Nobel prize [65, 66]. This work involved developing a sophisticated cooling technique to micro-Kelvin temperatures, in order to make the de Broglie wave length exceed the average inter-particle distance. This is known as the BEC condition. Photons were actually the first bosons introduced by Bose in 1924 [67], and

the BEC condition is easily satisfied by light at room temperature. However, there was the belief that optical BEC would be impossible, because of the fundamental difference between atoms, whose numbers are conserved, and photons which can be randomly emitted and absorbed. However, there exist situations where light is neither emitted nor absorbed, e.g. light in an optical cavity, reflected back and forth by mirrors [68], or by light freely propagating through a transparent medium. In the latter, the movement of photons to different energy states (specifically the lowest one corresponding to BEC) can be achieved by nonlinear wave interactions. The mechanism for these nonlinear wave interactions is provided by the Kerr effect which permits wave mixing. Moreover, the nonlinear interactions are crucial for the BEC of light, because no condensation is possible in non-interacting 1D and 2D Bose systems.

When the nonlinearity of the system is weak, OWT can be described by weak WT theory [3, 56], with the prediction of two KZ states in a dual cascade system. One aspect of OWT is that the nonlinearity of the system is predicted to grow in the inverse cascade with the progression of wave action towards large scales. This will eventually lead to a violation of the weak nonlinearity assumption of WT theory. The high nonlinearity at low wave numbers will lead to the formation of coherent structures [50, 61, 47, 69, 70, 71]. In OWT this corresponds to the formation of solitons and collapses for focusing nonlinearity [51], or to a quasi-uniform condensate and vortices in the de-focusing case [47].

Experimentally, OWT is produced by propagating light through a nonlinear medium [72]. However, the nonlinearity is typically very weak and it is a challenge to make it overpower the dissipation. This is the main obstacle regarding the photon condensation setup in a 2D optical Fabry-Perot cavity, theoretically suggested in [68] but never experimentally implemented.

This brings us to the discussion of the exceptional role played by 1D optical systems. Firstly, it is in 1D that the first ever OWT experiment was implemented [51]. The key feature in our setup is to trade one spatial dimension for a time axis. Namely, we consider a time-independent 2D light field where the principal direction of the light propagation acts as an effective time. This allows us to use a nematic liquid crystal (LC), which provides a high level of tunable optical nonlinearity [73, 74]. The slow relaxation time of the re-orientational dynamics of the LC molecules is not a restriction of our setup because the system is steady in time. Similar experiments were first reported in [75], where a beam propagating inside a nematic layer undergoes a strong self-focusing effect followed by filamentation, soliton formation and an increase in light intensity. Recently, a renewed interest in the same setup has led to further studies on optical solitons and the MI regime [76, 77, 78]. However, all the previous experiments used a high input intensity, implying a strong nonlinearity of the system, and therefore the soliton condensate appears immediately, bypassing the WT regime. In our experiment, we carefully set up an initial condition of weakly nonlinear waves situated at high wave numbers from a laser beam. We randomize the phase of the beam, so that we produce a wave field as close to a random phase and amplitude (RPA) wave field as possible. The nonlinearity of the system is provided by the LC, controlled by a voltage applied across the LC cell. This provides the means for nonlinear wave mixing via the Kerr effect. The LC we use is of a focusing type, causing any condensate that forms to become unstable and the formation of solitons to occur via MI.

Secondly, from the theoretical point of view 1D OWT is very interesting because it represents a system close to an integrable one, namely the 1D nonlinear Schrödinger

equation (NLSE). Thus it inherits many features of the integrable model, e.g. the significant role of solitons undergoing nearly elastic collisions. On the other hand, deviations from the integrability are important, because they upset the time recursions of the integrable system thereby leading to turbulent cascades of energy and wave action through scales. We show that the process responsible for such cascades is a six-wave resonant interaction (wave mixing). Another example of a nearly integrable 1D six-wave system can be found in superfluid turbulence - it is the WT of Kelvin waves on quantized vortex lines [39, 79, 42, 43, 44, 46] (even though non-local interactions make the six-wave process effectively a four-wave one in this case). Some properties of the six-wave systems are shared with four-wave systems, particularly WT in the Majda-McLaughlin-Tabak (MMT) model reviewed in Physical Reports by Zakharov *et al* [71]. For example, both the four-wave and the six-wave systems are dual cascade systems, and in both systems solitons (or quasi-solitons) play a significant role in the WTLC. There are also significant differences between these two types of systems. Notably, pure KZ solutions appear to be much less important for the six-wave optical systems than for the four-wave MMT model - instead the spectra have a thermal component which is dominant over the flux component. Moreover, the number of solitons in 1D OWT decrease in time due to soliton mergers, so that asymptotically there is only a single strong soliton left in the system.

Similar behavior was extensively theoretically studied in various settings for non-integrable Hamiltonian systems starting with the paper by Zakharov *et al* [80], and then subsequently in [81, 82, 83, 84, 85, 86, 87, 88, 89, 90]. The final state, with a single soliton and small scale noise, was interpreted as a statistical attractor, and an analogy was pointed out to the over-saturated vapor system, where the solitons are similar to droplets and the random waves behave as molecules [90]. Indeed, small droplets evaporate whilst large droplets gain in size from free molecules, resulting in a decrease in the number of droplets. On the other hand, in the 1D OWT context, the remaining strong soliton is actually a narrow coherent beam of light. This allows us to interpret the WT evolution leading to the formation of such a beam as a lasing process. Here, the role of an active medium where the initial energy is stored is played by the weakly nonlinear random wave component, and the major mechanism for channeling this energy to the coherent beam is provided by the WT inverse cascade. For this reason, we can call such a system a *WT laser*. It is quite possible that the described WT lasing mechanism is responsible for spontaneous formation of coherent beams in stars or molecular clouds, although it would be premature to make any definite claims about this at present.

Generally, in spite of recent advances, the study of 1D OWT is far from being complete. The present review provides a report on the current state of this area describing not only what we have managed to learn and explain so far, but also the results which we do not know yet how to explain, discussing the existing theory and the gaps within it that are yet to be filled. We compare the experimental observations with the predictions of WT theory and independently juxtapose our findings with direct numerical simulation of the governing equations. In particular, we describe some puzzles related to the wave action spectra obtained in the experiment and in the numerical experiments. Furthermore, we will describe the recent extensions of weak WT theory onto the wave probability density function (PDF), which marks the beginning of developing a formalism for describing WT intermittency and the role of coherent structures. On the other hand, a theory for the WTLC incorporating interacting random waves and coherent structures/solitons is

still to be investigated, with only of a few pioneering works reporting on the study of the interaction between coherent structures and the radiating background [91].

2. The Experiment

The 1D optical system has been designed to meet the major requirements of OWT. Especially important are the careful calibrations that have been taken to fulfill the balance between low dissipation and low nonlinearity. Indeed, the main experimental challenge in observing the WT regime is in keeping the nonlinearity weak enough to let the WT regime develop and, at the same time, high enough to make it overpower the dissipation. Our setup is based on a nematic liquid crystal layer in which a laminar shaped beam propagates. LCs are particularly suitable for the observation of the WT regime because of their well known optical properties, such as their high and tunable nonlinearity, transparency (slow absorption) over a wide range of optical wave lengths, the realization of large cells and the possibility to drive them with low voltage externally applied fields [74].

2.1. Description of the Experimental Setup

The liquid crystal, LC, cell is schematically depicted in figure 2. It is made by sandwiching a nematic layer, (E48), of thickness $d = 50 \mu m$, between two $20 \times 30 mm^2$, glass windows and on the interior, the glass walls are coated with indium-tin-oxide transparent electrodes. We have pre-treated the indium-tin-oxide surfaces with polyvinyl-alcohol, polymerized and then rubbed, in order to align all the molecules parallel to the confining walls. When a voltage is applied across the cell, LC molecules tend to orientate in such a way as to become parallel to the direction of the electric field. By applying a $1 kHz$ electric field with a rms voltage of $V_0 = 2.5 V$ we preset the molecular director to an average tilt angle Θ .

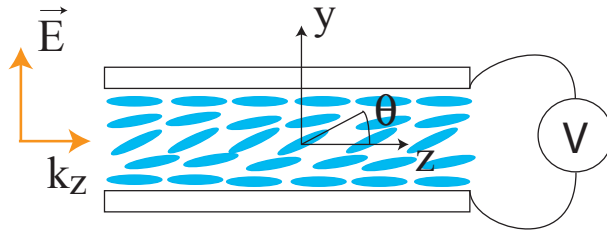


Figure 2: Schematic of the LC cell: molecules, initially aligned parallel to the confining walls, are oriented, through the application of the external voltage V , at an average angle θ , around which further reorientations are induced by the optical field \vec{E} .

The experimental apparatus is shown in figure 3. It consists of a LC cell, inside which a laminar shaped beam propagates. An important point is that the input beam is carefully prepared in such a way as to have an initial condition of weakly nonlinear random waves. As depicted in figure 3a, the preparation of the input beam is such that the system is forced with an initial condition Q_{in} , which is at a intermediate spatial scale between the large scale, $k = 0$, and the dissipative scale, k_d . Moreover, phases

are randomized so that a narrow bandwidth forcing is realized around the initial spatial modulation at the chosen wave number k_{in} .

The setup is schematically represented in figure 3b. The input light originates from a diode pumped, solid state laser, with $\lambda = 473 \text{ nm}$, polarized along y and shaped as a thin laminar Gaussian beam of $30 \mu\text{m}$ thickness. The input light intensity is kept very low, with an input intensity of $I = 30 \mu\text{W}/\text{cm}^2$ to ensure the weakly nonlinear regime. A spatial light modulator (SLM), at the entrance of the cell is used to produce suitable intensity masks for injecting random phased fields with large wave numbers. This is made by creating a random distribution of diffusing spots with the average size $\simeq 35 \mu\text{m}$ through the SLM.

The beam evolution inside the cell is monitored with an optical microscope and a CCD camera. The LC layer behaves as a positive uni-axial medium, where $n_{\parallel} = n_z = 1.7$ is the extraordinary refractive index and $n_{\perp} = 1.5$ is the ordinary refractive index [74]. The LC molecules tend to align along the applied field and the refractive index, $n(\Theta)$, follows the distribution of the tilt angle θ . When a linearly polarized beam is injected into the cell, the LC molecules orientate towards the direction of the incoming beam polarization, thus, realizing a re-orientational optical Kerr effect. Because the refractive index increases when molecules orient themselves towards the direction of the input beam polarization, the sign of the nonlinear index change is positive, hence, we have a focusing nonlinearity.

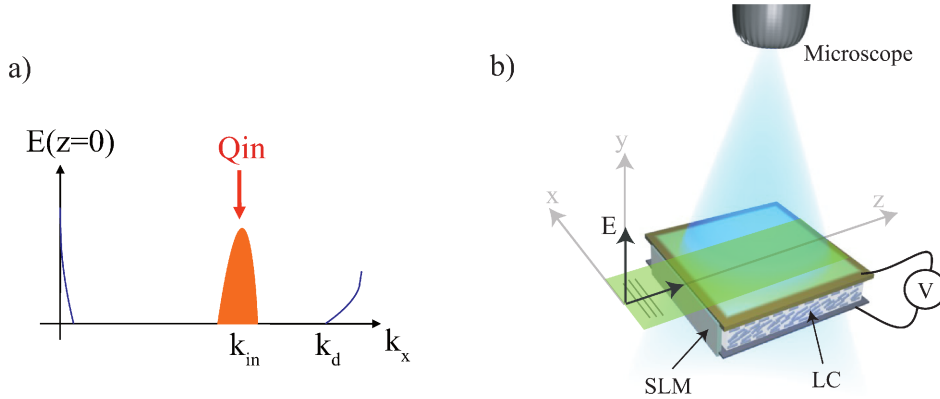


Figure 3: a) Spatial forcing realized as initial condition Q_{in} by appropriate preparation of the input beam; k_{in} is the chosen wave number around which random phase modulations are introduced. b) Sketch of the experimental setup: a laminar shaped input beam propagates inside the LC layer; random phase modulations are imposed at the entrance of the cell by means of a spatial light modulator, SLM.

Figure 4 depicts in more detail how the input light beam is prepared before entering the LC cell. The beam is expanded and collimated through the spatial light filter shown in figure 4. The objective, OB, focuses the light into the $20 \mu\text{m}$ pinhole, PH, the lens L_1 collimates the beam with a waist of 18 mm . After that, the light passes through the SLM, which is a LCD screen working in transmission with a resolution of 800×600 , with 8 bits pixels, of size $14 \mu\text{m}$. Each pixel is controlled through a personal computer PC, to ensure that the outgoing light is intensity modulated. In our case we use a cosine modulation having a colored noise envelope. The lenses, L_3 and L_4 , are used to focus

the image from the LCD screen at the entrance of the LC cell. The half wave-plate, W, together with the polarizer, P, are used to control the intensity and the polarization, which is linear along the y -axis. The circular aperture is inserted in the focal plane to filter out the diffraction given by the pixelization of the SLM and the diffuser, PH, is inserted to spatially randomize the phase of the light. In order to inject the light inside the LC cell, we use a cylindrical lens, L_4 , close to the entrance of the LC layer.

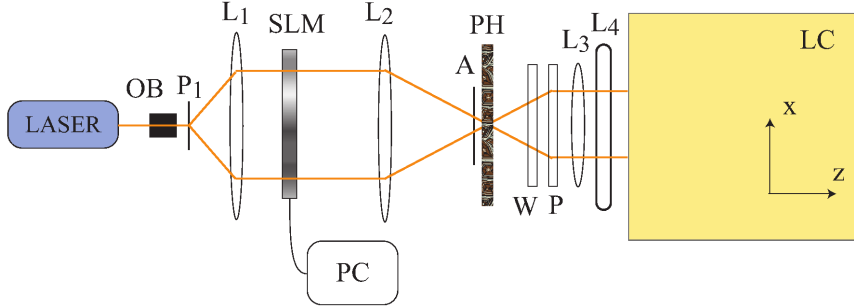


Figure 4: Detailed representation of the experimental setup, showing the initialization of the input laser beam. OB: objective, P_1 : pinhole, L_1, L_2, L_3, L_4 : lenses, SLM: spatial light modulator, PC: computer, A: variable aperture, PH: random phase plate, W: half-wave plate, P: polarizer, LC: liquid crystals.

2.2. The Evolution of the Light Intensity and the Inverse Cascade

The inverse cascade can be observed directly in the experiment by inspecting the light pattern in the (x, z) plane of the LC cell. Recall that z has here the role of time. Two magnified images of the intensity distribution $I(x, z)$ showing the beam evolution during propagation in the experiment are displayed in figure 5. For comparison, in figure 5a and b, we show the beam evolution in the linear and in the weakly nonlinear regimes, respectively. In figure 5a, we set a periodic initial condition with a uniform phase and apply no voltage to the LC cell. We see that the linear propagation is characterized by the periodic recurrence of the pattern with the same period, a phase slip occurring at every Talbot distance. This is defined by p^2/λ , with p , the period of the initial condition and λ , the laser wave length [92]. In figure 5b, we apply a voltage, $V = 2.5 V$ to the LC cell. The initial condition is periodic with the same period as in figure 5a, but now with random phases. We observe that the initial period of the pattern is becoming larger as the light beam propagates along z .

While the linear propagation in figure 5a, forms Talbot intensity carpets [93], with the initial intensity distribution reappearing periodically along the propagation direction z , the weak nonlinearity in figure 5b, leads to wave interactions, with different spatial frequencies mixing and the periodic occurrence of the Talbot carpet being broken. In figure 6, we show two intensity profiles taken in the nonlinear case at two different stages of the beam propagation. The inverse cascade is accompanied by a smoothing of the intensity profile and the amplification of low wave number components.

The inverse cascade can be measured directly by recording the evolution of the transverse light pattern $I(x, z)$ along z . However, experimentally we measure the light intensity $I(x, z)$ as we do not have direct access to the phases. Therefore, we measure the

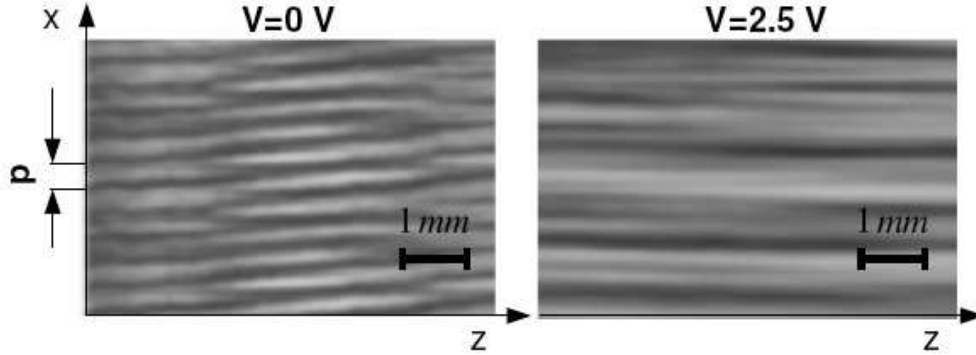


Figure 5: Intensity distribution $I(x, z)$ showing the beam evolution during propagation; a) linear case (no voltage applied to the LC cell), b) weakly nonlinear case (the voltage applied to the LC cell is set to 2.5 V). d is the spatial period of the input beam modulation at the entrance plane of the cell.

spectrum of intensity $N(k, z) = |I_k(z)|^2$, for which an appropriate scaling should be derived from the theory. The experimental scaling for N_k in the inverse cascade is obtained by fitting the experimental spectrum of the light intensity, and gives $N_k \sim |k|^{-1/5}$ as shown in figure 7. One can see an inverse cascade excitation of the lower k states, and a good agreement with the WT prediction.

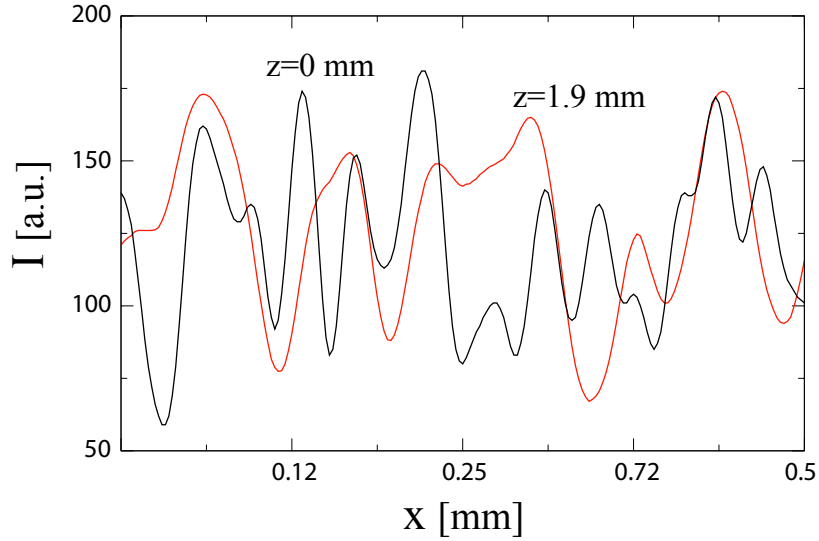


Figure 6: Two intensity profiles $I(x)$ recorded at $z = 0$ and $z = 1.9$ mm in the weakly nonlinear regime, with $V = 2.5$ V, showing the smoothing associated with the inverse cascade.

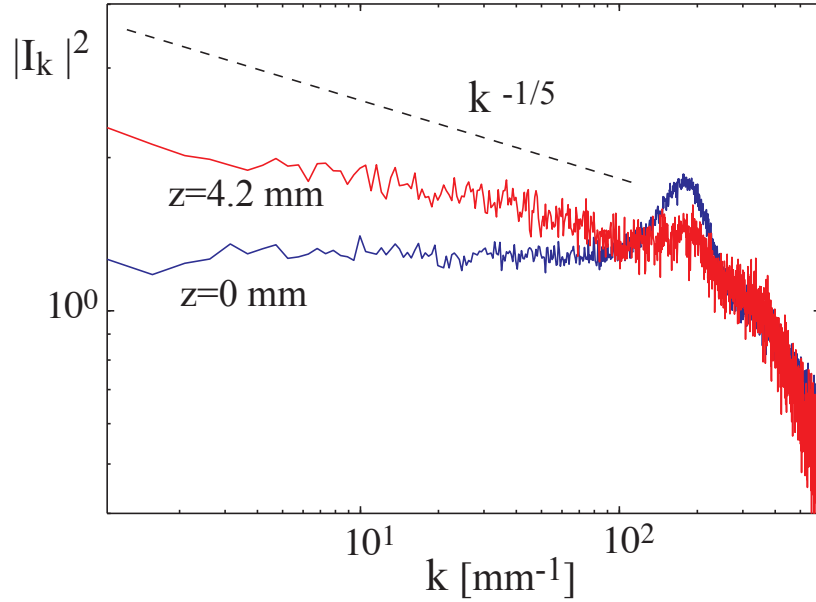


Figure 7: Experimental spectrum of the light intensity, $N_{\mathbf{k}} = |I_{\mathbf{k}}|^2$ at two different distances z .

2.3. The Long Distance Evolution and Soliton Formation

The intensity distribution $I(x, z)$, showing the beam evolution during propagation for longer distances is displayed in figures 8. In the high resolution inset we can observe that the typical wavelength of the waves increases along the beam, which corresponds to an inverse cascade process. Furthermore, one can see the formation of coherent solitons out of the random initial wave field, such that in the experiment, one strong soliton is dominant at the largest distance z .

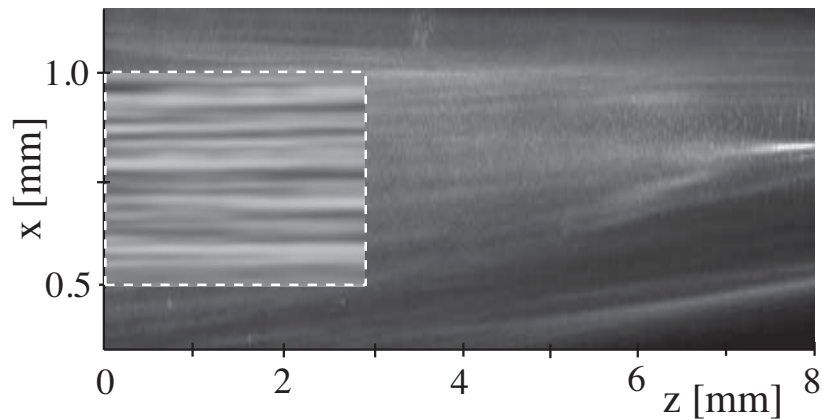


Figure 8: Experimental results for intensity distribution $I(x, z)$. The area marked by the dashed line is shown at a higher resolution (using a larger magnification objectif).

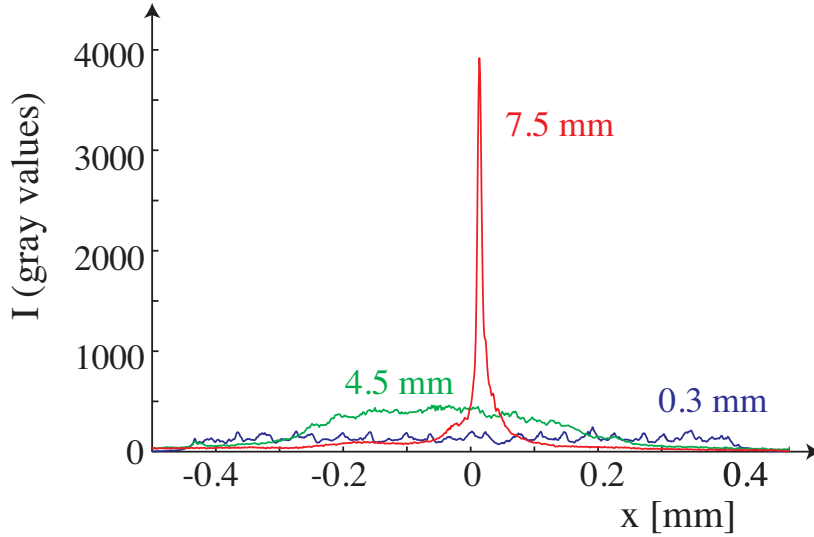


Figure 9: Linear intensity profiles $I(x)$ taken at different propagation distances, $z = 0.3, 4.5$ and 7.5 *mm*.

The experimental evolution reported in figure 8 indicates that the total number of solitons reduces. The observed increase of the scale and formation of coherent structures represents the condensation of light. Experimentally, the condensation into one dominant soliton is well revealed by the intensity profiles $I(x)$ taken at different propagation distances, as shown in figure 9 for $z = 0.3, 4.5$ and 7.5 *mm*. Note that the amplitude of the final dominant soliton is three orders of magnitude larger than the amplitude of the initial periodic modulation.

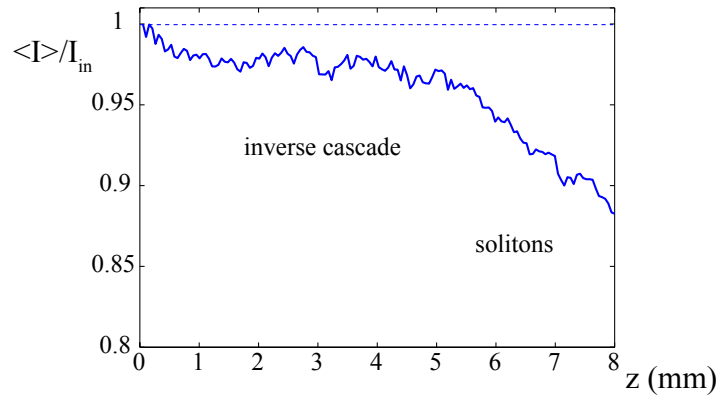


Figure 10: Evolution of the normalized x -averaged light intensity $\langle I \rangle / I_{in}$, where I_{in} is the input intensity, as a function of the propagation distance z .

As for energy dissipation, we should note that this is mainly due to radiation losses, whereas absorption in the liquid crystals is practically negligible [94]. In order to give

an estimation of the losses occurred during the z evolution we have averaged the light intensity $I(x, z)$ along x and calculated the ratio of the x -averaged intensity $\langle I \rangle$ to the input intensity I_{in} . The result is plotted in figure 10, from which we observe that after 8 mm of propagation the losses are about 15%. Moreover, by comparing figure 10 with the intensity distribution $I(x, z)$ (see figure 8), we can note that during the inverse cascade the total light intensity remains practically constant, whereas losses become more important when solitons start to appear.

2.4. The Probability Density Function of the Intensity

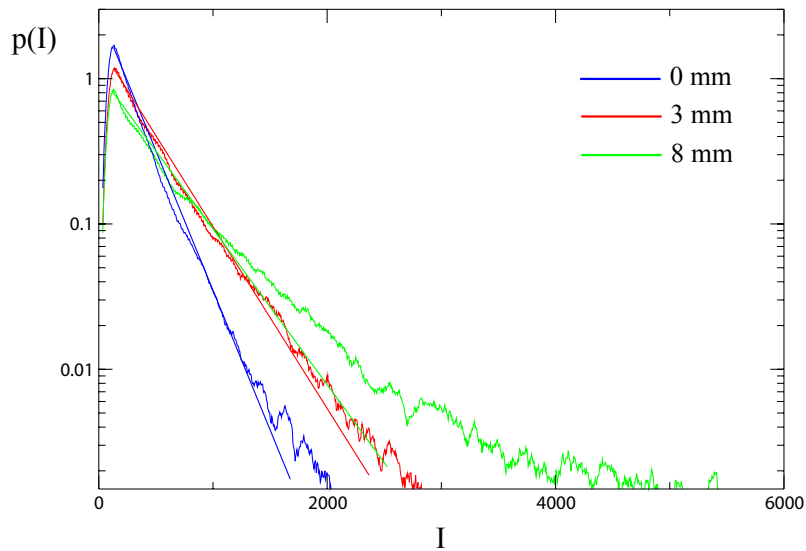


Figure 11: PDFs of the wave intensity within the experimental cell at three different distances along the cell, $z = 0$ mm, $z = 3$ mm and $z = 8$ mm. Straight lines correspond to the Rayleigh PDF's corresponding to Gaussian wave fields (these fits have the same mean as the respective numerical PDFs).

Figure 11 displays three experimentally obtained profiles of the PDF of the wave intensity along the cell at distances $z = 0$ mm, $z = 3$ mm and $z = 8$ mm in lin-log coordinates. In a pure Gaussian wave field, we would observe the Rayleigh distribution (31) which would correspond to a straight profile of the PDF in lin-log coordinates. However, in figure 11, non-Gaussianity is observed with the deviation from the straight lines, indicating a slower than exponential decay of the PDF tails. Non-Gaussianity corresponds to *intermittency* of WT.

Intermittency implies that there is a significantly higher occurrence of high intensity structures compared to that predicted by a Gaussian wave field and that the system is in the presence of an MI process leading to solitons. The observation of intermittency could be a sign of the development of coherent structures (solitons) in the system.

Analogies can be drawn of such high amplitude solitons with the rogue waves appearing in systems characterized by many nonlinearly interacting waves, as seen on the ocean surface [95], in nonlinear optical systems [96, 97, 98], and in superfluids [99]. For

all of which a description in terms of nonlinear coherent structures emerging from modulational instability in the nonlinear Schrödinger equation can be outlined [100]. In particular, possible links between rogue waves and wave turbulence in optical systems are discussed in [101].

2.5. *The Relation to Previous Studies of Optical Solitons*

Optical re-orientation of the LC occurs under the action of the light itself, with the LC molecules tending to align along the direction of the laser beam polarization, and giving rise to a Kerr effect that produces a self-focusing nonlinearity [73]. This effect was shown to lead to laser beam filamentation [75] and, recently, has been exploited to demonstrate the stable propagation of spatial optical solitons, also called nematicons, inside nematic LC cells [76]. For the same type of system, MI has also been reported [77, 78]. However, the previous experiments used a high input intensity, implying a strong nonlinearity of the system, and therefore filamentation and solitons appeared immediately, bypassing the WT regime.

Solitons are well-known and widely studied in nonlinear optics [102], where they are understood as light pulses that maintain their shape, unaltered during propagation in a nonlinear medium, and where the nonlinearity implies a change in the refractive index that is induced by the intensity of the light itself. In this context solitons are classified as being either spatial or temporal, whether the self-confinement of the light beam occurs in space or in time during their propagation. The nonlinearity of the medium corresponds, respectively, to a self-focusing or a self phase modulation effect.

While WT implies the presence of many random waves interacting with low nonlinearity, previous work conducted in the nonlinear optics field was mainly aimed at realizing self-confined beams in a different regime, where the nonlinearity was relatively high and the medium seeded by a single pulse of Gaussian shape. A spatial soliton is therefore obtained by imposing a tightly focused beam as an initial condition and, then by letting the beam propagate inside a medium where the self-focusing nonlinearity compensates the transverse beam widening by diffraction. These types of spatial solitons have been observed in a number of diverse optical media, such as, photorefractive crystals, atomic vapors, and semiconductor wave guides [103, 104]. On the other hand, temporal solitons correspond to cases when the nonlinearity compensates the temporal broadening of a light pulse due to the natural dispersion of the traversed medium [74], and have been observed in optical fibers.

In both cases, the theoretical approach to spatial and the temporal solitons are based on the NLSE. We therefore expect the generic behavior of the system to have an OWT regime existing before the formation of solitons. This entails an inverse cascade, the development of soliton turbulence and subsequently, a final single soliton acting as a statistical attractor of the system [80]. In the spatial case, the light propagation direction, usually denoted as z , plays the role of time, therefore the wave dispersion relation is of the type $\omega = k^2$, whereas in the temporal case the time derivative is in the second order dispersion term, hence the dispersion relation is of the type $k = \omega^2$. Theoretical predictions of OWT regimes should, therefore, be different in both cases. Recently, experiments achieving WT regimes in optical fibers have been devised [105] and the wave thermalization phenomena has been reported for the same type of system [106].

However, up to now only in the LC experiment has there been a genuine WT regime, with an inverse cascade and the spontaneous emergence of spatial solitons out of random waves, been demonstrated [51].

2.6. The Theoretical Model of the OWT Experiment

Theoretically, the experimental setup can be modeled by an evolution equation for the input beam, coupled to a relaxation equation for the LC dynamics given by

$$2iq\frac{\partial\psi}{\partial z} + \frac{\partial^2\psi}{\partial x^2} + k_0^2 n_a^2 a\psi = 0, \quad (1a)$$

$$\frac{\partial^2 a}{\partial x^2} - \frac{1}{l_\xi^2} a + \frac{\varepsilon_0 n_a^2}{4K} |\psi|^2 = 0, \quad (1b)$$

where $\psi(x, z)$ is the complex amplitude of the input beam propagating along the time axis z ; x is the coordinate across the beam; $a(x, z)$ is the LC reorientation angle; $n_a = n_e - n_o$ is the birefringence of the LC; k_0 is the optical wave number; ε_0 is the vacuum permittivity; and $l_\xi = \sqrt{\pi K/2\Delta\varepsilon}(d/V_0)$ is the electrical coherence length of the LC [107], with K being the elastic constant, $q^2 = k_0^2 (n_o^2 + n_a^2/2)$ and $\Delta\varepsilon$ is the dielectric anisotropy. Note that l_ξ fixes the typical dissipation scale, limiting the extent of the inertial range in which the OWT cascade develops. In other contexts, such a spatial diffusion of the molecular deformation has been denoted as a non-local effect, see [76, 77, 78]. In our experiment, when $V_0 = 2.5$ V, we have that $l_\xi = 9$ μm . By considering that a typical value of K is of the order ~ 10 pN, we can derive a typical dissipation length scale of the order ~ 10 μm .

The evolution equations, (1) for the complex amplitude of the input beam, $\psi(x, z)$, to the LC reorientation angle, $a(x, z)$ can be re-written as a single equation for field $\psi(x, z)$. This can be achieved by formally inverting the operator on $a(x, z)$ in equation (1b). Equation (1b) implies that

$$a(x, z) = \frac{\varepsilon_0 n_a^2}{4K} \left(\frac{1}{l_\xi^2} - \frac{\partial^2}{\partial x^2} \right)^{-1} |\psi|^2. \quad (2)$$

Substituting this expression into equation (1a), we eliminate the dependence on variable $a(x, z)$. This gives

$$2iq\frac{\partial\psi}{\partial z} + \frac{\partial^2\psi}{\partial x^2} + \frac{k_0^2 n_a^4 \varepsilon_0}{4K} \psi \left(\frac{1}{l_\xi^2} - \frac{\partial^2}{\partial x^2} \right)^{-1} |\psi|^2 = 0. \quad (3)$$

Equation (3) is a single equation modeling the evolution of the complex amplitude, $\psi(x, z)$. We can further simplify equation (3) by considering the system in two limits of wave number k : $kl_\xi \ll 1$ and $1 \ll kl_\xi$, that we call the long- and short-wave limits respectively. These limits enable the expansion of the nonlinear operator in power of $l_\xi \partial/\partial x$. Our experimental system is well described by the long-wave limit. The limitations imposed by the dissipation of the LC in the current experimental setup prevents the implementation in the short-wave regime. However, for the completeness of our description and for the possibilities in the modification of the experimental setup in the future for the short-wave regime, we will continue to investigate this limit theoretically and numerically.

2.6.1. The Long-Wave Regime

The long-wave approximation to equation (3) corresponds to the wavelength of the spatial light distribution, $\lambda \propto 1/k$, being greater than the electrical coherence length of the LC, l_ξ . In physical space, this limit corresponds to $l_\xi \partial/\partial x \ll 1$, which permits the expansion of the nonlinear operator of equation (3) as

$$\left(\frac{1}{l_\xi^2} - \frac{\partial^2}{\partial x^2}\right)^{-1} = l_\xi^2 \left(1 + l_\xi^2 \frac{\partial^2}{\partial x^2} + l_\xi^4 \frac{\partial^4}{\partial x^4} + \dots\right). \quad (4)$$

Taking the leading order of this expansion yields

$$2iq \frac{\partial \psi}{\partial z} = -\frac{\partial^2 \psi}{\partial x^2} - \frac{1}{2l_\xi^2 \tilde{\psi}^2} \psi |\psi|^2 \quad (5)$$

where, for clarity, we have introduced a reference light intensity:

$$\tilde{\psi}^2 = \frac{2K}{\varepsilon_0 n_a^4 l_\xi^4 k_0^2}. \quad (6)$$

Equation (5) is the 1D focusing NLSE. As is well-known, the 1D NLSE is an integrable system, solvable with the aid of the inverse scattering transform [108], and characterized by solitons¹. Unfortunately, this would be a poor model for OWT, as the integrability of the 1D NLSE implies that wave turbulent interactions are not possible. To overcome this, we must consider the sub-leading contribution in expansion (4). This extra nonlinear term acts as a correction breaking the integrability of the system. The resulting equation is given as

$$2iq \frac{\partial \psi}{\partial z} = -\frac{\partial^2 \psi}{\partial x^2} - \frac{1}{2l_\xi^2 \tilde{\psi}^2} \left(\psi |\psi|^2 + l_\xi^2 \psi \frac{\partial^2 |\psi|^2}{\partial x^2} \right). \quad (7)$$

We refer to equation (7) as the long-wave equation (LWE). For the expansion (4) to be valid, the additional nonlinear term must be considered smaller than the leading nonlinear term. Moreover for OWT to be in the weakly nonlinear regime, both of the nonlinear contributions should be smaller than the linear term. Therefore, although integrability is lost, the system will remain close to the integrable one described by (5). As a result, we expect soliton-like solutions close to the exact solutions of the 1D NLSE (5). On the other hand, exact soliton solutions of equation (5), do not change shape, and have the ability to pass through one another unchanged. We can expect that in the LWE (7), we will observe similar soliton solutions, but the non-integrability will allow solitons to interact with one another, and with the weakly nonlinear random wave background.

2.6.2. The Short-Wave Regime

In the opposite limit of equation (3), when $1 \ll l_\xi^2 \partial^2/\partial x^2$, the nonlinear operator of equation (3) can be represented in terms of a Taylor expansion of negative powers of the

¹The term soliton is sometimes reserved for solitary waves with special properties arising from integrability, such as the ability to pass through one another without change in shape or velocity, as is the case for the 1D NLSE. Hereafter, we will use the term soliton more broadly, including solitary waves in non-integrable systems which can change their states upon mutual collisions.

spatial derivative:

$$\left(\frac{1}{l_\xi^2} - \frac{\partial^2}{\partial x^2}\right)^{-1} = -\left(\frac{\partial^2}{\partial x^2}\right)^{-1} + \frac{1}{l_\xi^2} \left(\frac{\partial^2}{\partial x^2}\right)^{-2} - \dots \quad (8)$$

It is sufficient for us to approximate the nonlinear operator of equation (3) with just the leading order term in expansion (8), as integrability of the equation is not an issue. Therefore, we get an equation of the form:

$$2iq \frac{\partial \psi}{\partial z} = -\frac{\partial^2 \psi}{\partial x^2} + \frac{1}{2l_\xi^4 \tilde{\psi}^2} \psi \left(\frac{\partial^2}{\partial x^2}\right)^{-1} |\psi|^2. \quad (9)$$

We call equation (9) the short-wave equation (SWE). Ultimately, we have presented two dynamical equations for the complex wave amplitude $\psi(x, z)$ for 1D OWT in two limits of wave number space. Both of these systems can be expressed in a Hamiltonian formulation, that will be utilized by WT theory in the weakly nonlinear regime.

2.7. The Nonlinearity Parameter

It is essential for the development of OWT that the system operates in a weakly nonlinear regime. We can quantify the linearity and nonlinearity within the system with the introduction of a nonlinear parameter, J , which is determined by the ratio of the linear term to the nonlinear term within the dynamical equations.

For instance, the nonlinear parameter from the LTE (7) is defined as

$$J^L = \frac{2\tilde{\psi}^2 k^2 l_\xi^2}{I}. \quad (10)$$

This is derived from the ratio of the linear term and the first of the two nonlinear terms. Here, $I = \langle |\psi(x, z)|^2 \rangle$ is the average value of the light intensity. Similarly, the SWE, (9) yields a nonlinearity parameter of

$$J^S = \frac{2\tilde{\psi}^2 k^4 l_\xi^4}{I}. \quad (11)$$

Calculation of J^L and J^S act as a verification of the weak nonlinear assumption of WT. This is especially important in the context of experimental implementations of OWT, where initially unknown quantities are often difficult to measure.

2.8. The Hamiltonian Formulation

Both equations (7) and (9) can be written in terms of a Hamiltonian system of the form

$$2iq \frac{\partial \psi}{\partial z} = \frac{\delta \mathcal{H}}{\delta \psi^*}. \quad (12)$$

For the LTE, the Hamiltonian is given as

$$\begin{aligned} \mathcal{H}^L &= \mathcal{H}_2 + \mathcal{H}_4^L, \\ &= \int \left\{ \left| \frac{\partial \psi}{\partial x} \right|^2 - \frac{1}{4\tilde{\psi}^2} \left[\frac{|\psi|^4}{l_\xi^2} - \left(\frac{\partial |\psi|^2}{\partial x} \right)^2 \right] \right\} dx. \end{aligned} \quad (13a)$$

In the nonlinear energy term \mathcal{H}_4 , the term quartic with respect to ψ , we have added a superscript L to denote that this quartic term corresponds to the LWE, (7). This is because the Hamiltonian of the LWE and SWE only differ in the expression \mathcal{H}_4 . For the SWE, the Hamiltonian is given by

$$\begin{aligned}\mathcal{H}^S &= \mathcal{H}_2 + \mathcal{H}_4^S, \\ &= \int \left[\left| \frac{\partial \psi}{\partial x} \right|^2 - \frac{1}{4l_\xi^4 \tilde{\psi}^2} \left(\frac{\partial^{-1} |\psi|^2}{\partial x^{-1}} \right)^2 \right] dx.\end{aligned}\quad (13b)$$

In both the LWE and the SWE, the linear, (quadratic), energy \mathcal{H}_2 is identical. The Hamiltonians (13) coincide with the total energy of the systems and are conserved by their respective dynamics ($\mathcal{H} = \text{const}$). Moreover, both the LWE and SWE contain an additional invariant, the wave action \mathcal{N} defined as

$$\mathcal{N} = \int |\psi|^2 dx. \quad (14)$$

Conservation of \mathcal{N} is a consequence of the $U(1)$ gauge symmetry or invariance of equations (7) and (9) with respect to a phase shift: $\psi(x, z) \rightarrow \psi(x, z) \exp(i\phi)$.

By expressing the Hamiltonian in terms of its Fourier representation

$$\psi(x, z) = \sum_{\mathbf{k}} a(\mathbf{k}, z) e^{i\mathbf{k}x}, \quad (15)$$

here $\mathbf{k} \in \mathbb{R}$, the general Hamiltonian structure for Hamiltonians (13) can be represented in terms of the wave amplitude variable:

$$\mathcal{H} = \sum_{\mathbf{k}} \omega_k a_{\mathbf{k}} a_{\mathbf{k}}^* + \frac{1}{4} \sum_{1,2,3,4} T_{3,4}^{1,2} a_1 a_2 a_3^* a_4^* \delta_{3,4}^{1,2}, \quad (16)$$

where $\omega_k = k^2$ is the linear frequency² of non-interacting waves, $\delta_{3,4}^{1,2} = \delta(\mathbf{k}_1 + \mathbf{k}_2 - \mathbf{k}_3 - \mathbf{k}_4)$ is a Kronecker delta function, $T_{3,4}^{1,2} = T(\mathbf{k}_1, \mathbf{k}_2, \mathbf{k}_3, \mathbf{k}_4)$ is the nonlinear interaction coefficient, and the subscripts in the summation correspond to the summation over the associated wave numbers. Note that we use bold symbol \mathbf{k} for the wave number to emphasize that it can be either positive or negative, while k is reserved specifically for the wave vector length, $k = |\mathbf{k}|$.

By symmetry arguments, the interaction coefficient should not change under the permutations $\mathbf{k}_1 \leftrightarrow \mathbf{k}_2$, $\mathbf{k}_3 \leftrightarrow \mathbf{k}_4$. Furthermore, the Hamiltonian (16) represents the total energy of the system and is therefore a real quantity. This property implies extra symmetries of the interaction coefficient:

$$T_{3,4}^{1,2} = T_{3,4}^{2,1} = T_{4,3}^{1,2} = (T_{1,2}^{3,4})^*. \quad (17)$$

For the LWE Hamiltonian (13a), the interaction coefficient is defined as follows,

$$\begin{aligned}{}^L T_{3,4}^{1,2} &= {}^1 T_{3,4}^{1,2} + {}^2 T_{3,4}^{1,2} \\ &= -\frac{1}{l_\xi^2 \tilde{\psi}^2} + \frac{1}{2\tilde{\psi}^2} (\mathbf{k}_1 \mathbf{k}_4 + \mathbf{k}_2 \mathbf{k}_3 + \mathbf{k}_2 \mathbf{k}_4 + \mathbf{k}_1 \mathbf{k}_3 - 2\mathbf{k}_3 \mathbf{k}_4 - 2\mathbf{k}_1 \mathbf{k}_2).\end{aligned}\quad (18a)$$

²Indeed, ω_k is the frequency with respect to the time variable which is related to the distance z as $t = z/2q$.

We have denoted the two contributions to ${}^L T_{3,4}^{1,2}$, from both nonlinear terms in (7), as ${}^1 T_{3,4}^{1,2}$ and ${}^2 T_{3,4}^{1,2}$, where the first arises from the usual cubic nonlinearity seen in the 1D focusing NLSE, and the second from the sub-leading correction.

Similarly, the SWE yields the following interaction coefficient,

$${}^S T_{3,4}^{1,2} = \frac{1}{2l_\xi^4 \tilde{\psi}^2} \left(\frac{1}{\mathbf{k}_1 \mathbf{k}_3} + \frac{1}{\mathbf{k}_2 \mathbf{k}_3} + \frac{1}{\mathbf{k}_1 \mathbf{k}_4} + \frac{1}{\mathbf{k}_2 \mathbf{k}_4} - \frac{2}{\mathbf{k}_1 \mathbf{k}_2} - \frac{2}{\mathbf{k}_3 \mathbf{k}_4} \right). \quad (19a)$$

In terms of the wave amplitude variables $a(\mathbf{k})$, the Hamiltonian system (16) satisfies the Fourier space analogue of equation (12):

$$2iq \frac{\partial a(\mathbf{k}, z)}{\partial z} = \frac{\delta \mathcal{H}}{\delta a^*(\mathbf{k}, z)}. \quad (20)$$

It is with equation (20) that the formulation of WT theory is applied. In the next Section, we will give a brief mathematical description of WT theory, and outline the assumptions on the wave field that is required to apply such an approach.

2.9. The Canonical Transformation

Nonlinear wave interactions can be classified by the lowest order of resonance interactions they undergo. For an $N \leftrightarrow M$ wave scattering process, these resonance conditions are defined as

$$\mathbf{k}_1 + \dots + \mathbf{k}_N = \mathbf{k}_{N+1} + \dots + \mathbf{k}_{N+M}, \quad (21a)$$

$$\omega_1 + \dots + \omega_N = \omega_{N+1} + \dots + \omega_{N+M}, \quad (21b)$$

where \mathbf{k}_i is the wave number and $\omega_i = \omega(\mathbf{k}_i)$ is the frequency of wave i .

The lower orders of nonlinearity can be eliminated using a quasi-identity canonical transformation (CT) which is similar to the Poincaré-type algorithm used in, e.g. the construction of the corrected wave action for the perturbed integrable systems in Kolmogorov-Arnold-Moser (KAM) theory. The latter represents a recursive procedure eliminating the lower-order interaction terms one by one at each of the recursive steps, which is only possible when there are no resonances at that respective order. In WT theory, such a recursion is “incomplete” - it contains a finite number of recursive steps until the later steps are prevented by the lowest order wave resonances. The CT procedure for eliminating the non-resonant interactions in WT theory is explained in [3], where the most prominent example given was for the system of gravity water waves, where it was used to eliminate the non-resonant cubic Hamiltonian (see also [109] where some minor mistakes made for gravity waves were corrected).

Of course, apart for satisfying the resonant conditions, the respective type of the nonlinear coupling must be present. For example, the 2D and 3D NLSE have the dispersion relation $\omega_k = k^2$ which can satisfy the three-wave $1 \leftrightarrow 2$ resonance conditions, but the three-wave nonlinear coupling is zero. On the other hand, for gravity water waves there is a $1 \leftrightarrow 2$ wave interaction Hamiltonian (when written in terms of the natural variables - height and velocity potential), but the wave linear frequency $\omega_k = \sqrt{gk}$ does not allow for $1 \leftrightarrow 2$ resonances [52]. As a consequence, the lowest order resonant processes in all of these cases are four-wave ($2 \leftrightarrow 2$). For 1D OWT, like in the NLSE, the frequency of the linear propagating waves is given by

$$\omega(\mathbf{k}) = k^2, \quad (22)$$

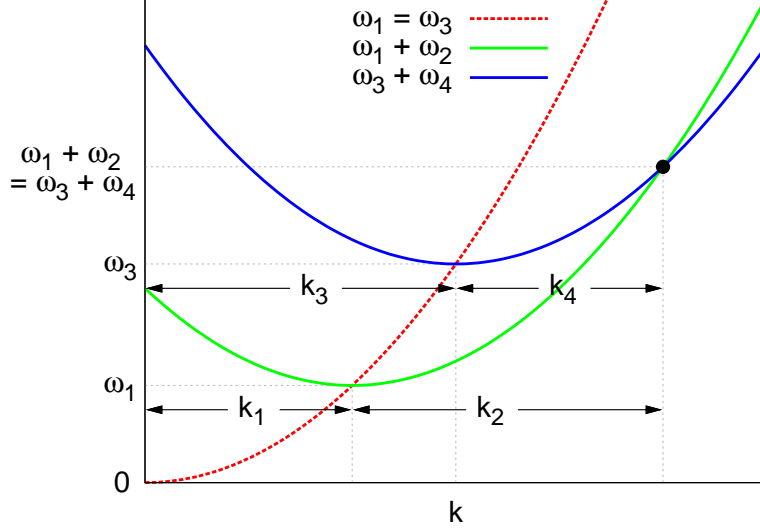


Figure 12: We plot a graphical representation of the four-wave resonance condition [56]. The four-wave resonance condition is satisfied at points where the green and blue lines intersect, (shown by the black dot). However, for dispersion relations $\omega_k \propto k^\alpha$, with $\alpha > 1$, there can only be one intersection, corresponding to the trivial wave resonance: $\mathbf{k}_1 = \mathbf{k}_4$ and $\mathbf{k}_2 = \mathbf{k}_3$.

In 1D, dispersion relations of the form $\omega(\mathbf{k}) \propto k^\alpha$ with $\alpha > 1$ cannot satisfy the four-wave resonance condition:

$$\mathbf{k}_1 + \mathbf{k}_2 = \mathbf{k}_3 + \mathbf{k}_4, \quad (23a)$$

$$\omega(\mathbf{k}_1) + \omega(\mathbf{k}_2) = \omega(\mathbf{k}_3) + \omega(\mathbf{k}_4). \quad (23b)$$

This can be understood by a simple graphical proof presented in figure 12 [56]. In figure 12 we observe the red dashed curve representing the dispersion relation $\omega_k = Ck^\alpha$ with $\alpha > 1$. At two locations along this curve (at $\mathbf{k} = \mathbf{k}_1$ and $\mathbf{k} = \mathbf{k}_3$), two further dispersion curves (the green and blue solid lines) are produced: with their minima at points $(\mathbf{k}, \omega) = (\mathbf{k}_1, \omega_1)$ and at (\mathbf{k}_3, ω_3) respectively. These subsequent lines represent the wave frequencies of $\omega_1 + \omega_2$ and $\omega_3 + \omega_4$, where \mathbf{k}_1 and \mathbf{k}_3 are now fixed, with \mathbf{k}_2 varying along the green solid line and \mathbf{k}_4 varying along the blue line. If the green and blue lines intersect, it will be when the four-wave resonance condition (23) is satisfied and will occur at the point $(\mathbf{k}, \omega) = (\mathbf{k}_1 + \mathbf{k}_2, \omega_1 + \omega_2) = (\mathbf{k}_3 + \mathbf{k}_4, \omega_3 + \omega_4)$. In figure 12, we observe that such an intersection occurs only once, and it can be clearly seen that $\mathbf{k}_1 = \mathbf{k}_4$ and $\mathbf{k}_2 = \mathbf{k}_3$ must hold. This corresponds to a trivial pairing of wave numbers, which will not provide any nonlinear energy exchange between modes. As a consequence, resonant four-wave interactions are absent in the system. There are no five-wave interactions either because the $U(1)$ symmetry prohibits the presence of odd orders in the wave amplitude in the interaction Hamiltonian. In situations such as these, there exists a weakly nonlinear CT that allows us to change to new canonical variables such that the leading interaction Hamiltonian is of order six.

A similar strategy was recently applied to eliminate non-resonant fourth-order interactions in the context of Kelvin waves in superfluid turbulence [110, 44] and in nonlinear optics [51]. The details of the CT for our optical system can be found in Appendix A. The result of the CT is the representation of our system in a new canonical variable $c_{\mathbf{k}}$ with the elimination of the quartic contribution \mathcal{H}_4 . This however results in the appearance of a sextic contribution \mathcal{H}_6 :

$$\mathcal{H} = \sum_{\mathbf{k}} \omega_{\mathbf{k}} c_{\mathbf{k}} c_{\mathbf{k}}^* + \frac{1}{36} \sum_{1,2,3,4,5,6} \mathcal{W}_{4,5,6}^{1,2,3} \delta_{4,5,6}^{1,2,3} c_1 c_2 c_3 c_4^* c_5^* c_6^*, \quad (24)$$

where the explicit formula for $\mathcal{W}_{4,5,6}^{1,2,3}$ stemming from the CT is given by

$$\mathcal{W}_{4,5,6}^{1,2,3} = -\frac{1}{8} \sum_{\substack{i,j,m=1 \\ i \neq j \neq m \neq i}}^3 \sum_{\substack{p,q,r=4 \\ p \neq q \neq r \neq p}}^6 \frac{T_{p,q}^{p+q-i,i} T_{j,m}^{j+m-r,r}}{\omega_{j,m}^{j+m-r,r}} + \frac{T_{i,j}^{i+j-p,p} T_{q,r}^{q+r-m,m}}{\omega_{q,r}^{q+r-m,m}}, \quad (25)$$

where we have use the notation $\omega_{3,4}^{1,2} = \omega_1 + \omega_2 - \omega_3 - \omega_4$. Note that analogous to the symmetries of the four-wave interaction coefficient $T_{3,4}^{1,2}$, we must similarly impose the following symmetry conditions on $\mathcal{W}_{4,5,6}^{1,2,3}$ to ensure the Hamiltonian is real:

$$\mathcal{W}_{4,5,6}^{1,2,3} = \mathcal{W}_{4,5,6}^{2,1,3} = \mathcal{W}_{4,5,6}^{3,2,1} = \mathcal{W}_{4,5,6}^{1,3,2} = \mathcal{W}_{4,5,6}^{2,3,1} = \mathcal{W}_{4,5,6}^{3,1,2} = \left(\mathcal{W}_{1,2,3}^{4,5,6} \right)^*. \quad (26)$$

Hamiltonian (24) represents the the original Hamiltonian system (16), but now in the new canonical variable $c_{\mathbf{k}}$. The interaction Hamiltonian has now been transformed from having a leading non-resonant fourth-order interaction term into one with a leading resonant six-wave interaction. From the formula of the new six-wave interaction coefficient (25), the six-wave interaction stems from the coupling of two non-resonant four-wave interactions connected by a *virtual* wave (an illustration is presented in figure 13).

By substituting Hamiltonian (24) into equation (20), we derive an evolution equation for the wave action variable $c_{\mathbf{k}}$,

$$i\dot{c}_{\mathbf{k}} = \omega_{\mathbf{k}} c_{\mathbf{k}} + \frac{1}{12} \sum_{2,3,4,5,6} \mathcal{W}_{4,5,6}^{\mathbf{k},2,3} c_2^* c_3^* c_4 c_5 c_6 \delta_{4,5,6}^{\mathbf{k},2,3}, \quad (27)$$

where we denote the “time” derivative of $c_{\mathbf{k}}$ as $\dot{c}_{\mathbf{k}} = \partial c_{\mathbf{k}} / \partial z$. This equation is the starting point for WT theory. This is the six-wave analogue of the well-known Zakharov equation describing four-wave interactions of water surface waves [111].

3. Wave Turbulence Theory

General formulation of WT theory can be found in a recent book [56], reviews [112, 71, 113] and the older classical book [3]. In our review will only outline the basic ideas and steps of WT, following mostly the approach of [56]. More details will be given on the parts not covered in these sources, namely the six-wave systems arising in OWT and respective solutions and their analysis.

Let us consider a 1D wave field, $a(x, z)$, in a domain which is periodic in the x -direction with period L , and let the Fourier transform of this field be represented by the

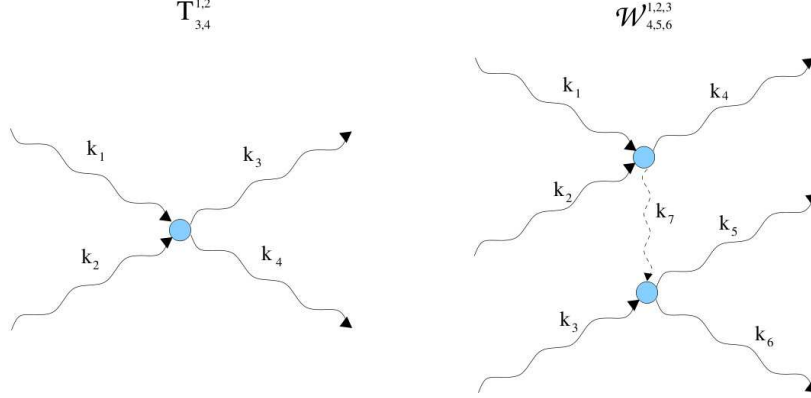


Figure 13: An illustration to show the non-resonant four-wave interaction, $T_{3,4}^{1,2}$, and the resonant six-wave interaction, $\mathcal{W}_{4,5,6}^{1,2,3}$, after the CT. The six-wave (sextet) interaction term is a contribution arising from two coupled four-wave (quartet) interactions via a virtual wave (dashed line).

Fourier amplitudes $a_l(t) = a(\mathbf{k}_l, z)$, with wave number, $\mathbf{k}_l = 2\pi l/L$, $l \in \mathbb{Z}$. Recall that the propagating distance z in our system plays a role of “time”, and consider the amplitude-phase decomposition $a_l(t) = A_l(z)\psi_l(z)$, such that A_l is a real positive amplitude and ψ_l is a phase factor that takes values on the unit circle in the complex plane. Following [114, 115, 116, 117], we say a wave field $a(x, z)$ is an RPA field, if all the amplitudes $A_l(z)$ and the phase factors $\psi_l(z)$ are independent random variables and all ψ_l s are uniformly distributed on the unit circle on the complex plane. We remark, that the RPA property does not require us to fix the shape of the amplitude PDF, and therefore, we can deal with strongly non-Gaussian wave fields. This will be useful for the description of WT intermittency.

Construction of the WT theory for a particular wave system consists of three main steps: *i*) expansion of the Hamiltonian dynamical equation (equation (27) in our case) in powers of a small nonlinearity parameter, *ii*) making the assumption that the initial wave field is RPA and statistical averaging over the initial data, and finally *iii*) taking the large box limit followed by the weak nonlinearity limit. Since the derivations for our OWT example are rather technical and methodologically quite similar to the standard procedure described in [56], we move these derivations to Appendix B. This approach leads to an evolution equation for the one-mode amplitude PDF $\mathcal{P}_{\mathbf{k}}(s_{\mathbf{k}})$ which is the probability of observing the wave intensity $J_{\mathbf{k}} = |A_{\mathbf{k}}|^2$ of the mode \mathbf{k} in the range $(s_{\mathbf{k}}, s_{\mathbf{k}} + ds_{\mathbf{k}})$:

$$\dot{\mathcal{P}}_{\mathbf{k}} = -\frac{\partial \mathcal{F}_{\mathbf{k}}}{\partial s_{\mathbf{k}}}, \quad \mathcal{F}_{\mathbf{k}} = -\left(s_{\mathbf{k}} \gamma_{\mathbf{k}} \mathcal{P}_{\mathbf{k}} + s_{\mathbf{k}} \eta_{\mathbf{k}} \frac{\partial \mathcal{P}_{\mathbf{k}}}{\partial s_{\mathbf{k}}} \right), \quad (28)$$

where we have introduced a probability space flux $\mathcal{F}_{\mathbf{k}}$ and where

$$\eta_{\mathbf{k}} = \frac{\epsilon^8 \pi}{6} \int |\mathcal{W}_{4,5,6}^{\mathbf{k},2,3}|^2 \delta_{4,5,6}^{\mathbf{k},2,3} \delta(\omega_{4,5,6}^{\mathbf{k},2,3}) n_2 n_3 n_4 n_5 n_6 d\mathbf{k}_2 d\mathbf{k}_3 d\mathbf{k}_4 d\mathbf{k}_5 d\mathbf{k}_6, \quad (29a)$$

and

$$\gamma_{\mathbf{k}} = \frac{\epsilon^8 \pi}{6} \int |\mathcal{W}_{4,5,6}^{\mathbf{k},2,3}|^2 \delta_{4,5,6}^{\mathbf{k},2,3} \delta(\omega_{4,5,6}^{k,2,3}) [(n_2 + n_3) n_4 n_5 n_6 - n_2 n_3 (n_4 n_5 + n_4 n_6 + n_5 n_6)] d\mathbf{k}_2 d\mathbf{k}_3 d\mathbf{k}_4 d\mathbf{k}_5 d\mathbf{k}_6. \quad (29b)$$

Multiplying equation (28) by $s_{\mathbf{k}}$ and integrating over $s_{\mathbf{k}}$, we then obtain the KE, an evolution equation for the wave action density $n_{\mathbf{k}} = \langle |c_{\mathbf{k}}|^2 \rangle$:

$$\dot{n}_{\mathbf{k}} = \eta_{\mathbf{k}} - \gamma_{\mathbf{k}} n_{\mathbf{k}}, \quad (30)$$

Our main focus is on the non-equilibrium steady state solutions of equations (28) and (30).

3.1. Solutions for the One-Mode PDF: Intermittency

The simplest steady state solution corresponds to the zero flux scenario, $\mathcal{F}_{\mathbf{k}} = 0$:

$$\mathcal{P}_{\text{hom}} = \frac{1}{n_{\mathbf{k}}} e^{-\frac{s_{\mathbf{k}}}{n_{\mathbf{k}}}}, \quad (31)$$

where $n_{\mathbf{k}}$ corresponds to any stationary state of the KE. Solution \mathcal{P}_{hom} , is the Rayleigh distribution. Subscript *hom* refers to the fact that this is the solution to the homogeneous part of a more general solution for a steady state with a constant non-zero flux, $\mathcal{F}_{\mathbf{k}} = \mathcal{F} \neq 0$. The general solution in this case is [114]

$$\mathcal{P}_{\mathbf{k}} = \mathcal{P}_{\text{hom}} + \mathcal{P}_{\text{part}}, \quad (32)$$

where $\mathcal{P}_{\text{part}}$ is the particular solution to equation (28). The particular solution is a correction due to the presence of a non-zero flux. In the region of the PDF tail, where $s_{\mathbf{k}} \gg n_{\mathbf{k}}$, we can expand $\mathcal{P}_{\text{part}}$ in powers of $n_{\mathbf{k}}/s_{\mathbf{k}}$:

$$\mathcal{P}_{\text{part}} = -\frac{\mathcal{F}}{s_{\mathbf{k}} \gamma_{\mathbf{k}}} - \frac{\eta_{\mathbf{k}} \mathcal{F}}{(s_{\mathbf{k}} \gamma_{\mathbf{k}})^2} - \dots. \quad (33)$$

Thus, at leading order, the PDF tail has algebraic decay $\sim 1/s_{\mathbf{k}}$, which corresponds to the presence of strong intermittency of WT [114]. From equation (33), we observe that a negative \mathcal{F} implies an enhanced probability of high intensity events. Subsequently, a positive flux, \mathcal{F} , would imply that there is less probability in observing high intensity structures than what is expected by a Gaussian wave field. In WT systems, we expect to observe both kinds of behavior each realized in its own part of the \mathbf{k} -space forming a WTLC, which will be discussed later.

3.2. Solutions of the Kinetic Equation

The KE (30) is the main equation in WT theory, it describes the evolution of the wave action spectrum $n_{\mathbf{k}}$. It can be written a more compact form as

$$\begin{aligned} \dot{n}_{\mathbf{k}} = & \frac{\epsilon^8 \pi}{6} \int |\mathcal{W}_{4,5,6}^{\mathbf{k},2,3}|^2 \delta_{4,5,6}^{\mathbf{k},2,3} \delta(\omega_{4,5,6}^{k,2,3}) n_{\mathbf{k}} n_2 n_3 n_4 n_5 n_6 \\ & \times (n_{\mathbf{k}}^{-1} + n_2^{-1} + n_3^{-1} - n_4^{-1} - n_5^{-1} - n_6^{-1}) d\mathbf{k}_2 d\mathbf{k}_3 d\mathbf{k}_4 d\mathbf{k}_5 d\mathbf{k}_6. \end{aligned} \quad (34)$$

The integral on the right hand side of the KE, (34), is known as the *collision integral*. Stationary solutions of the KE are solutions that make the collision integral zero. There exist two types of stationary solutions to the KE. The first type are referred to as the thermodynamic equilibrium solutions. The thermodynamic solutions correspond to an equilibrated system and thus refer to an absence of a \mathbf{k} -space flux for the conserved quantities, (in our case, linear energy, \mathcal{H}_2 , and total wave action, \mathcal{N}). The second type are known as the KZ solutions. They correspond to non-equilibrium stationary states determined by the transfer of a constant non-zero \mathbf{k} -space flux. They arise when the system is in the presence of forcing (source) and dissipation (sink), where there exists some intermediate range of scales, known as the *inertial range*, where neither forcing of dissipation influences the transfer of the cascading invariant. The discovery of the KZ solutions for the KE has been one of the major achievements of WT theory, and as such these solutions have received a large amount of attention within the community. In systems that possess more than one invariant, the KZ solutions describe the transfer of invariants to distinct regions of \mathbf{k} -space [3]. For many systems, these regions are usually the low and high wave number areas of \mathbf{k} -space, however this is not necessarily the case for anisotropic wave systems [118]. The directions in which the invariants cascade can be discovered by considering a Fjørtoft argument.

3.3. Dual Cascade Behavior

As 1D OWT has two invariants, there are two KZ solutions of the KE, each defined by a constant flux transfer of either invariant. This is analogous to 2D turbulence, where the enstrophy, (the integrated squared vorticity), cascades towards small scales and energy towards large scales [63, 64]. When a non-equilibrium statistical steady state is achieved in a weak nonlinear regime, the total energy (which is conserved) is dominated by the linear energy ($\mathcal{H} \approx \mathcal{H}_2$). Hence, we can make the assumption that the linear energy is almost conserved. This is important as the linear energy is a quadratic quantity in $\psi(x, z)$ and allows for the application of the Fjørtoft argument [119]. This argument was originally derived in the context of 2D turbulence, and does not require any assumptions on the locality of wave interactions. To begin, let us define the energy flux $P(\mathbf{k}, t) = P_{\mathbf{k}}$ and wave action flux $Q(\mathbf{k}, t) = Q_{\mathbf{k}}$ by

$$\frac{\partial \epsilon_{\mathbf{k}}}{\partial z} = -\frac{\partial P_{\mathbf{k}}}{\partial \mathbf{k}}, \quad \frac{\partial n_{\mathbf{k}}}{\partial z} = -\frac{\partial Q_{\mathbf{k}}}{\partial \mathbf{k}}, \quad (35)$$

where the energy density in Fourier space is defined as $\epsilon_{\mathbf{k}} = \omega_{\mathbf{k}} n_{\mathbf{k}}$, such that $\mathcal{H}_2 = \int \epsilon_{\mathbf{k}} d\mathbf{k}$. Below, we will outline the Fjørtoft argument in the context of the six-wave OWT system.

We should assume that the system has reached a non-equilibrium statistical steady state, therefore the total amount of energy flux, $P_{\mathbf{k}}$, and wave action flux, $Q_{\mathbf{k}}$, contained within the system must be zero, i.e. $\int P_{\mathbf{k}} d\mathbf{k} = 0$ and $\int Q_{\mathbf{k}} d\mathbf{k} = 0$ respectively - this corresponds to the flux input equaling the flux output. Then, let the system be forced at a specific intermediate scale, say \mathbf{k}_f , with both energy and wave action fluxes being generated into the system at rates P_f and Q_f . Moreover, let there exist two sinks, one towards small scales, say at $k_+ \gg k_f$, with energy and wave action being dissipated at rates P_+ and Q_+ , and one at the large scales, say at $k_- \ll k_f$, dissipated at rates P_- and Q_- . Further assume that in between the forcing and dissipation, there exist two distinct

inertial ranges where neither forcing or dissipation takes effect. In the weakly nonlinear regime, the energy flux is related to the wave action flux by $P_{\mathbf{k}} \approx \omega_{\mathbf{k}} Q_{\mathbf{k}} = k^2 Q_{\mathbf{k}}$. In a non-equilibrium statistical steady state, the energy and wave action balance implies that

$$P_f = P_- + P_+, \quad Q_f = Q_- + Q_+, \quad (36)$$

and therefore, we approximately have

$$P_f \approx k_f^2 Q_f, \quad P_- \approx k_-^2 Q_-, \quad P_+ \approx k_+^2 Q_+. \quad (37)$$

Subsequently, the balance equations (36) imply

$$k_f^2 Q_f \approx k_-^2 Q_- + k_+^2 Q_+, \quad Q_f = Q_- + Q_+. \quad (38)$$

Re-arranging equations (38) enables us to predict at which rates the energy and wave action fluxes are dissipated at the two sinks. From equations (38) we obtain

$$Q_+ \approx \frac{k_f^2 - k_-^2}{k_+^2 - k_-^2} Q_f, \quad Q_- \approx \frac{k_f^2 - k_+^2}{k_-^2 - k_+^2} Q_f. \quad (39)$$

If we consider the region around large scales, $k_- \ll k_f < k_+$, then the first equation in (39) implies $k_f^2 Q_f \approx k_+^2 Q_+$, i.e. that energy is mostly absorbed at the region around k_+ . Furthermore, considering the region around small scales, $k_- < k_f \ll k_+$, the second equation in (39) implies that $Q_f \approx Q_-$, i.e. that wave action is mostly absorbed at regions around k_- . Ultimately, if we force the system at an intermediate scale, where there exists two inertial ranges either side of k_f , we should expect to have that the majority of the energy flowing towards small scales and the majority of the wave action flowing towards large scales. This determines the dual cascade picture of the six-wave system illustrated in figure 14.

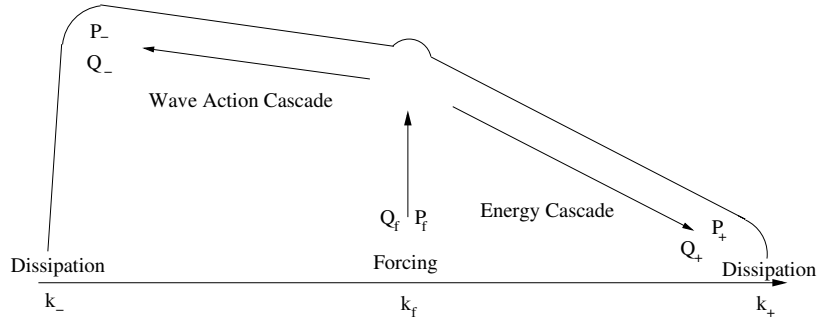


Figure 14: A Graphic to show the development of the the dual cascade regime for 1D OWT.

3.4. The Zakharov Transform and the Power-Law Solutions

To formally derive the thermodynamic and KZ solutions of the KE we will use the Zakharov transform (ZT). This requires that the interaction coefficients of the system are *scale invariant*. Scale invariance of an interaction coefficient is reflected by its self-similar form when the length scales are multiplied by a common factor, i.e. for any real

number $\lambda \in \mathbb{R}$, we say that an interaction coefficient is scale invariant with a *homogeneity coefficient* $\beta \in \mathbb{R}$, if

$$\mathcal{W}(\lambda \mathbf{k}_1, \lambda \mathbf{k}_2, \lambda \mathbf{k}_3, \lambda \mathbf{k}_4, \lambda \mathbf{k}_5, \lambda \mathbf{k}_6) = \lambda^\beta \mathcal{W}(\mathbf{k}_1, \mathbf{k}_2, \mathbf{k}_3, \mathbf{k}_4, \mathbf{k}_5, \mathbf{k}_6). \quad (40)$$

Moreover, the frequency ω_k must also possess the scale invariant property, i.e.

$$\omega(\lambda \mathbf{k}) = \lambda^\alpha \omega(\mathbf{k}), \quad (41)$$

with some $\alpha \in \mathbb{R}$. For OWT this is indeed the case. Since for OWT we have $\omega(\mathbf{k}) \propto k^2$, we see that $\alpha = 2$. Let us now seek solutions of the KE with a power-law form,

$$n_{\mathbf{k}} = C k^{-x}, \quad (42)$$

where C is the constant prefactor of the spectrum, whose physical dimension is determined by the dimensional quantities within the system, and x is the exponent of the spectrum.

An informal way in determining the exponent x of the KZ and thermodynamic solutions is to apply a dimensional analysis argument. For the thermodynamic equilibrium solutions, we assume a zero flux, i.e. that both $\epsilon_{\mathbf{k}}$ and $n_{\mathbf{k}}$ are scale independent. Conversely, for the derivation of the KZ solutions, we want to consider a wave action density scaling that implies a constant flux of the cascading invariant. This is achieved by considering $P_{\mathbf{k}}, Q_{\mathbf{k}} \propto k^0$ in equations

$$P_{\mathbf{k}} = \int^{\mathbf{k}} \frac{\partial \epsilon_{\mathbf{k}'}}{\partial z} d\mathbf{k}', \quad (43a)$$

$$Q_{\mathbf{k}} = \int^{\mathbf{k}} \frac{\partial n_{\mathbf{k}'}}{\partial z} d\mathbf{k}', \quad (43b)$$

(see (35)), using the power-law ansatz (42) and the KE, (34). However, this method does not allow for the evaluation of the prefactor of the spectrum in (42). Therefore, we will now describe the formal way of calculating the KE solutions by using the ZT. The ZT expresses the KE in such a way that it overlaps sub-regions of the KE's domain of integration, thus at each solution, the integrand of the collision integral is set exactly to zero over the whole domain [3]. The ZT takes advantage of the symmetries possessed within the KE by a change of variables. In our case, this results in splitting the domain of the KE into six sub-regions.

Applicability of the ZT requires the locality of wave interactions, namely that only waves with a similar magnitude of wave number will interact. The criterion of locality is equivalent to the convergence of the collision integral. Locality of these solutions will be checked in the following Section.

The ZT is a change of variables on specific sub-regions of the domain, one such sub-region is transformed by

$$\mathbf{k}_2 = \frac{\mathbf{k}^2}{\tilde{\mathbf{k}}_2}, \quad \mathbf{k}_3 = \frac{\mathbf{k}\tilde{\mathbf{k}}_3}{\tilde{\mathbf{k}}_2}, \quad \mathbf{k}_4 = \frac{\mathbf{k}\tilde{\mathbf{k}}_4}{\tilde{\mathbf{k}}_2}, \quad \mathbf{k}_5 = \frac{\mathbf{k}\tilde{\mathbf{k}}_5}{\tilde{\mathbf{k}}_2} \quad \text{and} \quad \mathbf{k}_6 = \frac{\mathbf{k}\tilde{\mathbf{k}}_6}{\tilde{\mathbf{k}}_2}, \quad (44)$$

with the Jacobian of the transformation $J = -\left(\mathbf{k}/\tilde{\mathbf{k}}_2\right)^6$. We must apply four similar transformations, to each of the remaining sub-regions (these are presented in Appendix C).

Using the scale invariant properties of the interaction coefficients and frequency, and the fact that a Dirac delta function scales as

$$\delta((\lambda \mathbf{k})^\alpha) = \lambda^{-\alpha} \delta(\mathbf{k}^\alpha), \quad (45)$$

the ZT implies that the KE can be expressed as

$$\begin{aligned} \dot{n}_{\mathbf{k}} &= \frac{C^5 \epsilon^8 \pi}{6} \int |\mathcal{W}_{4,5,6}^{\mathbf{k},2,3}|^2 |\mathbf{k} \mathbf{k}_2 \mathbf{k}_3 \mathbf{k}_4 \mathbf{k}_5 \mathbf{k}_6|^{-x} \{k^x + k_2^x + k_3^x - k_4^x - k_5^x - k_6^x\} \\ &\times \left[1 + \left(\frac{k_2}{k}\right)^y + \left(\frac{k_3}{k}\right)^y - \left(\frac{k_4}{k}\right)^y - \left(\frac{k_5}{k}\right)^y - \left(\frac{k_6}{k}\right)^y \right] \\ &\times \delta_{4,5,6}^{\mathbf{k},2,3} \delta(\omega_{4,5,6}^{k,2,3}) d\mathbf{k}_2 d\mathbf{k}_3 d\mathbf{k}_4 d\mathbf{k}_5 d\mathbf{k}_6, \end{aligned} \quad (46)$$

where we have omitted the tildes and $y = 5x - 3 - 2\beta$. We see that if $x = 0$ or $x = 2$, the integrand will vanish as we have zero by cancellation in either the curly brackets or in the square brackets (taking into account the Dirac delta function involving frequencies). In particular, when $x = 0$ or $x = 2$, the solutions will correspond to thermodynamic equilibria of the equipartition of the energy and the wave action respectively:

$$n_{\mathbf{k}}^{\text{T}} = C_{\mathcal{H}}^{\text{T}} k^{-2}. \quad (47a)$$

$$n_{\mathbf{k}}^{\text{T}} = C_{\mathcal{N}}^{\text{T}} k^0, \quad (47b)$$

Solutions (47) correspond to zero flux states - in fact both energy and wave action fluxes, $P_{\mathbf{k}}$ and $Q_{\mathbf{k}}$ are identically equal to zero on both equilibrium solutions. Spectra (47) are two limiting cases, in low and high wave number regions, of the more general thermodynamic equilibrium Rayleigh-Jeans solution

$$n_{\mathbf{k}}^{\text{RJ}} = \frac{T_c}{\omega_k + \mu}. \quad (48)$$

Here T_c is the characteristic temperature of the system, and μ is a chemical potential.

In addition to these thermodynamic solutions, our system possesses two non-equilibrium KZ solutions. The KZ solutions are obtained from equation (46) when either $y = 0$ or $y = 2$. When either condition is met, the integrand in equation (46) vanishes due to cancellation in the square brackets. The corresponding solution for the direct energy cascade from low to high wave numbers is obtained when $y = 2$, this gives the following wave action spectrum scaling:

$$n_{\mathbf{k}}^{\mathcal{H}} = C_{\mathcal{H}} k^{-\frac{5+2\beta}{5}}, \quad (49a)$$

where β is the homogeneity parameter, which we will specify later depending on the LWE or SWE regime considered.

Note that in the experiment we do not have direct access to $n_{\mathbf{k}}$ but we measure instead the spectrum $N(\mathbf{k}, z) = |I_{\mathbf{k}}(z)|^2$ of the light intensity. In Appendix I we present how the scaling for $N_{\mathbf{k}}$ in the inverse cascade state is easy to obtain from the scaling of $n_{\mathbf{k}}$ under the random phase condition.

The wave action spectrum (49a) implies that the energy flux $P_{\mathbf{k}}$ is \mathbf{k} -independent and non-zero. The solution for the inverse wave action cascade from high to low wave numbers is obtained when $y = 0$, and is of the form

$$n_{\mathbf{k}}^{\mathcal{N}} = C_{\mathcal{N}} k^{-\frac{3+2\beta}{5}}. \quad (49b)$$

On each KZ solution, the respective flux is a non-zero constant - reflecting the Kolmogorov scenario, whilst the flux of the other invariant is absent. However, we emphasize that the KZ solutions are only valid if they correspond to local wave interactions - an assumption of the ZT.

The main contribution to the six-wave interaction coefficient in the LWE, after application of the CT and expansion in small kl_ξ (see Appendix D), is \mathbf{k} -independent:

$${}^L\mathcal{W}_{4,5,6}^{1,2,3} \approx \frac{9}{4\tilde{\psi}^4 l_\xi^2}. \quad (50)$$

This implies that the homogeneity coefficient for the LWE is $\beta^L = 0$.

Therefore, equations (49) imply that the KZ solutions for the LWE are given by

$${}^L n_{\mathbf{k}}^{\mathcal{H}} = C_{\mathcal{H}}^L \left(\frac{\tilde{\psi}^2 l_\xi}{2} \right)^{4/5} P_{\mathbf{k}}^{1/5} k^{-1}, \quad (51a)$$

$${}^L n_{\mathbf{k}}^{\mathcal{N}} = C_{\mathcal{N}}^L \left(\frac{\tilde{\psi}^2 l_\xi}{2} \right)^{4/5} Q_{\mathbf{k}}^{1/5} k^{-3/5}, \quad (51b)$$

where ${}^L n_{\mathbf{k}}^{\mathcal{H}}$, is the KZ spectrum for the direct energy cascade, and ${}^L n_{\mathbf{k}}^{\mathcal{N}}$ is the inverse wave action spectrum. Here, $C_{\mathcal{H}}^L$ and $C_{\mathcal{N}}^L$ are dimensionless constant pre-factors of the spectra.

Conversely, for the SWE we see that the four-wave interaction coefficient, ${}^S T_{3,4}^{1,2}$, is scale invariant and scales as $\propto k^{-2}$. Formula (25), implies that the homogeneity coefficient for the SWE is $\beta^S = -6$. For both the LWE and SWE we calculated the explicit expressions for the six-wave interaction coefficients using *Mathematica*, and confirmed that $\beta^L = 0$ and $\beta^S = -6$. However we must omit the explicit expression for ${}^S \mathcal{W}_{4,5,6}^{1,2,3}$ in this review as it is extremely long.

Therefore, the SWE yields the following KZ solutions:

$${}^S n_{\mathbf{k}}^{\mathcal{H}} = C_{\mathcal{H}}^S \left(\frac{\tilde{\psi}^2}{2} \right)^{4/5} P_{\mathbf{k}}^{1/5} k^{7/5}, \quad (52a)$$

$${}^S n_{\mathbf{k}}^{\mathcal{N}} = C_{\mathcal{N}}^S \left(\frac{\tilde{\psi}^2}{2} \right)^{4/5} Q_{\mathbf{k}}^{1/5} k^{9/5}, \quad (52b)$$

where, $C_{\mathcal{H}}^S$ and $C_{\mathcal{N}}^S$ are dimensionless constants.

Spectra (51) and (52) are valid solutions only if they correspond to local wave interactions. Therefore we must check that the collision integral converges on these spectra.

3.5. Locality of the Kolmogorov-Zakharov Solutions

The KZ solutions can only be realized if they correspond to local, in \mathbf{k} -space, wave interactions. This entails checking that the collision integral converges, when the wave action density is of KZ type, (49). Our strategy for determining the locality of the KZ solutions is to check the convergence of the collision integral when one wave number vanishes, or when one wave number diverges to $\pm\infty$. These limits correspond to the

convergence of the collision integral in the infrared (IR) and ultraviolet (UV) regions of \mathbf{k} -space respectively. Although the collision integral is five-dimensional (5D), the two Dirac delta functions, relating to the six-wave resonance condition, imply that integration is over a 3D surface within the 5D domain. For linear frequencies of the form, $\omega_k \propto k^2$, we can parametrize the six-wave resonance condition in terms of four variables (see Appendix A), which subsequently allows us to neglect two of the integrations in (34).

The details of the locality analysis is situated in Appendix E. We performed the analysis using the `Mathematica` package, which allowed us to handle and simplify the vast number terms resulting from the CT. Assuming that the six-wave interaction coefficient has the following scaling as $k_6 \rightarrow 0$, $\lim_{k_6 \rightarrow 0} \mathcal{W}_{4,5,6}^{\mathbf{k},1,2} \propto k_6^\xi$, where $\xi \in \mathbb{R}$. Then we find that we have IR convergence of the collision integral if $x < 1 + 2\xi$, is satisfied. Similarly, by assuming that the six-wave interaction coefficient scales with k_6^η as $k_6 \rightarrow \infty$: $\lim_{\mathbf{k}_6 \rightarrow \infty} \mathcal{W}_{4,5,6}^{\mathbf{k},2,3} \propto k_6^\eta$, where $\eta \in \mathbb{R}$, we find that the criterion for UV convergence of the collision integral is $\eta < x$.

We now check for convergence in the OWT models. We begin by investigating the locality on the LWE. The six-wave interaction coefficient ${}^L\mathcal{W}_{4,5,6}^{1,2,3}$ was shown (at leading order) to be constant, with the constant given in equation (50). This implies that in the IR limit ${}^L\mathcal{W}_{4,5,6}^{1,2,3}$ remains constant, i.e. $\xi = 0$. Hence, the condition for IR convergence becomes $x < 1$. Due to relation (50) being constant, we also have that $\eta = 0$, and therefore, the convergence condition for UV is $0 < x$. Therefore, the LWE has local KZ spectra if their exponents are within the region $0 < x < 1$. For the LWE's KZ solutions (51), we have that the direct cascade of energy has the exponent $x = 1$, which implies divergence. However, because this exponent is at the boundary of the convergence region, we have a slow logarithmic divergence of the collision integral. This implies that by making a logarithmic correction to the wave action spectrum (51a), we can prevent divergence of the collision integral - we will consider this in the next Subsection. The inverse cascade of wave action, with $x = 3/5$, implies convergence of the collision integral.

Consideration of the SWE in the IR region, by appropriate Taylor expansion around a vanishing \mathbf{k}_6 using `Mathematica`, reveals that the six-wave interaction coefficient, ${}^S\mathcal{W}_{4,5,6}^{1,2,3}$, behaves as $\lim_{\mathbf{k}_6 \rightarrow 0} {}^S\mathcal{W}_{4,5,6}^{1,2,3} \propto k_6^{-1}$, giving $\xi = -1$. Therefore, the condition for IR convergence of the KZ solutions becomes $x < -1$. Similarly, using `Mathematica` and expanding the interaction coefficient ${}^S\mathcal{W}_{4,5,6}^{1,2,3}$ in the limit where $\mathbf{k}_6 \rightarrow \infty$, we find that $\lim_{\mathbf{k}_6 \rightarrow \infty} {}^S\mathcal{W}_{4,5,6}^{1,2,3} \propto k_6^0$, thus $\eta = 0$. This implies that the UV condition for convergence is the same as that for the LWE. Therefore, there does not exist any region of convergence for the collision integral of the SWE. To be specific, both KZ solutions of the SWE (52), where $x = -7/5$ and $x = -9/5$ for the direct and inverse spectra respectively, we have IR convergence and UV divergence. Therefore, both short-wave KZ spectra are non-local. Non-locality of the KZ solutions implies that the local wave interaction assumption is incorrect, and thus the approach taken to predict these spectra is invalid. However, the development of a non-local theory for the SWE may yield further insight.

3.6. Logarithmic Correction to the Direct Energy Spectrum

In the previous Subsection, the direct energy cascade in the LWE, (51a), was shown to be marginally divergent in the IR limit. This is to say, that the collision integral diverges at a logarithmic rate in the limit of one vanishing wave number. However, by introducing a logarithmic dependence to the KZ solution, we can produce a convergent collision

integral. Following Kraichnan's argument for the logarithmic correction associated to the direct enstrophy cascade in 2D turbulence [63, 64], we assume a correction of the form:

$${}^L n_{\mathbf{k}}^{\mathcal{H}} = C_{\mathcal{H}}^L \left(\frac{\tilde{\psi}^2 l_{\xi}}{2} \right)^{4/5} P_{\mathbf{k}}^{1/5} k^{-1} \ln^{-y}(k\ell), \quad (53)$$

where y is some constant to be found and ℓ is the scale of at which energy is injected. The exponent of the logarithmic power law, y , is calculated by assuming that the energy flux, $P_{\mathbf{k}}$, remains \mathbf{k} -independent. Subsequently, the energy flux can be expressed as

$$P_{\mathbf{k}} = \int^{\mathbf{k}} \omega_k \frac{\partial n_{\mathbf{k}}}{\partial t} d\mathbf{k} \propto \int^{\mathbf{k}} k^4 n_{\mathbf{k}}^5 d\mathbf{k} \propto \int^{\mathbf{k}} k^{-1} \ln^{-5y}(k\ell) d\mathbf{k}, \quad (54)$$

where we have taken into account that the collision integral (34), with interaction coefficients (18), scales as $\dot{n}_{\mathbf{k}} \propto k^2 n_{\mathbf{k}}^5$. Therefore, $P_{\mathbf{k}}$ remains \mathbf{k} -independent³ when $y = 1/5$. This implies that the logarithmically corrected direct energy KZ spectrum is given by

$${}^L n_{\mathbf{k}}^{\mathcal{H}} = C_{\mathcal{H}}^L \left(\frac{\tilde{\psi}^2 l_{\xi}}{2} \right)^{4/5} P_{\mathbf{k}}^{1/5} k^{-1} \ln^{-1/5}(k\ell). \quad (55)$$

Spectrum (55) now produces a convergent collision integral for the LWE and is subsequently a valid KZ solution.

3.7. Linear and Nonlinear Times and The Critical Balance Regime

In this Section, we estimate the nonlinear transfer times in the KZ cascades and discuss the critical balance (CB) states of strong WT. The linear timescale is defined as $T_L = 2\pi/\omega_k$. From the KE, we can define the nonlinear timescale as $T_{\text{NL}} = 1/\frac{\partial \ln(n_{\mathbf{k}})}{\partial t}$. Weak WT theory is applicable when there is a large separation between the linear and nonlinear timescales, i.e. $\frac{T_L}{T_{\text{NL}}} \ll 1$. The estimation of T_{NL} , with respect to k , can be achieved using the KE (34), giving $T_{\text{NL}} \propto k^{4x-2\beta-2}$. Therefore, the condition of applicability can be written as $T_L/T_{\text{NL}} \propto k^{-4x+2\beta} \ll 1$. This can be violated in either of the limits $k \rightarrow 0$ or $k \rightarrow \infty$, depending on the sign of $-4x + 2\beta$. When $T_L/T_{\text{NL}} \sim 1$, then the KE approach breaks down and we are in a strong WT regime.

To describe strong WT in some physical systems the concept of CB was suggested, first in magneto-hydrodynamics (MHD) turbulence [32] and then later in rotating and stratified turbulence [120] and BEC [49]. CB is defined as a turbulent state where the nonlinear evolution time T_{NL} is of the same order as the linear wave period T_L over a large range of scales. A CB scaling for the wave action density, $n_{\mathbf{k}}$, can be made by equating T_{NL} with T_L , on a scale by scale basis, i.e. $T_L/T_{\text{NL}} \propto k^{-4x+2\beta} \sim 1$, implying a CB spectrum

$$n_{\mathbf{k}}^{\text{CB}} = C_{\text{CB}} k^{-\frac{\beta}{2}}, \quad C_{\text{CB}} = \text{const.} \quad (56)$$

For 1D OWT, we estimate the ratio between the linear and nonlinear timescales using the KE of the LWE and SWE. For the LWE, with homogeneity coefficient $\beta^L = 0$,

³The energy flux is actually proportional to $\ln(\ln(k\ell))$.

implies that for both the direct ($x = 1$) and inverse ($x = 3/5$) KZ spectra, the WT criterion $\frac{T}{T_{\text{NL}}} \ll 1$ will gradually be violated as $k \rightarrow 0$. For the direct cascade, the largest scale is at the forcing. Thus, if WT is weak at the forcing scale, it will remain weak everywhere along the cascade. In the inverse cascade, even for weak forcing, the strength of WT is increasing along the cascade toward the lowest wave numbers, resulting in the break down of WT theory and the formation of nonlinear coherent structures. For the SWE, with homogeneity coefficient $\beta^S = -6$, and with KZ exponents $x = -7/5$ and $x = -9/5$ for the direct and inverse KZ spectra respectively, we have a similar situation where condition $\frac{T}{T_{\text{NL}}} \ll 1$ gets violated as the inverse cascade progress to small wave numbers.

3.8. The Differential Approximation and the Cascade Directions

The differential approximation model (DAM) is an approximation of the KE by assuming strongly local wave interactions. This enables the construction of a partial differential equation for the evolution of the wave action density, $n_{\mathbf{k}}$. We stress that the DAM is an approximation and thus can only be justified when the KZ solutions are proved local, i.e. the DAM is only applicable to the KE of the LWE. Therefore, we find that the DAM is only applicable to the KE of the LWE. The DAM contains both the thermodynamic and non-equilibrium KZ solutions of the KE, and can be further simplified to *reduced* DAMs, which only consider a subset of these solutions. The usefulness of the DAM can be shown with derivation of exact analytical expressions for the fluxes and finally by its computational simplicity. The DAM can also be adapted to classical turbulence theory, where it is known as the Leith model [121, 122, 123]. This has led to the DAM being used extensively in WT and classical turbulence [124, 125, 126, 127, 128, 41, 129, 110]. The derivation of the DAM for the LWE can be found in Appendix F. The DAM for 1D OWT is given by

$$\dot{n}_\omega = S_0 \omega^{1/2} \frac{\partial^2}{\partial \omega^2} \left[\omega^{\frac{9}{2}} n_\omega^6 \frac{\partial^2}{\partial \omega^2} \left(\frac{1}{n_\omega} \right) \right]. \quad (57)$$

This equation contains the same steady state solutions (thermodynamic and non-equilibrium) as the KE. The thermodynamic solution, $n_\omega = T_c / (\omega + \mu)$ is found when

$$R_\omega = S_0 \omega^{\frac{9}{2}} n_\omega^6 \frac{\partial^2}{\partial \omega^2} \left(\frac{1}{n_\omega} \right) \quad (58)$$

is identically equal to zero. The energy and wave action fluxes, P_ω and Q_ω , can be derived from R_ω by the following formulae:

$$P_\omega = R_\omega - \omega \frac{\partial R_\omega}{\partial \omega}, \quad (59a)$$

$$Q_\omega = -\frac{\partial R_\omega}{\partial \omega}. \quad (59b)$$

Consequently, both P_ω and Q_ω vanish upon the thermodynamic solution. By assuming the same power-law scaling as for the KE (42), $n_\omega = C \omega^{-x/2}$, we can calculate formulae

for the behavior of the DAM with respect to ω and the exponent x :

$$\dot{n}_\omega = S_0 C^5 \frac{x}{2} \left(\frac{x}{2} - 1 \right) y (y - 1) \omega^{-y - \frac{1}{2}}, \quad (60a)$$

$$R(\omega, x, y) = S_0 C^5 \frac{x}{2} \left(\frac{x}{2} - 1 \right) \omega^{-y+1}, \quad (60b)$$

$$P(\omega, x, y) = S_0 C^5 \frac{x}{2} \left(\frac{x}{2} - 1 \right) y \omega^{-y+1}, \quad (60c)$$

$$Q(\omega, x, y) = S_0 C^5 \frac{x}{2} \left(\frac{x}{2} - 1 \right) (y - 1) \omega^{-y}, \quad (60d)$$

where $y = \frac{5x}{2} - \frac{3}{2}$. Stationary solutions for the DAM are seen when $\dot{n}_\omega = 0$, i.e. when $x = 0$, $x = 2$, $y = 0$ or $y = 1$, yielding the thermodynamic solutions (47) and the KZ solutions of the LWE (51). Relations (60c) and (60d) enable for the calculation of the sign of the KZ fluxes. First, we observe that both fluxes vanish upon reaching the thermodynamic solutions, when $x = 0$ and $x = 2$, and second, that on the KZ solutions, the flux of the non-cascading invariant is zero.

The Fjørtoft argument of Subsection 3.3, showed the directions of \mathbf{k} -space in which energy and wave action are permitted to flow. However, the direction of the invariant cascade in the KZ solution may sometimes contradict Fjørtoft's argument in which case they cannot be matched to any physical forcing and dissipation, and hence, they are not realizable. Therefore, it is essential that the direction of the flux agrees with the analysis of Fjørtoft's argument.

We use the formulation of the DAM in Subsection 3.8, to determine the directions of the energy and wave action fluxes $P_{\mathbf{k}}$ and $Q_{\mathbf{k}}$ within the LWE. By plotting formulae (60c) and (60d) for $P_{\mathbf{k}}$ and $Q_{\mathbf{k}}$ against the exponent of the KZ solution, x , we can determine the sign of the fluxes. When the exponent is that of both thermodynamic solutions (47), then both fluxes should vanish.

In figure 15, we plot equations (60), for $P_{\mathbf{k}}$ and $Q_{\mathbf{k}}$. we observe that at $x = 0, 2$ corresponding to the two thermodynamic equilibrium solutions, we have both the energy and wave action fluxes identically zero. At $x = 3/5$, corresponding to the wave action cascade, we have that the energy flux $P_{\mathbf{k}}$ is zero, whilst the wave action flux $Q_{\mathbf{k}}$ is *positive*. When $x = 1$, the exponent for the energy cascade, we have the wave action flux $Q_{\mathbf{k}}$ is zero, and the energy flux $P_{\mathbf{k}}$ is *negative*. However, to agree with Fjørtoft's argument, when $x = 1$, the energy flux must be *positive* and the wave action flux zero. Similarly, when the exponent agrees with the KZ exponent of the inverse cascade, (51b), Fjørtoft's argument implies that the wave action flux must be *negative*. Thus, we should not expect realizability of the pure KZ solutions. The authors of [50] suggest that in such situations, we might expect to observe *finite temperature cascade* solutions. Such "warm cascades" were studied in the example of the Boltzmann kinetics in [130] and in the BEC WT context in [56]. These solutions are predominantly thermodynamic ones similar to (48), but with a correction which is small in the inertial range and which causes a sharp falloff at the dissipation scale. A remarkable feature of the warm cascade is that its temperature is independent of the forcing rate, but dependent only on the wave numbers of the forcing and the dissipation.

3.9. Modulational Instability and Solitons in the Long-Wave Equation

The similarity of the LWE (7) to the integrable 1D focusing NLSE (5) means that we should expect not only random waves but also soliton-like coherent structures. During the

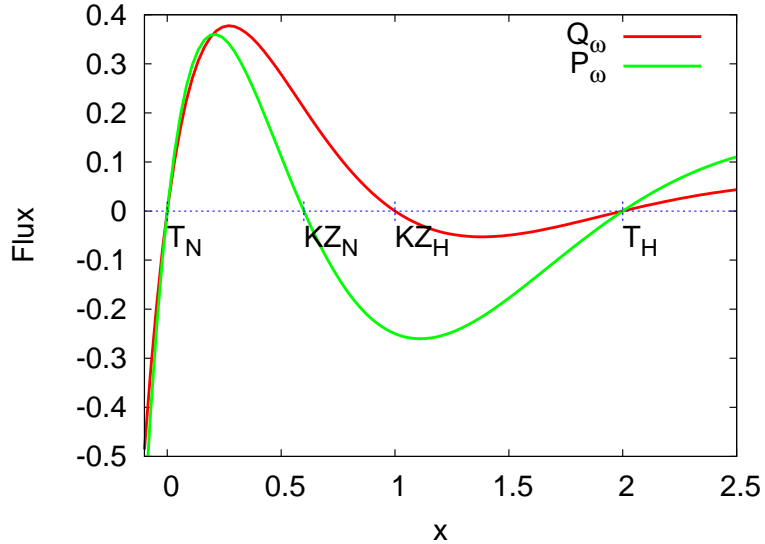


Figure 15: Plot of the energy flux P_ω and wave action flux Q_ω against the exponent x of the power law distribution of $n_\omega = C\omega^{-x/2}$ in the DAM representation of the LWE.

inverse cascade, solitons appear naturally as wave action reaches the low wave numbers. Indeed, the KE description (34) becomes invalid, and the MI of the wave field occurs resulting in the filamentation of light and its condensation into solitons.

Solitons are localized (in physical space) structures resulting from the balance between the dispersion of the wave and the nonlinear beam self-focusing. Solitons appear in several nonlinear wave equations, with the 1D NLSE one example. The 1D NLSE (5) can be solved exactly by the inverse scattering transform. Analytical soliton solutions of equation (5) have the form

$$\psi_{sol}(x, z) = 2Al_\xi \tilde{\psi} \operatorname{sech} \left(Ax - \frac{ABz}{q} + C_1 \right) \exp \left(i \left[Bx + \frac{(A^2 - B^2)z}{2q} + C_2 \right] \right), \quad (61)$$

where A , B , C_1 and C_2 are constants.

Unlike equation (5), the LWE, (7), is non-integrable, and thus, will not possess exact analytical solutions of form (61). However, the LWE's deviation from NLSE is small, so we would expect to observe coherent structures of the LWE to be similar in shape to (61). Moreover, solitons of integrable systems possess the property of passing through one another without changing shape. However, when integrability is slightly violated, we expect to observe weak nonlinear interactions between solitons. This may be observed as possible merging events, oscillations in profile or interactions with weak random waves.

Formally, 1D NLSE solitons are defined as solutions to (5) of the form [71]

$$\psi_{sol}(x, z) = e^{i\Omega z/2q} \phi \left(x - \frac{Vz}{2q} \right), \quad (62)$$

i.e. that the structure of the soliton is preserved as it propagates along the z -axis by some

velocity V . The Fourier transform of $\phi(x, z)$ satisfies the following integral equation:

$$\phi_{\mathbf{k}} = -\frac{1}{2(\Omega - \mathbf{k}V + \omega_k)} \int T_{3,4}^{\mathbf{k},2} \phi_2^* \phi_3 \phi_4 \delta_{3,4}^{\mathbf{k},2} d\mathbf{k}_2 d\mathbf{k}_3 d\mathbf{k}_4, \quad (63)$$

with $T_{3,4}^{1,2}$, in the case of the 1D NLSE, given by the first term of equation (18b), i.e. constant. If the denominator of $\phi_{\mathbf{k}}$ in equation (63) has no zeros for $\mathbf{k} \in \mathbb{R}$, then solitons may be present in the system. If in equation (63) the numerator and denominator contain only one zero each at $\mathbf{k} = 0$ then solitons may also exist. For OWT, when $\omega_k = k^2$, there exist soliton parameters Ω and V for which the denominator is not zero. This corresponds to the cases when on the (\mathbf{k}, ω) -plane, the line $\omega = \mathbf{k}V - \Omega$ lies below the parabola $\omega = \omega_k = k^2$ without intersecting it. Such parameters correspond to non-radiating solitons. Let us emphasize an important difference with systems for which there exist no straight lines on the (\mathbf{k}, ω) -plane non-intersecting with the dispersion curve, as it is the case e.g. for the gravity waves, where $\omega_k = k^{1/2}$, and for a the MMT model with the same dispersion relation [71, 91]. In the latter cases quasi-soliton structures are possible, but they have only a finite life time because they decay via radiating weak waves in a way similar to Cherenkov radiation [91]. In contrast, there is no radiation of waves by solitons in our optical system, except during the soliton-soliton collisions (the latter do create wave ripples due to the weak non-integrability of the system). In fact, we will see that the dominant interactions are in the opposite direction: the waves “condense” into solitons with resonant parameters Ω and V i.e. such that the line $\omega = \mathbf{k}V - \Omega$ is tangentially touching the parabola $\omega = \omega_k$. Subsequent evolution brings these lines further down thus decoupling the solitons from the weak waves. Hence, the solitons act as optical “vacuum cleaners” which absorb “optical dirt” - the background noise consisting of weak random waves.

In figure 16, we plot the profile of the NLSE soliton (61), with the corresponding wave action spectrum given in figure 17. We observe a scaling of $n_{\mathbf{k}} \propto k^0$ towards low wave numbers, with a decline of the spectrum at large k . However, a $n_{\mathbf{k}} \propto k^0$ scaling is also observed from the equipartition of wave action (47). Therefore, by mere observation of the wave action spectrum, $n_{\mathbf{k}}$, it will be difficult to determine if the wave field is comprised of equilibrated random waves or if is in the presence of solitons. To distinguish between these two states, we can numerically produce a (\mathbf{k}, ω) -plot, that involves an additional Fourier transform over a time window. This method separates the random waves from the coherent component by observation of the dispersion relation, ω_k [51, 47, 49].

The inverse cascade of photons is an essential step in the creation of solitons from a weakly nonlinear random wave field. The cascade provides the means, via nonlinear wave interaction, for wave action to reach large scales. As the inverse cascade develops, the nonlinearity of the system increases and a condensate forms, resulting in the dynamics of random waves deviating from the linear dispersion relation to one that is Bogoliubov modified. In the LWE, this condensate is unstable, and undergoes MI resulting in the formation of solitons. To derive an expression for the Bogoliubov dispersion relation, we must first expand the wave function $\psi(x, z)$ around a homogeneous condensate solution. The Bogoliubov dispersion relation then comprises of the wave frequency for the disturbances upon the condensate. Its derivation can be found in Appendix G. The dispersion

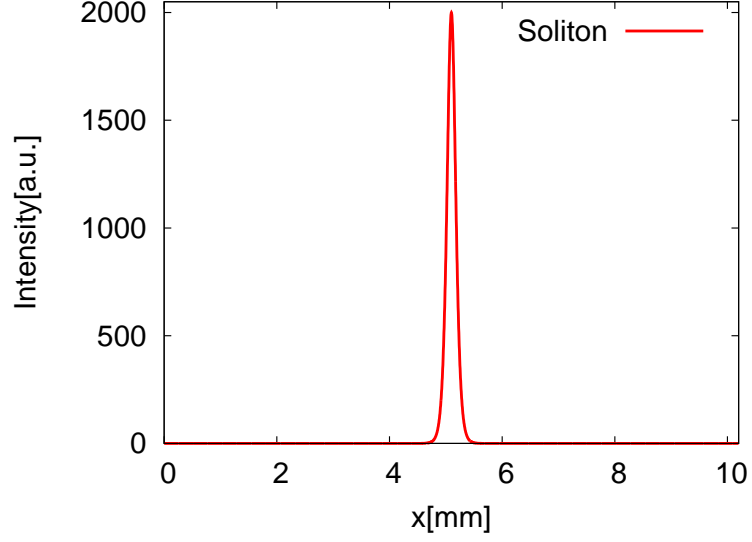


Figure 16: Intensity profile of the 1D NLSE soliton profile given in equation (61).

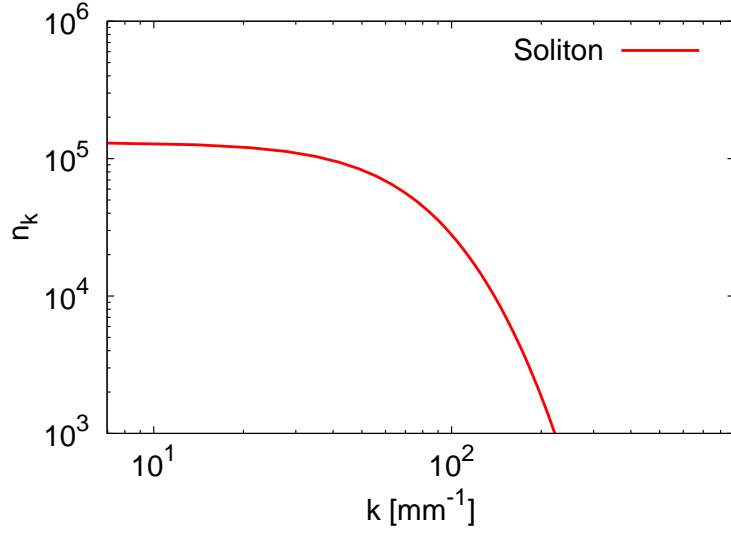


Figure 17: The corresponding wave action spectrum for the soliton profile in figure 16

relation is

$$\begin{aligned}
 \omega_k^B &= \omega_c + \Omega_k \\
 &= -\frac{I_0}{2\tilde{\psi}^2 l_\xi^2} + \sqrt{\frac{\left(1 + \frac{I_0}{\tilde{\psi}^2}\right) k^4 - \frac{I_0}{\tilde{\psi}^2 l_\xi^2} k^2}{36}},
 \end{aligned} \tag{64}$$

where $I_0 = |\psi_0|^2$ is the intensity of the condensate. We observe that the Bogoliubov dispersion relation (64) is the linear wave frequency $\omega_k = k^2$ (when $I_0 = 0$) with a correction due to the formation of the condensate. Frequency (64) becomes complex when the term inside the square root turns negative. This gives a condition for the MI,

$$k^2 < \frac{I_0}{(\tilde{\psi}^2 + I_0)l_\xi^2}. \quad (65)$$

It is MI that precedes and assists the formation of solitons when WT fails to remain weak at large scales. Note that the large scale condensate is not necessarily uniform in the physical space - it may contain a range of excited large-scale modes. However, such a condensate will be felt as quasi-uniform by modes with \mathbf{k} significantly exceeding the lowest wave numbers. Thus, it is best to generalize the definition of the condensate intensity. In fact, we found that the best agreement of the Bogoliubov dispersion relation to the numerical (\mathbf{k}, ω) -plot (figure 23) was achieved when we take I_0 to equal the intensity of the soliton component, i.e. the wave action contained in the region $-\omega_{\max}/2 < \omega < 0$. Note that other classical examples of MI are also found in the context of water waves, where it is known as the Benjamin-Feir instability [131], and in the Rossby/drift waves [132].

Consideration of a single 1D NLSE soliton defined by equation (61), in an infinitely long domain, allows for the analytical computation of the conserved quantities of the 1D NLSE system. This will provide some insight into the behavior of solitons in the LWE. Calculation of the two energy contributions in the NLSE Hamiltonian are given by

$$\mathcal{H}_2 = \int_{-\infty}^{\infty} \left| \frac{\partial \psi_{\text{sol}}}{\partial x^2} \right|^2 dx = \frac{8A\tilde{\psi}^2 l_\xi^2 (A^2 + 3B^2)}{3}, \quad (66a)$$

$$\mathcal{H}_4 = -\frac{1}{4\tilde{\psi}^2 l_\xi^2} \int_{-\infty}^{\infty} |\psi_{\text{sol}}|^4 dx = -\frac{16A^3 \tilde{\psi}^2 l_\xi^2}{3}. \quad (66b)$$

Although, exact NLSE solitons do not interact, solitons in the LWE will because of the additional non-integrable term. Therefore, we will most probably observe behavior such as growing, shrinking, merging and collapsing. If we consider the A -dependence of equations (66), then we observe that the nonlinear energy of the soliton increases at twice the rate (with respect to A) compared to the linear energy. However, for the system to conserve energy, the linear and nonlinear energies must remain balanced for all time (with their sum equal to some initial energy, E_0). From (66) this initial energy is given by

$$\mathcal{H}_{\text{sol}} = E_0 = \frac{8\tilde{\psi}^2 l_\xi^2 A (3B^2 - A^2)}{3}. \quad (67)$$

For the same energy, equation (67) implies the relation

$$B = \sqrt{\frac{E_0}{3A} + \frac{A^2}{3}}, \quad (68)$$

i.e. for the soliton to grow in amplitude A , it must also increase its speed $\sim B/q$, in order to compensate for the balance between the linear and nonlinear energies. However, this would increase the wave action \mathcal{N} and the linear momentum \mathcal{M} - another conserved

quantity of the system. Therefore, an important question to ask is, can two solitons merge, while wave action, energy, and linear momentum remain conserved?

The answer to this is yes, but only if the merging of two solitons generate waves. Let us prove this fact. Consider two solitons with parameters $\{A_1, B_1\}$ and $\{A_2, B_2\}$, that defines their amplitude and speed respectively, and then assume that the two solitons merge into one soliton defined by $\{A_3, B_3\}$, see figure 18 for an illustration,

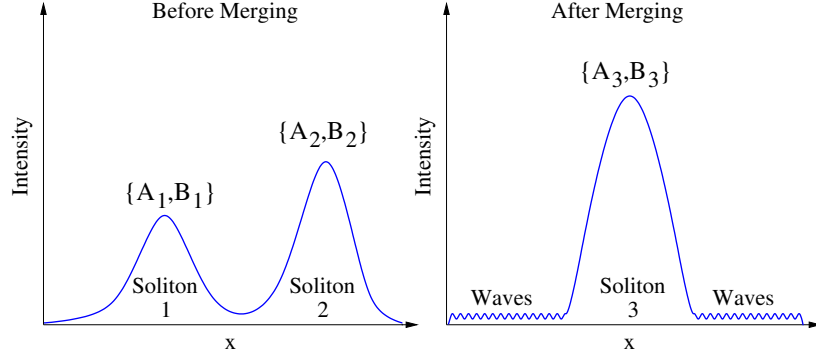


Figure 18: Graphic to show the before and after states from a soliton merger. On the left image we see two solitons with parameters $\{A_1, B_1\}$ and $\{A_2, B_2\}$, while after we see only one soliton defined by $\{A_3, B_3\}$ but with the generation of waves, with the wave energy being determined by equation (73).

The wave action \mathcal{N} of a soliton is defined as

$$\mathcal{N}_{\text{sol}} = \int_{-\infty}^{\infty} |\psi_{\text{sol}}|^2 dx = 4A\tilde{\psi}^2 l_{\xi}^2, \quad (69)$$

and its momentum \mathcal{M} is given by

$$\mathcal{M}_{\text{sol}} = \frac{i}{2} \int_{-\infty}^{\infty} \left(\psi_{\text{sol}} \frac{\partial \psi_{\text{sol}}^*}{\partial x} - \psi_{\text{sol}}^* \frac{\partial \psi_{\text{sol}}}{\partial x} \right) dx = 8AB\tilde{\psi}^2 l_{\xi}^2. \quad (70)$$

Conservation of the total wave action and the total momentum of two solitons imply that

$$A_3 = A_1 + A_2, \quad (71a)$$

$$B_3 = \frac{A_1 B_1 + A_2 B_2}{A_1 + A_2}, \quad (71b)$$

must hold during the merging event. Now if we consider the total energy conservation, but include a term that describes the generation of energy associated to waves $\mathcal{H}_{\text{waves}}$ (it is reasonable to assume that low amplitude waves do not significantly contribute to the total wave action and the momentum of the system). Then the conservation of energy implies

$$\mathcal{H}_{\text{sol1}} + \mathcal{H}_{\text{sol2}} = \mathcal{H}_{\text{sol3}} + \mathcal{H}_{\text{waves}}, \quad (72)$$

where $\mathcal{H}_{\text{sol}i}$ is the energy defined by equation (67) of soliton i . Then using (71), (72) and (67), we have that the energy that is generated into waves is given by

$$\mathcal{H}_{\text{waves}} = \frac{8\tilde{\psi}^2 l_{\xi}^2 A_1 A_2 \left[(A_1 + A_2)^2 + (B_1 - B_2)^2 \right]}{38 A_1 + A_2}. \quad (73)$$

Equation (73) states the amount of energy that is transferred to waves from the soliton merging event and is solely determined by the parameters of the initial (pre-merging) solitons. Furthermore, equation (73) implies that there *must* be waves generated from the merging of two solitons. If there were no waves created from the interaction, then the only solution to (73) would imply $A_1 = 0$ or $A_2 = 0$, i.e. one of the two initial solitons is absent. Therefore, we can expect the behavior of the LWE to be as follows: As wave action reaches the largest scale by the inverse cascade, solitons begin to emerge via MI. As these solitons evolve, they grow in size by absorbing wave action from waves and by merging with other solitons. But by merging with other solitons, the interaction emits low intensity random linear waves back into the system. This process proceeds until there is only a single soliton remaining surrounded by a field of random linear waves.

4. Numerical results and comparison with the experiment

We present the numerical results for OWT. After presenting the numerical method, we divide this Section into two main parts, firstly, we consider the system described by the LWE in its numerical aspect and compare with the experimental results. We begin this Subsection by considering the decaying setup with condensation at the lowest wave numbers. Then we move on to the numerical simulations of the LWE in the forced and dissipated regime. In the final Subsection, we present the numerical results for the SWE.

4.1. The Numerical Method

For the numerical computation of the LWE and the SWE, we implement a pseudo-spectral method [133, 134], with a resolution of $N = 2^{12}$ Fourier modes. The scheme utilizes the fast Fourier transform to convert physical space vectors into their Fourier representation, where differentiation of the wave field is transformed to algebraic multiplication by wave number \mathbf{k} . The linear terms are solved exactly in Fourier space and then converted back into physical space with the aid of integrating factors, to greatly improve the numerical stability. Nonlinear terms are more complicated. Multiplications involving $\psi(x, z)$, have to be performed in physical space. Moreover, multiplication produces aliasing errors, due to the periodicity of the Fourier series expansion of the solution. These errors can be removed by artificially padding the Fourier mode representation with wave number modes of zero amplitude at either ends of \mathbf{k} -space. The amount of de-aliasing is subject to the degree of nonlinearity of the equation. For us, this entails that half of the wave number resolution for the solution needs to be zero - a quarter at each end of \mathbf{k} -space [134].

We evolve the simulations in time by using the fourth order Runge-Kutta method [134], using a time step that is small enough so that it satisfies the Courant-Friedrichs-Lewy (CFL) condition of

$$\max_{\mathbf{k}} \left(\frac{\partial \omega_{\mathbf{k}}}{\partial \mathbf{k}} \right) \Delta t < \Delta x, \quad (74)$$

where $\Delta x = L/N$ is the spacing of our spatial grid and $L = 32\pi$, is the length of our periodic box. Numerically we compute the non-dimensionalized equation given by

$$i \frac{\partial \psi}{\partial z} = - \frac{\partial^2 \psi}{\partial x^2} + N(\psi) + i(F_{\mathbf{k}} - D_{\mathbf{k}}), \quad (75)$$

where $N(\psi)$ represents the nonlinear part of our equations. Appendix H includes the derivation of the non-dimensional versions of both the LWE and SWE. The non-dimensional LWE contains an adjustable parameter α , defined in Appendix H. For the decaying setup, we set $\alpha = 128$, so that the numerical simulation is in the same regime as the experiment. For the forced and dissipated cases, we set $\alpha = 1024$, so that the long-wave limit is better realized. $F_{\mathbf{k}} = F(\mathbf{k})$ is the forcing profile, where energy and wave action are injected into the system. We define this in Fourier space, over a specific range of wave numbers. For the direct cascade simulations we use a forcing profile given by

$$F_{\mathbf{k}}^{\text{direct}} = \begin{cases} A \exp(i\theta_{\mathbf{k}}) & \text{if } 9 \leq \frac{k}{\Delta k} \leq 11 \\ 0 & \text{otherwise,} \end{cases} \quad (76)$$

where A is the amplitude of forcing and $\theta_{\mathbf{k}}$ is a random variable chosen from a uniform distribution on $[-\pi, \pi)$ at each wave number and at each time step and $\Delta k = 2\pi/L$ is the Fourier grid spacing. For the inverse cascade simulations, we apply forcing over a small range of wave numbers situated in the high wave number region. However, we must allow for some Fourier modes with wave numbers larger than the forcing ones, because some direct cascade range is necessary for the development of the inverse cascade. Our forcing profile for the inverse cascade simulations is given by

$$F_{\mathbf{k}}^{\text{inverse}} = \begin{cases} A \exp(i\theta_{\mathbf{k}}) & \text{if } \frac{N}{16} - 10 \leq \frac{k}{\Delta k} \leq \frac{N}{16} + 10 \\ 0 & \text{otherwise.} \end{cases} \quad (77)$$

In all simulations, we dissipate at high wave numbers by adding a hyper-viscosity term $\propto \mathbf{k}^4 \psi_{\mathbf{k}}$. We use the fourth power of \mathbf{k} , so that the dissipation profile is not too steep for the formation of a bottleneck, or too shallow as to prevent a large enough inertial range developing. At low wave numbers, we use two types of dissipation profile. Firstly, we can use a hypo-viscosity term $\propto \mathbf{k}^{-4} \psi_{\mathbf{k}}$. However, this type of dissipation profile in the 3D NLSE model has led to the WT description becoming invalid and a CB regime to develop [49]. In these situations, the CB scenario is avoided by the use of low wave number friction.

To summarize, our numerical dissipation profile $D_{\mathbf{k}} = D(\mathbf{k})$, removes wave action and energy from the system at low and high wave numbers. For clarity, we split $D_{\mathbf{k}}$ into the low and high wave number contributions $D_{\mathbf{k}}^L$ and $D_{\mathbf{k}}^H$. At high wave numbers our hyper-viscosity profile is defined as

$$D_{\mathbf{k}}^H = \nu_{\text{hyper}} \mathbf{k}^4 \psi_{\mathbf{k}}, \quad (78a)$$

where ν_{hyper} is the coefficient for the rate of dissipation. If we apply hypo-viscosity at low wave numbers, then $D_{\mathbf{k}}^L$ is given by

$$D_{\mathbf{k}}^L = \begin{cases} \nu_{\text{hypo}} \mathbf{k}^{-4} \psi_{\mathbf{k}} & \text{if } \mathbf{k} \neq 0 \\ \psi_{\mathbf{k}} = 0 & \text{if } \mathbf{k} = 0, \end{cases}$$

where ν_{hypo} is the coefficient for the rate of dissipation at low wave numbers. However, in situations where we use friction, then $D_{\mathbf{k}}^L$ is defined as

$$D_{\mathbf{k}}^L = \begin{cases} \nu_{\text{friction}} \psi_{\mathbf{k}} & \text{if } 0 \leq k \leq 6 \\ 0 & \text{otherwise,} \end{cases}$$

where ν_{friction} is the rate of friction dissipation.

4.2. The Long-Wave Equation

4.2.1. The Decaying Inverse Cascade with Condensation

The decaying simulation leading to photon condensation was originally reported by us in [51]. Both experimental and numerical setups are configured for decaying OWT, where an initial condition is set up and allowed to develop in the absence of any forcing or artificial dissipation. We perform the numerical simulation with the same parameters as the experiment, and present results in dimensional units for comparison.

The inverse cascade spectrum is of a finite capacity type, in a sense that only a finite amount of the cascading invariant (wave action in this case) is needed to fill the infinite inertial range. Indeed, this is determined as the integral of the wave action spectrum $n_{\mathbf{k}}$ converges at $\mathbf{k} = 0$, i.e.

$$\int_0 n_{\mathbf{k}} dk \propto \int_0 k^{-3/5} dk < \infty. \quad (79)$$

For finite capacity spectra, the turbulent systems have a long transient (on its way to the final thermal equilibrium state) in which the scaling is of the KZ type (provided this spectrum is realizable, i.e. local and agrees with Fjørtoft). This is because the initial condition serves as a huge reservoir of the cascading invariant.

Experimentally, the initial condition is setup by injecting photons at small spatial scales by modulating the intensity of the input beam with a patterned intensity mask. We randomize the phases by the use of a phase modulator. This is made by creating a random distribution of diffusing spots with the average size $\simeq 35 \mu m$ through the SLM. This is done in order to create an initial condition close to a RPA wave field required by the theory. The numerical initial condition is more idealized. We restrict the initial condition to a localized region at small scales. The initial profile is given by

$$\psi_{\mathbf{k}}(0) = \begin{cases} A \exp(i\theta_{\mathbf{k}}) & \text{if } \frac{N}{16} - 5 < \frac{k}{\Delta k} < \frac{N}{16} \\ \psi_{\mathbf{k}}(0) = 0 & \text{otherwise,} \end{cases} \quad (80)$$

where $A = 4.608 \times 10^3$ is the amplitude of forcing and $\theta_{\mathbf{k}}$ is a random variable chosen from a uniform distribution on $[-\pi, \pi)$ at each wave number. In dimensional units, this corresponds to an initial condition in the region around $k_f \approx 1.5 \times 10^2 \text{ mm}^{-1}$. Moreover, we apply a Gaussian filter in physical space to achieve a beam profile comparable to that of the experiment.

Applicability of the WT approach is verified by the calculation of the nonlinear parameter ${}^L J$, equation (10), for the numerical simulation, which agrees with the experiment and is of the order ${}^L J \simeq 100$. Experimentally, we measure the light intensity $I(x, z) = |\psi|^2$ and not the phases of ψ . Therefore the wave action spectrum $n_{\mathbf{k}}$ is not directly accessible. Instead, we measure the intensity spectrum, $N(\mathbf{k}, z) = |I_{\mathbf{k}}(z)|^2$, where the k -scaling for $N_{\mathbf{k}}$ in the inverse cascade state is easily obtained from the KZ solution (51b) and the random phase condition, (see Appendix I). This procedure gives an intensity spectrum of

$$N_{\mathbf{k}} \propto k^{-1/5}. \quad (81)$$

The wave action spectrum from the numerical simulation is shown in figure 19 at two different distances, we observe at $z = 0 \text{ mm}$ the peak from the initial condition at high wave numbers, then at $z = 63 \text{ mm}$ we observe evidence of an inverse cascade,

as the majority of the wave action is situated towards low wave numbers. However, at low wave numbers we do not see the spectrum matching our theoretical KZ prediction (51b). We showed in Section 3.8, that the wave action flux, $Q_{\mathbf{k}}$, corresponding to the KZ solution (51b), has the incorrect sign for an inverse cascade. Therefore, we noted that the inverse cascade spectrum would correspond to a mixed thermal solution with a finite flux contribution. This is the probable cause for the lack of agreement with the KZ solution. We observe from figure 19, that $n_{\mathbf{k}} \propto k^0$ at low wave numbers, which may account for the mixed thermal solution (as this scaling corresponds to the equipartition of wave action (47b)) or for the presence of solitons (c.f. figure 17).

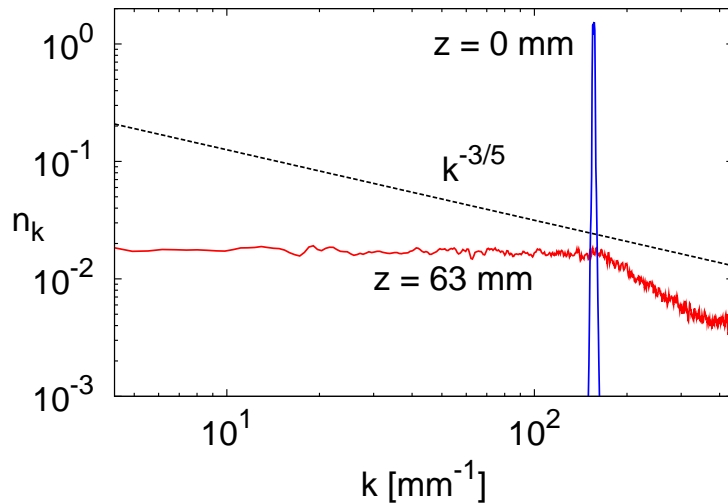


Figure 19: Numerical spectrum of the wave action, $n_{\mathbf{k}}$, at distances $z = 0 \text{ mm}$ and $z = 63 \text{ mm}$.

The numerical spectrum of the light intensity is shown in figure 20. In this plot, we observe an inverse cascade, resulting in a good agreement with the WT prediction for the intensity spectrum (81). This agreement may be coincidental, as we have shown that the flux directions are insufficient for a KZ wave action cascade. However, the intensity spectrum is a non-local quantity, and the system may, somehow, conspire to have better scaling properties of the KZ type for the intensity than for the wave action density. We can only confidently say that we still do not fully understand the agreement.

Verification of the long-wave limit $kl_{\xi} \ll 1$ and deviation from integrability is checked by considering the ratio of the two nonlinear terms in the LWE (7), which we denote as R , and is estimated in Fourier space as $R \propto k^2 l_{\xi}^2$. We observe from the experiment and the numerical simulations, respectively, figures 7 and 20, that the inverse cascade is approximately in the region $k \sim 10^4 - 10^5 \text{ m}^{-1}$, giving an estimation of $R \sim 10^{-2} - 1$. Note, that if R is too small, then we are close to an integrable system, which would be dominated by solitons and lack cascade dynamics, and if R is too high then the LWE is a poor approximation for 1D OWT.

The numerical simulation of the intensity distribution $I(x, z)$, showing the beam

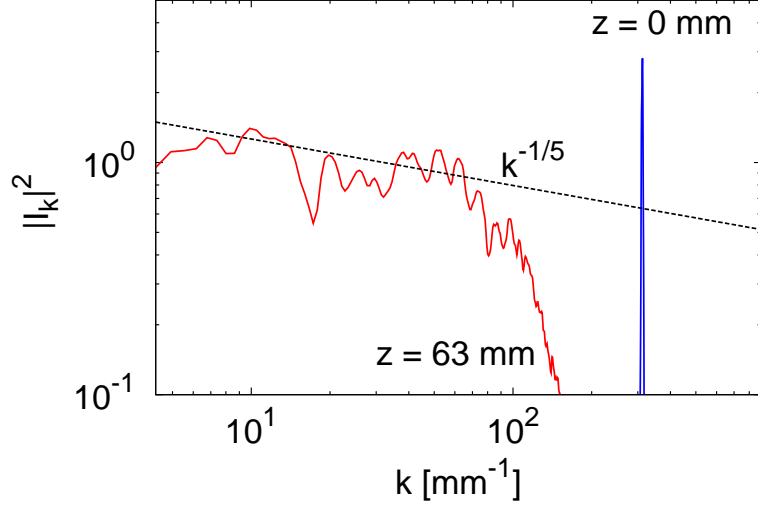


Figure 20: Numerical spectrum of the light intensity, $N_{\mathbf{k}} = |I_{\mathbf{k}}|^2$ at two different distances z . Averaging is done over a small finite time window and over ten realisations.

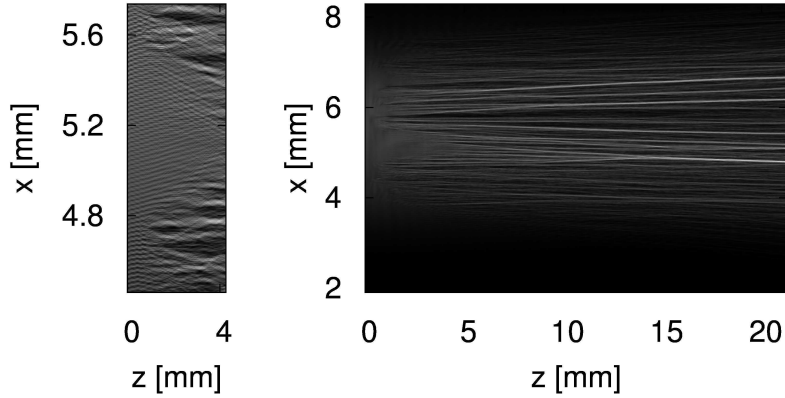


Figure 21: Numerical results for intensity distribution $I(x, z)$. The frame on the left is a magnified section of the initial propagation of the beam.

evolution during propagation is displayed in figure 21. Both the experimental and the numerical results, respectively figures 8 and 21, indicate that the total number of solitons reduces. The observed increase of the scale and formation of coherent structures represents the condensation of light. Experimentally, the condensation into one dominant soliton is well revealed by the intensity profiles $I(x)$ taken at different propagation distances, as shown in figure 9 for $z = 0.3, 4.5$ and 7.5 mm. Note that the amplitude of the final dominant soliton is three orders of magnitude larger than the amplitude of the initial periodic modulation.

4.2.2. The PDF of the light intensity

Numerically, we have computed the PDF of the light intensity and, for comparison with the experiment, we plot in figure 22 three PDFs at distances $z = 0 \text{ mm}$, $z = 31 \text{ mm}$ and $z = 63 \text{ mm}$. As in the experiment (see figure 11) we observe deviations from a pure Gaussian field, with a slower than exponential decay of the PDF tails. Again, non-Gaussianity corresponds here to *intermittency* of WT and, indeed, it accompanies the development of coherent structures (solitons) in the system.

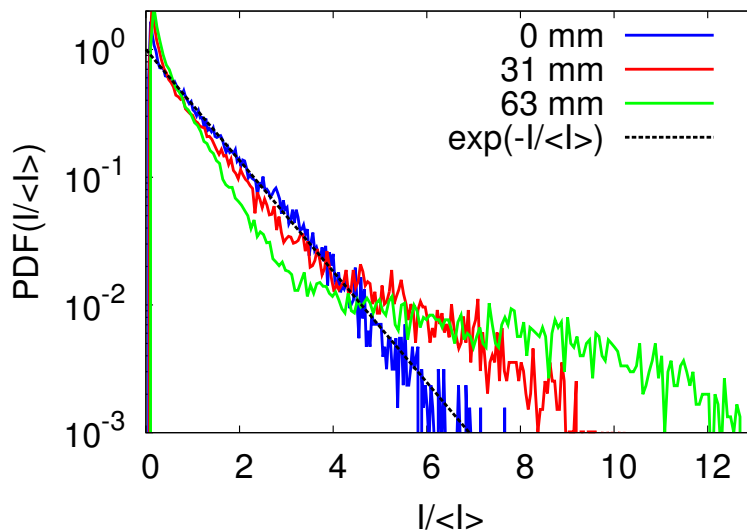


Figure 22: Normalized PDFs of the wave intensity within the numerical cell at three different distances along the cell, $z = 0 \text{ mm}$, 31 mm and $z = 63 \text{ mm}$. The black dashed straight line corresponds to the Rayleigh PDF corresponding to a Gaussian wave field.

4.2.3. The $k - \omega$ Plots: Solitons and Waves

To allow us to capture the inverse cascade dynamics in more detail and to enable us to visualize solitons and analyze their interactions with incoherent waves, we perform an additional decaying simulation with a lower initial intensity. However, to compensate for the lower intensity initial condition, we must run the simulation for much longer times. Separation of the random wave and the coherent soliton components can be achieved by performing an additional Fourier transform with respect to z over a finite z -window which results in the 2D Fourier (\mathbf{k}, ω) -plots of wave action density [47, 51].

The numerically obtained (\mathbf{k}, ω) -plot enables the direct observation of the dispersion relation of random waves, and is shown in figure 23. Here, the incoherent wave component is distributed around the wave dispersion relation, which is Bogoliubov-modified by

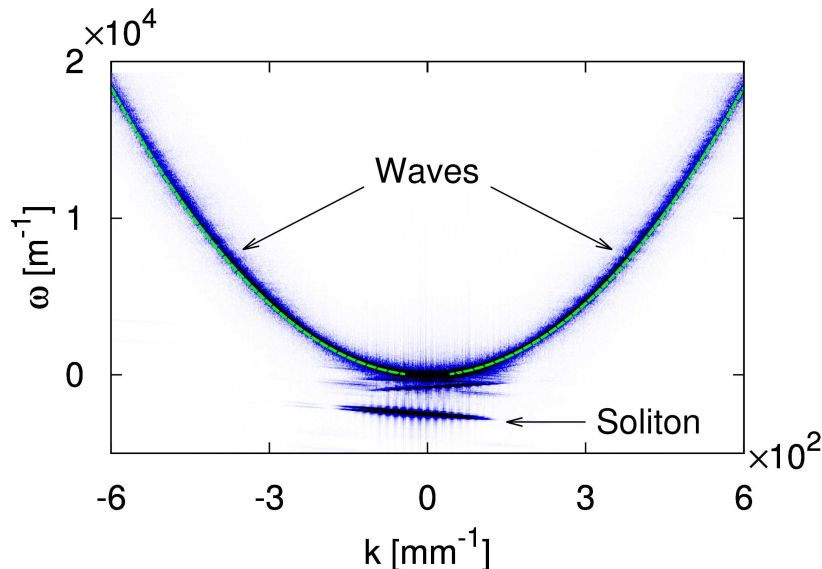


Figure 23: The (\mathbf{k}, ω) -plot of the wave field at $z = 10$ m. The Bogoliubov dispersion relation is shown by the dashed green line.

the condensate, (64), and is shown by the solid line in figure 23. The distribution of the dispersion relation is centered around the theoretical prediction (64). We observe that the width of the dispersion relation is narrow for large \mathbf{k} , a sign of weak nonlinearity, and progressively gets wider as it approaches smaller wave numbers. This broadening, is an indication that the nonlinearity of the system increases towards smaller \mathbf{k} , as was theoretically predicted in Section 3.7. At wave numbers around zero, we see that the theoretical Bogoliubov curve vanishes, corresponding to the region defined by equation (65), where the frequency becomes complex. For such wave numbers \mathbf{k} , MI of the wave packets occurs and the WT description breaks down. Below the region where the Bogoliubov relation becomes complex, we observe slanted lines. Each of these lines corresponds to a coherent soliton, whose speed is equal to the slope of the line. To examine the time evolution of the system, we have put together successive (\mathbf{k}, ω) -plots into a movie. We observe that the formation of solitons is seen in the movie as straight lines peeling with a gradient tangential to the dispersion curve. Moreover, we observe the gradual migration of these lines to higher negative frequencies, as the solitons begin to grow in size by the absorption of energy from surrounding waves or by merging with other solitons.

Further analysis can be done by separating the wave and the soliton components of the (\mathbf{k}, ω) -plot. We define the soliton region of the (\mathbf{k}, ω) -plot as the region defined with $-\omega_{\max}/2 < \omega < 0$, (where ω_k ranges from $[-\omega_{\max}, \omega_{\max})$ and $\omega_{\max} = k_{\max}^2$ in the (\mathbf{k}, ω) -plot). We chose this region to represent the soliton component because we found that some wave component of the dispersion relation appears in the extreme negative ω -region due to the periodicity of the Fourier transform and possibly from an insufficient time window for the Fourier transform in z . Consequently, the wave component is defined as the region of the (\mathbf{k}, ω) -plot outside the soliton region. By inverting the Fourier

transforms of each of the soliton and wave regions separately, we can recover the wave field $\psi(x, z)$ for each component. This enables us to compare the soliton and wave components of the intensity profile, figure 24, and the wave action spectrum, figure 25. In figure 24, we plot the intensity profile of light in real space for the soliton and wave components. We see that our procedure does indeed isolate the coherent solitons from the random wave background and we observe that the main soliton is a least an order of magnitude greater than the random wave field.

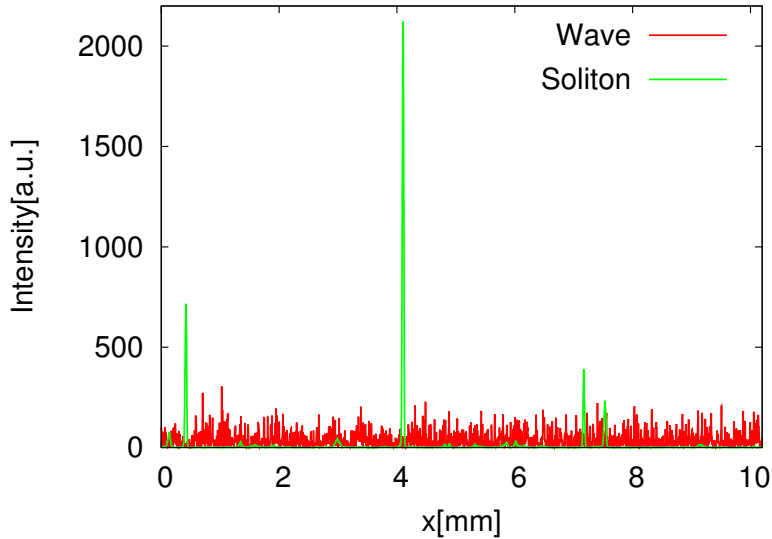


Figure 24: Plot of the intensity profile at $z = 10$ m of both the soliton and wave components

In figure 25, we observe that the soliton component of the wave action spectrum, is situated towards the low wave number region and scales as $\propto k^0$. This profile is qualitatively similar to the wave action spectrum of the exact soliton of the 1D NLSE, seen in figure 16. The wave component of the wave action spectrum is more widely distributed in \mathbf{k} -space. Taking into account that the initial spectrum was concentrated near $k = 1.5 \times 10^2 \text{mm}^{-1}$, we see that, roughly, the inverse cascade range is soliton dominated and the direct cascade range is random-wave dominated in this run. We also put a slope corresponding to the inverse cascade KZ spectrum to show that it strongly disagrees with the spectrum in the soliton dominated range. In the direct cascade range, the spectrum is consistent with the thermalized spectrum for energy (47a). For comparison, we also plot the direct cascade KZ scaling in figure 25. We see that the thermalized spectrum is in a much better agreement with the data than KZ. This is not surprising, as the decaying simulation is void of any dissipation mechanism, so energy would tend to thermalize. We would expect to see a better test of the KZ predictions in the forced and dissipated simulations where a non-equilibrium stationary state can be achieved.

Note that in other wave systems, the separation of the coherent and wave components, may be a useful technique in observing the KZ scaling otherwise masked by the presence

of coherent structures.

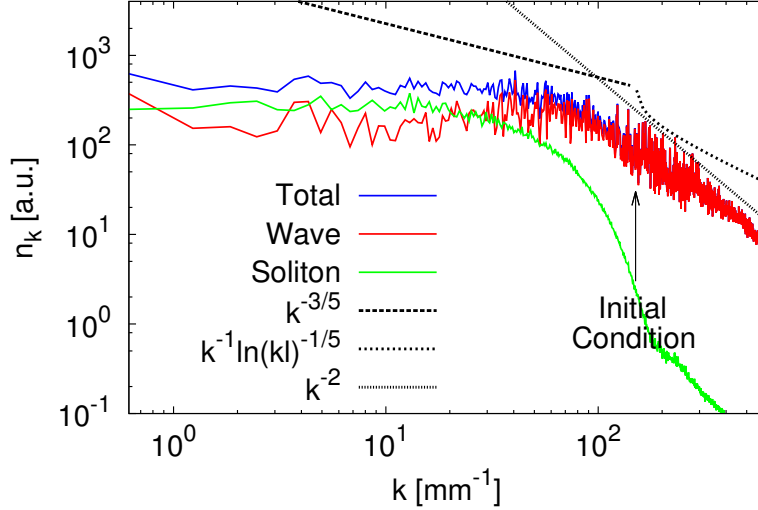


Figure 25: The wave action spectrum of both the soliton and wave components of the spectrum, with the KZ and thermalized energy predictions for comparison.

From the same simulation, we plot the (x, z) -plot for the intensity distribution, $I(x, z)$, in figure 26. With the longer propagation distance, we observe the formation and evolution of solitons from the weakly nonlinear background. In the initial stages of the simulation, we observe enlargement of the characteristic wavelength of the random waves followed by the formation of numerous solitons out of the random wave background. As the simulation progresses, the solitons become more pronounced and begin to behave independently from the waves, with an almost random movement through the numerical box. A large number of solitons are produced at the beginning of the simulation, but over long evolution times, the number of solitons reduces, with the remaining solitons being of increasing amplitude. Indeed, there are many soliton merging events. In figure 27b we see a magnified section of a merging event from figure 26. At late times, figure 26 shows a single dominant soliton in the system that has subsequently grown by absorption of energy from fellow solitons and the background wave field. Such a final single-soliton state is also observed in the experiment (figure 8), albeit at a much shorter propagation distance, with the multi-soliton range missing. In the future, it would be interesting to set-up a larger experiment which could capture the multi-soliton transient state. In figure 27, we plot three zoomed sections of figure 8 to highlight aspects of the soliton behavior. In figure 27a, we observe several solitons passing through one another with little deviation in their trajectories. Moreover, the weaker solitons (light gray in color), have almost straight trajectories, like freely propagating linear waves, whilst the stronger solitons' movements are more erratic.

In figure 27b, we magnify a merging event between two solitons. The larger soliton engulfs the smaller soliton almost without any deviation in its trajectory. Therefore, in

the numerical simulation, large solitons absorb energy from smaller solitons, reducing the total number within the system. In addition, we also observe at $z = 11.5 m$, a soliton bouncing off the larger soliton. As the weaker soliton approaches the larger soliton, it slows, before moving away at a fast speed. When two solitons merge and when they repel is a key question that still remains to be answered. Finally, in figure 27c, we observe two weak solitons propagating together, until around $z = 13 m$, when they both repel each other and disperse back into the random wave field. This shows the break up of the coherent structures and the subsequent re-injection of wave action into high frequency waves. All these events are parts of the WTLC, i.e. the cycle of coexistence and interactions of the random waves and the solitons and their mutual transformations into one another.

In figures 28 and 29, we plot the maximum of the intensity and the energy of the system with z . To begin, we note that the maximum of the intensity of the wave field is always growing, and moreover, we observe that there is a sharp increase in the maximum at around $z = 11 m$. This jump corresponds to the merging event seen in figure 27b. Thus, the dominant soliton instantly grows in size once it absorbs the other soliton. This merging event is also noticed in figure 29, where we observe a similar sharp increase to the linear and nonlinear energies at $z = 11 m$, showing that as the dominant soliton's amplitude increases, there is a significant increase in the nonlinearity of the system. It is interesting that the amplitude of the final dominant soliton continues to grow at the late stages of this simulation, e.g. in the range of z between $15 m$ and $20 m$. This soliton acts as a kind of "optical vacuum cleaner" which, as it moves, sucks in energy of the random waves and remaining soliton debris (i.e. soliton-like structures which are so weak that they cannot maintain their coherence for long).

From the beginning, the nonlinear energy, associated mostly with the first nonlinear term in the evolution equation (7), grows almost by an order of magnitude in size, compared to just under double in size for the linear contribution. This indicates that the inverse cascade and the subsequent soliton development is associated with an increase in the nonlinearity of the system, and hence the breakdown of the WT description. Moreover, we note that the total energy remains conserved, verifying that our simulation is well-resolved.

In figures 30, we present the soliton and wave components of the energies evolving with z . The data was made by using the same soliton-wave separation technique as the one we described previously, now using a series of (\mathbf{k}, ω) -plots and computing the energy values at each time. In figure 30a, we observe that over time the total energy of the wave component increases, whilst the energy of the soliton component decreases, crosses zero and becomes negative. However, this is not indicating a reduction in the soliton strength but the opposite, noting that the first nonlinear energy term in the long-wave Hamiltonian is negative, this indicates that the soliton component is becoming more nonlinear (an increase in the negative energy contribution). This fact is supported by figures 30b and 30c, where the linear and nonlinear energies of the soliton component are growing in magnitude and becoming of similar values. In figures 30c and 30d, we have labeled the point in time where two large solitons merge (see figure 27b). At this point, we observe a sharp acceleration in the growth of both the nonlinear energies, which coincides with figures 28 and 29 showing a sharp increase in the maximum intensity and energies at the same point in z . Thus figures 30 point towards a system that is becoming more nonlinear in time, with energy flowing from waves into solitons. In figure 30b we see

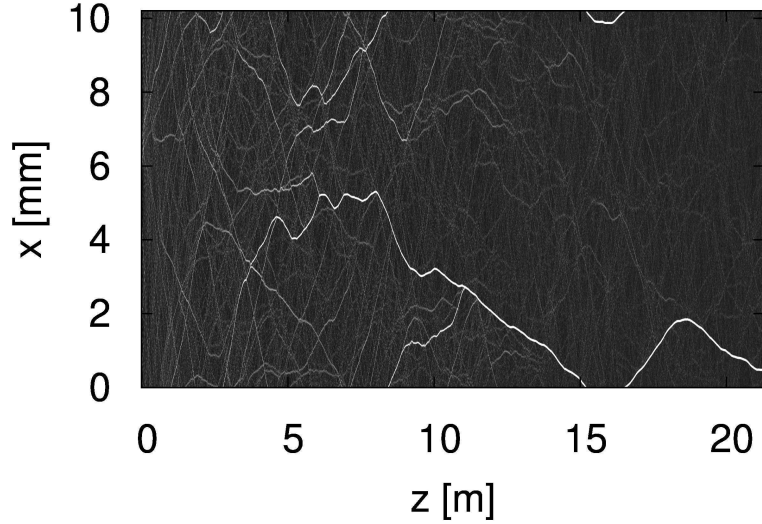


Figure 26: Numerically obtained $I(x, z)$ -plot for a long time simulation with a low intensity initial condition to see the inverse cascade and soliton merging.

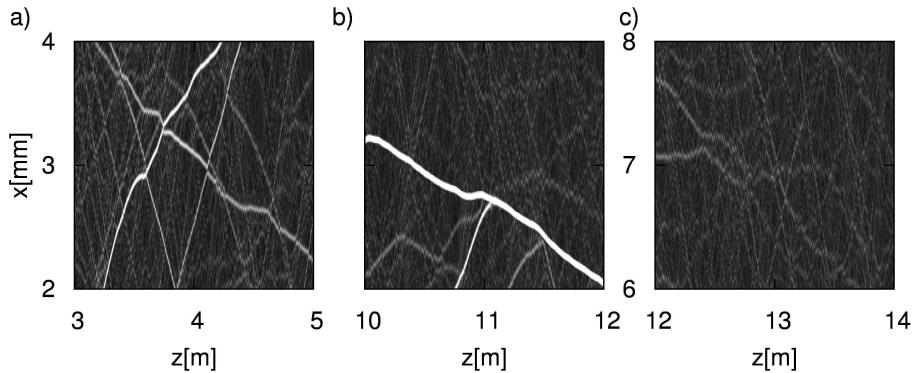


Figure 27: We present three close-up images of the (x, z) -plot of figure 26, highlighting three types of soliton behavior: a) passing through each other, b) merging and c) dissipating.

almost no growth with respect to the linear energy of the solitons. This coincides with the analysis of Subsection 3.9, where the consideration of the conserved quantities led us to expect the generation of waves rather than the increase in the momentum of the solitons. This is indeed the case, as figure 30b shows, and is further supported by figure 26. If we observe closely the paths of the solitons in figure 26, we observe that the solitons at late times are not moving ‘faster’ than those from earlier times. Moreover, what is interesting is that in figure 28, we observe an increase to the maximum intensity of the system when there is only a single soliton present ($z > 11$ m), i.e. the single soliton is still growing in size, but now by the absorption of wave action from the linear wave background and

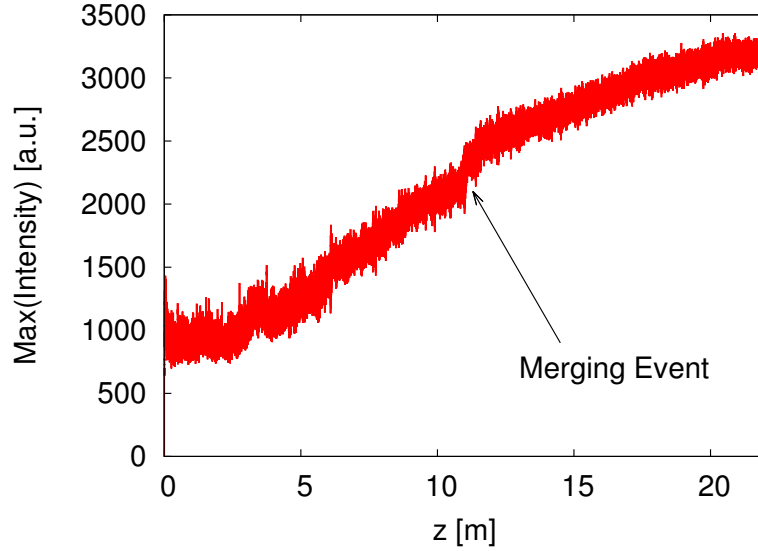


Figure 28: Plot of the maximum of the wave intensity in physical space versus z .

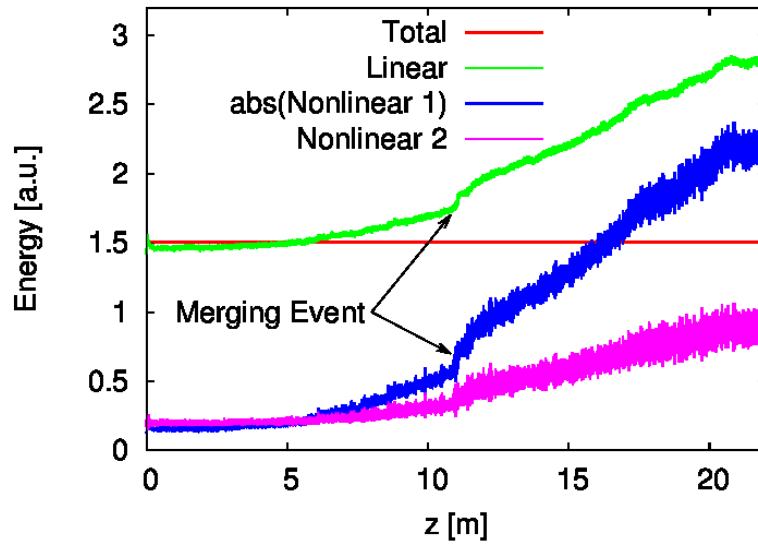


Figure 29: Plot of the energies for the long time simulation. We see the conservation of the total energy, the growth of the linear and both nonlinear energies (corresponding to the two nonlinear terms in equation (13a)).

not by merging with other solitons. This can be viewed as a vacuum cleaner effect, with the soliton ‘hoovering’ up wave action from waves. However, we note that this process does not remove waves from the system, as clearly in figure 30b we observe the

wave component of the linear energy is still increasing. Note that the growth of the wave energy is consistent with the loss of their wave action when the mean wavelength is decreasing. It seems that the hoovering effect is more efficient when the soliton is large in size, as opposed to earlier times when solitons are small in amplitude. The evidence for this scenario is observed in figures 28 and 30, where, at early times, sharp soliton growth (and subsequently the increase of the linear and nonlinear energies) is more determined and dominated by discrete mergers between solitons (as seen by the sudden spike in growth during the large merger event). However, at late times, when no more merging events occur, we still observe a growth in the maximum intensity, linear and nonlinear energies but in a more smooth and continuous fashion. At asymptotically large times, we expect that the equilibrium state will consist of a single stationary soliton, containing the majority of the wave action in the system, and a sea of small amplitude short random waves, containing the majority of the linear energy of the system. This scenario was originally predicted in [80, 135] and shown using statistical mechanics arguments in [85, 87].

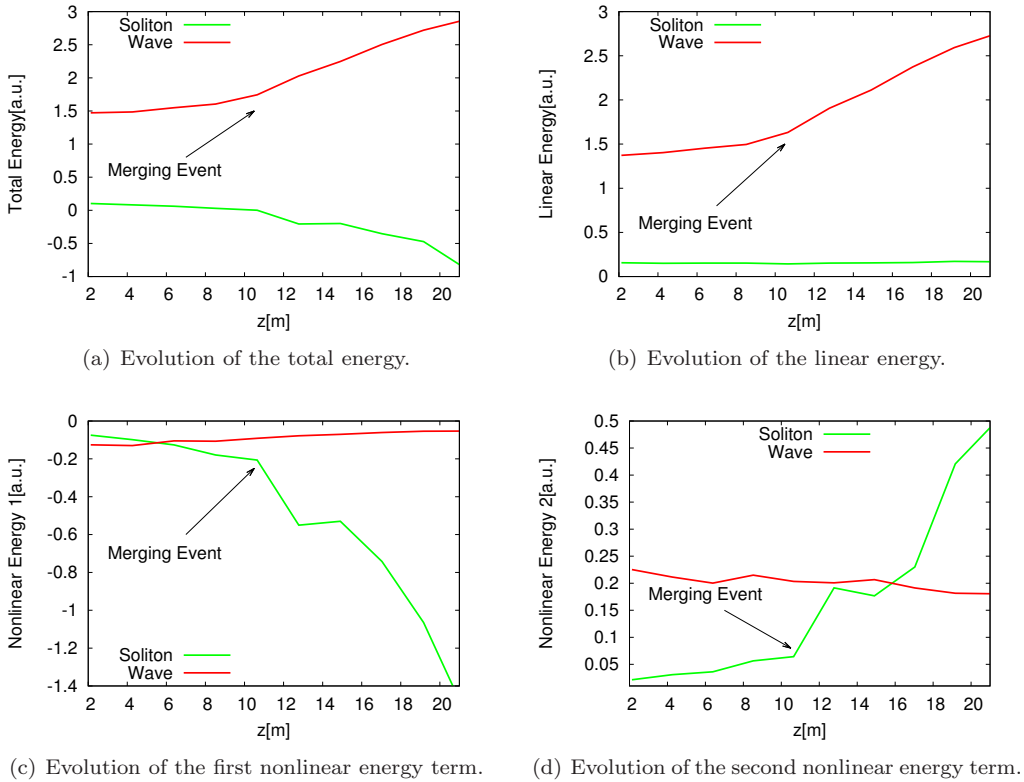


Figure 30: Plot of the evolution of the (a) total energy, (b) linear energy, (c) first nonlinear energy term, and (d) second nonlinear energy term, of the soliton and wave components versus z .

In figure 31, we plot the intensity PDF in \mathbf{k} -space for two wave numbers, $k = 9.8 \text{ mm}^{-1}$, and $k = 2.9 \times 10^2 \text{ mm}^{-1}$ at $z \approx 20 \text{ m}$. The two wave numbers are situated in

the low wave number (soliton dominated) and high wave number (weak wave dominated) regions respectively. We observe at both large and small values of $J_{\mathbf{k}}$ both PDFs show signs of depletion of their probability with respect to the Rayleigh distribution. However, there is far more depletion observed in the soliton dominated PDF at $k = 9.8 \text{ mm}^{-1}$. Probability depletion in the wave dominated scale, $k = 2.9 \times 10^2$, at the large (small) $J_{\mathbf{k}}$ corresponds to a positive (negative) probability flux $\mathcal{F}_{\mathbf{k}}$. We believe that the depletion at both large and small $J_{\mathbf{k}}$'s is because of the hoovering effect of the soliton - as solitons grow, their hoovering effect (absorption of wave action from waves) becomes more apparent and thus more depletion is seen. As the soliton is composed of a wide range of wave modes, this effect will occur at a large range of wave numbers (even high wave numbers). However, as the solitons merge, grow, or dissipate, they excite high frequency waves. This behavior would encourage the transportation of wave action from the soliton to small $J_{\mathbf{k}}$ s. Indeed, this process would generally only occur at high wave numbers and technically would produce an enhancement (negative probability flux) of the PDF tail in figure 31. The balance between the hoovering effect and excitation of waves is probably what is occurring at high wave numbers, giving rise to an almost (slightly depleted) Rayleigh PDF at $k = 2.9 \times 10^2 \text{ mm}^{-1}$. Over time, as solitons merge and dissipate, until only one remain, we would observe a reduction in the re-injection of wave action at high wave numbers because the mechanisms that allow this (merging and dissipation of solitons) would cease. At low wave numbers, at $k = 9.8 \text{ mm}^{-1}$, the PDF would gradually become more and more depleted (deviated from Rayleigh) as time progresses. As this scale is soliton dominated, we cannot apply our theory of the PDF depletion in terms of the probability flux $\mathcal{F}_{\mathbf{k}}$ which was developed for weak waves. In fact, such a PDF corresponds to a certain distribution of solitons in the soliton parameter space (A, B) for which a theory has not yet been developed.

The observed directions of the probability flux directions $\mathcal{F}_{\mathbf{k}}$ - toward large $J_{\mathbf{k}}$ s at low wave numbers and to low $J_{\mathbf{k}}$ s at high wave numbers - can be combined with the picture of the inverse cascade energy flux in the direction of low wave numbers by considering a 2D flux pattern on the $(k, J_{\mathbf{k}})$ -plane. This yields a diagram for the WTLC presented in figure 32. Here, the initial condition is at high wave numbers and low $J_{\mathbf{k}}$ s (weak small-scale random waves). The inverse cascade transports wave action, via six-wave mixing, to small wave numbers and to higher $J_{\mathbf{k}}$ s, as the inverse cascade is associated with an increase in nonlinearity of the system. As wave action accumulates at large scales, MI kicks in and solitons form, with wave action spreading along the soliton spectrum $n_{\mathbf{k}} \propto k^0$. Note that the wave modes within the soliton are coherent, i.e. correlated with each other. The non-integrability of the system allows for solitons to interact with surrounding structures, that enable energy exchange. In particular, solitons will collide, occasionally merge or deteriorate via random interactions - each of these processes allowing for the emission of energy and wave action to incoherent waves, resulting in a reversal of the probability flux \mathcal{F} at high wave numbers. The wave action re-injected back into the random wave component fuels the continual process of the inverse cascade. This continuous transport of wave action can be seen as a vortex-like flux structure in the $(k, J_{\mathbf{k}})$ -plane which we call the WTLC in our 1D OWT system [11, 56]. Note that from figure 31 we see a positive probability flux even at high wave numbers! Thus, the WTLC picture with flux lines not emerging and not terminating anywhere, as in figure 32, is only valid for a steady state, whereas figure 31 corresponds to an evolving transient where the net flux (produced by the hoovering effect) is still directed from waves to (growing)

solitons. For the LWE, the asymptotical final state is a single soliton containing most of wave action and surrounded by almost linear waves containing finite energy but almost no wave action.

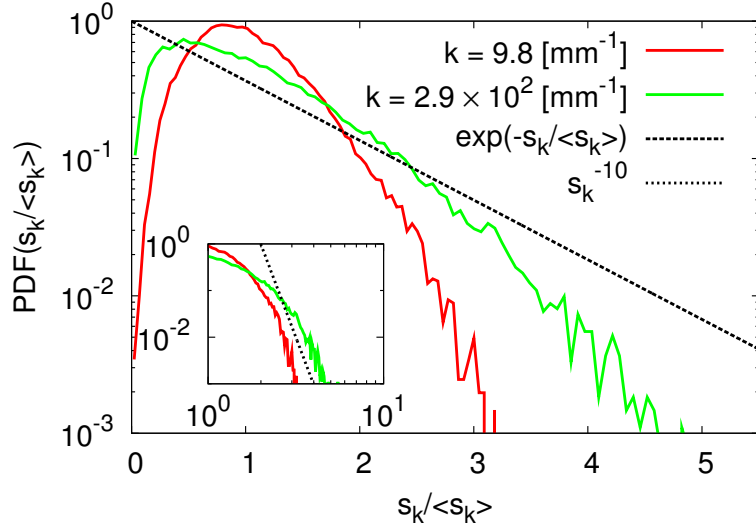


Figure 31: PDF of intensity $J_{\mathbf{k}}$, $\mathcal{P} = \langle \delta(s_{\mathbf{k}} - J_{\mathbf{k}}) \rangle$, at two wave numbers, $k = 9.8 \text{ mm}^{-1}$, and $k = 2.9 \times 10^2 \text{ mm}^{-1}$. The black dashed line is the Rayleigh distribution that corresponds to a Gaussian wave field. The inset shows the power-law behavior of the PDF tails. The black dashed line in the inset is $s_{\mathbf{k}}^{-10}$.

4.2.4. Forced and Dissipated Simulations

In this Subsection, we explore numerical simulations of the LWE and SWE with forcing and dissipation. This setup is intended to produce more idealized conditions for non-equilibrium stationary states assumed for the realizability of pure the KZ solutions, (51). Thus, we can test to see if the KZ spectra are realizable in principle, or if they can not be established at all, even in the most idealized of settings. In an infinite sized system, both the direct- and the inverse-cascade ranges can be realized in the same simulation, with forcing acting at an intermediate scale and two inertial ranges either side (see figure 14). However, computational restrictions make it impractical to perform such a simulation. Therefore, we simulate each cascade separately, by performing a simulation for each with forcing at either ends of \mathbf{k} -space, allowing for just one inertial range. We numerically solve the non-dimensionalized equation (see Appendix H) with $\alpha = 1024$. We run the simulations with a time step of $\Delta t = 1 \times 10^{-4}$ in a box of length $L = 32\pi$, with spatial resolution of $N = 2^{12}$. The simulations are run so that a non-equilibrium steady state is achieved. This is checked by observing stationarity of the total energy \mathcal{H} and wave action \mathcal{N} in the system.

For the direct cascade setup for the LWE, we introduce dissipation profiles at the two limits of \mathbf{k} -space that removing energy and wave action that is being constantly injected by the forcing. We set the low wave number dissipation profile, $D_{\mathbf{k}}^L$, to be friction, defined

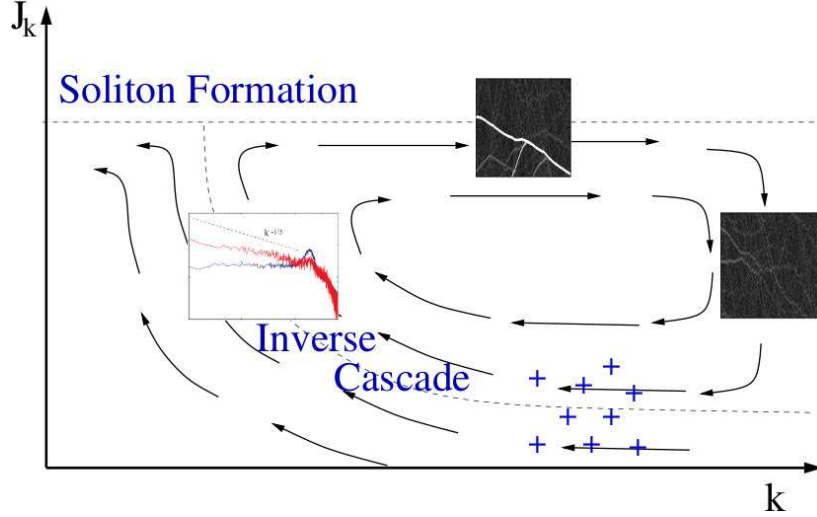


Figure 32: Diagram of the WTLC. The high wave number initial condition subsequently gets transferred to low k and high $J_{\mathbf{k}}$ by the inverse cascade. At low k , the weak WT fails (near the T -junction of the dashed lines) and MI occurs, solitons form resulting in the wave action getting spread along a $n_{\mathbf{k}} \propto k^0$ spectrum (horizontal dashed line). The emission of waves from merging or deteriorating solitons re-jets wave action at low intensities.

by (78b), with the friction coefficient of $\nu_{\text{friction}} = 5 \times 10^{-1}$ and apply a hyper-viscosity dissipation scheme at high wave numbers with a coefficient of $\nu_{\text{hyper}} = 1 \times 10^{-13}$. Forcing is situated at large scales and is defined by (76), with amplitude $A = 4.1 \times 10^4$. Once the simulation has reached a statistically non-equilibrium statistical steady state, we analyze the statistics by performing time averages over this steady state regime. We have plotted the wave action spectrum $n_{\mathbf{k}}$ for the direct cascade regime in figure 33.

We observe that the wave action spectrum in figure 33 does not agree with the theoretical KZ prediction (55). There is a clear flat spectrum of the form $n_{\mathbf{k}} \propto k^0$. This could correspond to several phenomena: solitons, critical balance and a thermalized state with equipartition of wave action. However, in figure 34, we have plotted the (\mathbf{k}, ω) -plot for the same simulation at late times. We observe an absence of any soliton structures, like the ones we saw in the decaying case (see figure 23). Therefore, we can safely reason that the flat spectrum is not associated with the presence of solitons within the system. The explanation for the k^0 slope is more likely down to the thermalization of the system with respect to wave action around the low to the intermediate wave number range. This behavior should be expected due to the lack of agreeing flux signs with Fjørtoft's argument for the LWE, where a system in such a situation would tend towards a modified thermalization spectrum [50] also known as a “warm cascade” [49]. The lack of agreement with the KZ spectrum can be explained by the incorrect flux directions which can be most easily understood and determined using the DAM in Subsection 3.8. It remains to be understood why we observe that the wave action spectrum corresponds more closely with the thermalized KE solution corresponding to the equipartition of wave action, and not the thermalized spectrum corresponding to the equipartition of energy. On the other hand, we observe that the (\mathbf{k}, ω) -distribution is not too narrow around the dispersion

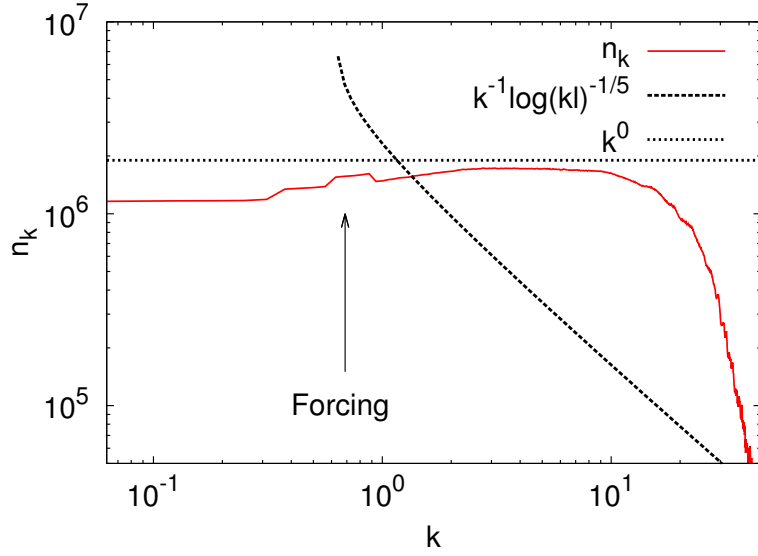


Figure 33: The wave action spectrum $n_{\mathbf{k}}$ in a statistically non-equilibrium stationary state for the direct cascade simulation of the LWE. We plot two black lines to show the theoretical comparisons. The black dashed line represent the WT prediction of the KZ solution $n_{\mathbf{k}} \propto k^{-1} \ln(k\ell)$. The black dotted line represents the thermalization of wave action.

curve $\omega = \omega_k = k^2$. Thus, we cannot rule out that the CB mechanism could be the real reason for the flat spectrum.

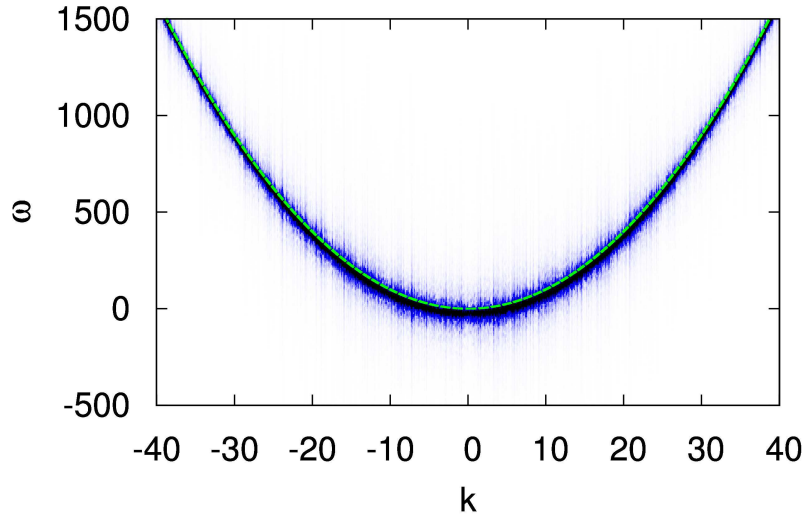


Figure 34: (\mathbf{k}, ω) -plot for the direct cascade simulation of the LWE. The green line represents the linear wave frequency $\omega_k = k^2$.

In figures 35 we plot PDFs of (a) the wave intensity in the physical space and (b) the Fourier-mode intensity at two different wave numbers. In figure 35a, we observe an almost perfect agreement of the the PDF to the Rayleigh distribution. This indicates that the system corresponds to a Gaussian wave field - a good indication that the system is in a thermalized state of random waves. Additionally in figure 35b we observe that both PDFs are Rayleigh distributed (here the Rayleigh distribution is fitted to the tails of the PDFs). Again, we observe a clear agreement of the tails to the straight line of the Rayleigh distribution at large amplitudes. Towards the core of the PDFs in figure 35b we see some depletion of the PDFs to the Rayleigh distribution the origin of which remains unclear. It is possible that this is a signature of appearance of an embryonic condensate (the true condensate, solitons, are not present in this system due to low wave number dissipation) - a similar effect was observed in recent simulations of the 3D NLSE [49].

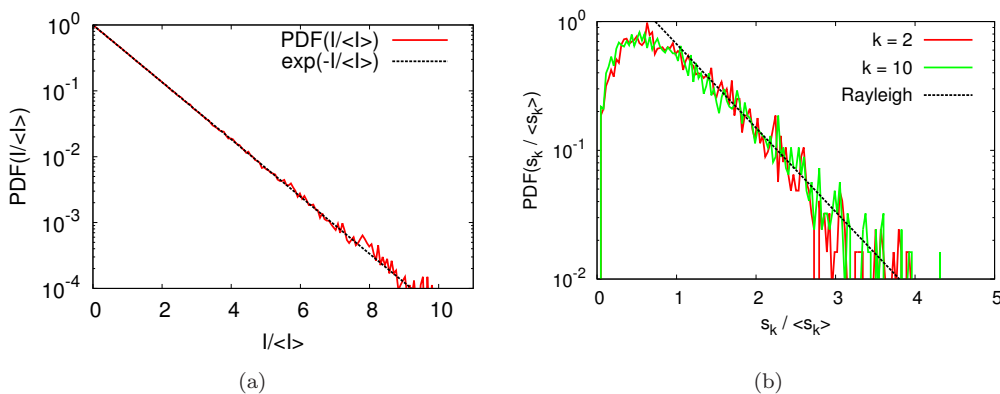


Figure 35: (a) Normalized PDF of the wave intensity in the direct cascade simulation of the LWE. The straight line corresponds to the Rayleigh distribution. (b) Normalized PDF of $J_{\mathbf{k}}$ at two wave numbers for the direct cascade in the LWE. The black dashed line represents the Rayleigh distribution.

The inverse cascade displays more unusual behavior. The inverse cascade simulation for the LWE was setup with forcing situated at high wave numbers with a profile given by equation (77) and with low wave number dissipation in terms of friction and high wave number dissipation in terms of hyper-viscosity. The parameters used for the simulation are $A = 7.7 \times 10^3$ for the forcing amplitude, $\nu_{\text{friction}} = 1 \times 10^{-1}$ and $\nu_{\text{hyper}} = 1 \times 10^{-11}$ for the dissipation coefficients. As usual, we wait for a non-equilibrium stationary state to be achieved before performing any analysis.

In figure 36 we plot the wave action spectrum from the numerical simulation, time averaged once the simulation has reached a non-equilibrium stationary state. For comparison, we also show the KZ prediction for the inverse cascade of wave action. We observe a lack of agreement to any power-law behavior to the spectrum. Indeed, we see a peak of the spectrum around the forcing region, while the spectrum gradually fall off at small and large k . The absence of a KZ spectrum can be explained by the incorrect flux directions, but what is really surprising is the omission of any thermalized or CB spectrum. The CB in this case, is identical to the spectrum of the spectrum of the thermalization of wave action: $n_{\mathbf{k}} \propto k^0$. CB has been observed in other optical systems, i.e. one described by the 3D NLSE [49]. We found that the spectrum to the

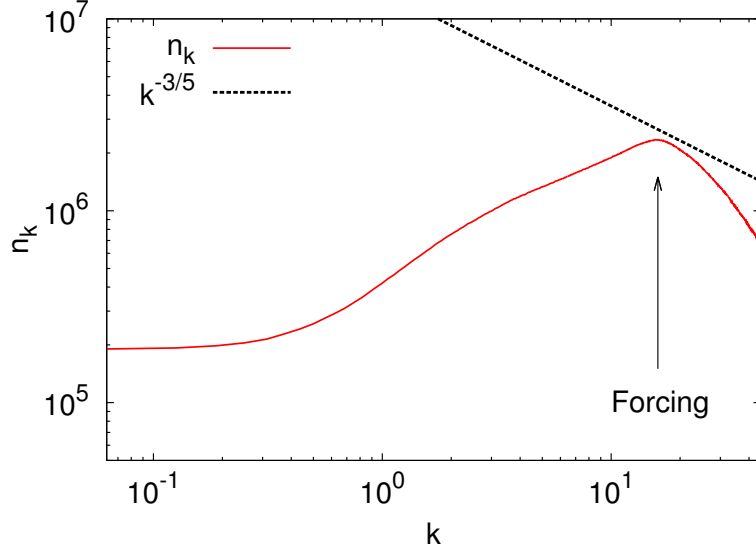


Figure 36: The wave action spectrum, $n_{\mathbf{k}}$, in a statistically non-equilibrium stationary state for the inverse cascade simulation of the LWE. The straight line represents the WT prediction of the KZ solution of $n_{\mathbf{k}} \propto k^{-3/5}$.

left of the forcing region seemed to be determined by the level of friction used at low wave numbers. By tuning the coefficient of friction, we adjusted the asymptotic value of the spectrum at $k = 0$, and the spectrum would simply gradually decline to that level from the forcing region. Dampening of these low wave number modes could prevent some non-local behavior that is driving the inverse cascade. Clearly, the dampening of these modes is restricting MI and the formation of solitons, which may have an essential role in the dynamics of the inverse cascade - as we do not observe this behavior in the decaying simulation of the previous Subsection. To be certain that we are not observing any effects that might be attributed to the presence of solitons, we show the (\mathbf{k}, ω) -plot for the simulation in figure 37. In figure 37 we observe that no solitons are present by the lack of any coherent straight lines around dispersion curve. However, if one looks closely, we do observe the partial formation of a soliton situated on the dispersion curve at $k = 15$. However, with the presence of dissipation this soliton does not ‘peel’ from the wave component. Moreover, inspection of the intensity distribution (not shown), does not provide any indication of coherent soliton like structures distinguishable from random waves. The (\mathbf{k}, ω) -plot is also in good agreement to the linear dispersion relation $\omega_k = k^2$ shown by the green dashed curve, but the width of the plot is as wide as ω_k in the inverse cascade range. This implies that the system is indeed in a strongly nonlinear regime which could point at CB but, as we have already mentioned, the CB spectrum is not observed. We have also done simulations with weaker forcing amplitudes for which WT was weak, and the result was similar to the one reported here. In fact, the reason that we increased the forcing was an attempt to strengthen the wave interactions in order to “push” the inverse cascade through to the large scales.

In figures 38 we plot PDFs of (a) the wave intensity in the physical space and (b) of the

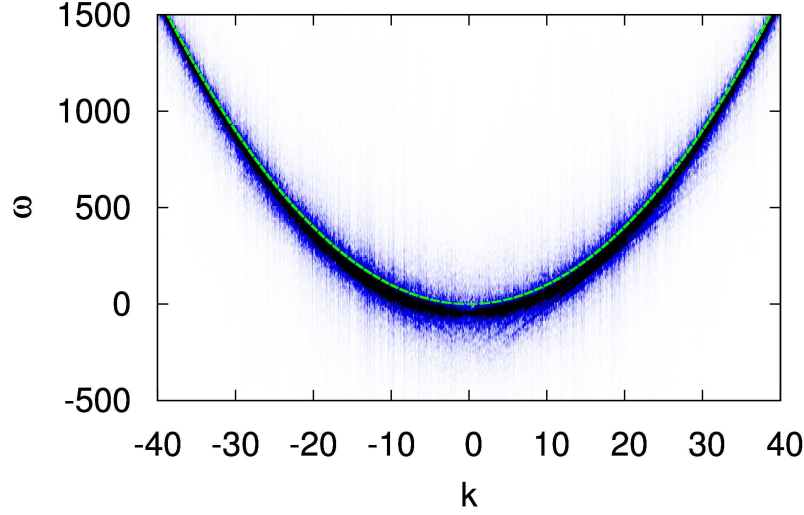


Figure 37: (\mathbf{k}, ω) -plot for the inverse cascade simulation of the LWE. The green line represents the linear wave frequency $\omega_k = k^2$.

Fourier-mode intensity at two different wave numbers. Similarly to the direct cascade, we observe agreement to the Rayleigh distribution of a Gaussian wave field. The PDF of the wave intensity in figure 38a is in perfect agreement to the unfitted Rayleigh distribution, whilst we observe good Rayleigh agreement of the tails of the PDFs in figure 38b at two wave number either end of the inertial range. Moreover, we observe a depletion of the probability at low wave mode intensities at both $k = 2$ and $k = 10$, the same phenomenon as seen in the direct cascade.

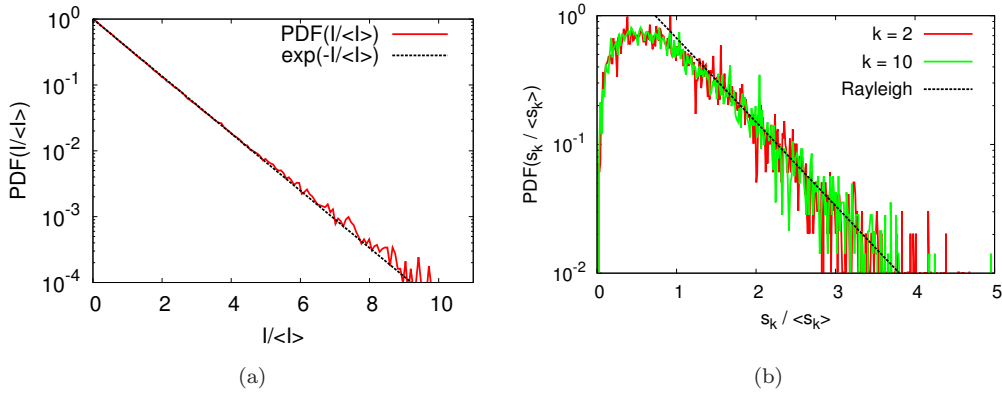


Figure 38: (a) Normalized PDF of the wave intensity in the inverse cascade simulation of the LWE. The straight line corresponds to the Rayleigh distribution. (b) Normalized PDF of $J_{\mathbf{k}}$ at two wave numbers for the inverse cascade in the LWE. The black dashed line represents the fitted Rayleigh distribution.

In the simulation of the forced-dissipated inverse cascade, we see no agreement of

the KZ, thermal or CB spectra. Moreover, we observe that the spectrum seems to be determined by the value of the lowest mode. This suggests that the inverse cascade may be associated to some non-local effect established by MI. Indeed, we find the forced-dissipated simulation to provide more questions than answers to the behavior of 1D OWT, and clearly more work in this area is needed to fully explain these results.

4.3. The Short-Wave Equation

We investigate the SWE, (9) by numerical simulations of the non-dimensionalized model of Appendix H. We apply the same forcing and dissipation profiles that are described in Section 4.1. We dissipate at low wave numbers using a hypo-viscosity profile, while using hyper-viscosity at high wave numbers.

We begin by discussing the direct cascade simulation. We force the system with the profile (76), with amplitude $A = 1.6 \times 10^2$ and use the dissipation rates of $\nu_{\text{hypo}} = 1 \times 10^{-2}$, $\nu_{\text{hyper}} = 1 \times 10^{-11}$ for the direct simulation.

In figure 39 we plot the wave action spectrum for the direct cascade averaged over a time window once the system has reached a statistically non-equilibrium steady state. We observe a good agreement to the WT prediction (52a). However, notice that there is some slight deviation of the spectrum in the middle of the inertial range. This is likely to be caused by an insufficient time average of the statistics. The agreement is surprising, as we showed that the KZ solution, (52a), does not produce convergence of the collision integral in the UV limit. However, we may be observing a non-local spectrum that is close to the local WT prediction.

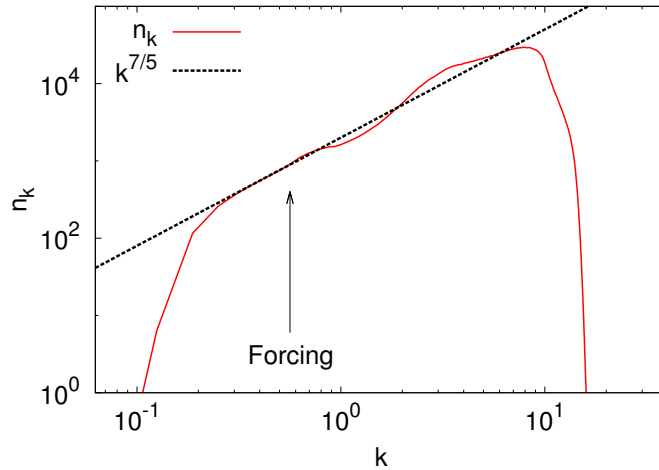


Figure 39: The wave action spectrum $n_{\mathbf{k}}$ in a statistically non-equilibrium stationary state for the direct cascade simulation of the SWE. The straight line represents the WT prediction of the KZ solution of $n_{\mathbf{k}} \propto k^{7/5}$.

In figures 40 we plot the normalized PDF for the wave intensity in physical space and in Fourier space respectively. We observe in figure 40a that there is a slight deviation to the Rayleigh distribution (corresponding to a Gaussian wave field) at high intensities. This implies that there is a larger than expected occurrence of high intensity structures

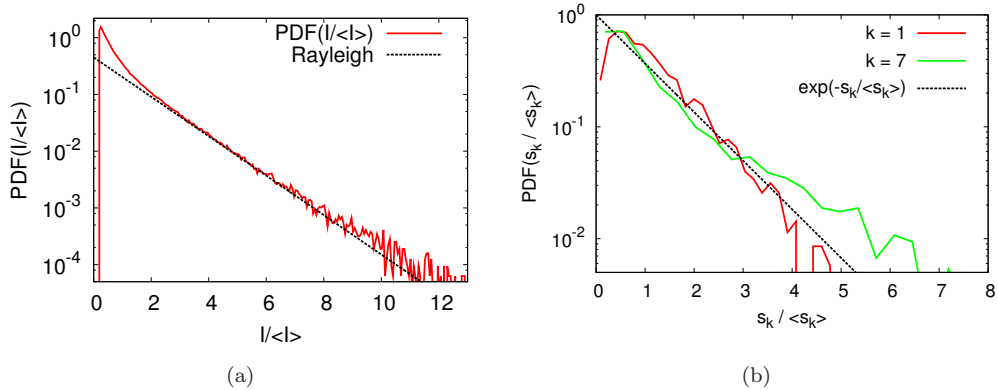


Figure 40: (a) Normalized PDF of the wave intensity in the direct cascade simulation of the SWE. The straight line corresponds to the fitted Rayleigh distribution. (b) Normalized PDF of $J_{\mathbf{k}}$ at two wave numbers for the direct cascade in the SWE. The black dashed line represents the Rayleigh distribution.

- a sign of wave intermittency. The SWE does not seem to produce solitons, but we can numerically check this fact by investigating the (\mathbf{k}, ω) -plot in figure 41. WT theory implies that such behavior should exist as part of a wave breaking process. In addition, in figure 40a we see a large accumulation of the probability at low intensities, far more than what is predicted by the Rayleigh distribution indicating an enhanced presence of dark regions void of light. On the other hand, figure 40b is the PDF of $J_{\mathbf{k}}$ at two wave numbers at either end of the inertial range. We see that the PDF at $k = 1$ remains relatively close to the Rayleigh distribution, with only a minor depletion in the tail. At $k = 7$ we observe a large enhancement of the PDF at large $J_{\mathbf{k}}$, corresponding to a negative probability flux $\mathcal{F}_{\mathbf{k}}$. Therefore, we see behavior that is similar to that which is described by the WTLC, figure 32. Observation of the (\mathbf{k}, ω) -plot, figure 41, shows that actually there are no coherent structures present in the system. This conclusion is made by the lack of structures at negative ω . Moreover, we see a clear accumulation of the dispersion curve situated around the linear wave frequency $\omega_k = k^2$. This indicates that the system is in the weak nonlinear limit.

The inverse cascade simulation of the SWE is produced with the following parameters: The forcing amplitude is set to be $A = 4.8 \times 10^2$, while the dissipation rates are given by $\nu_{\text{hypo}} = 1 \times 10^0$, $\nu_{\text{hyper}} = 1 \times 10^{-8}$. Similarly to the direct simulation, we wait until a non-equilibrium stationary state is achieved, and then perform averages on the statistics.

In figure 42, we observe a good agreement, for almost a decade in \mathbf{k} -space, with the KZ scaling (52b). At low wave numbers, we observe a slight accumulation of wave action before the dissipation occurs. However, analysis of the locality, showed us that the inverse KZ solution is invalid - similar puzzling behavior as in the case of the direct cascade simulation of the SWE.

In figures 43 we plot the normalized PDF for the wave intensity in the physical space and for the Fourier-space intensities $J_{\mathbf{k}}$. In both plots for comparison we insert lines corresponding to a Gaussian wave field. We observe in figure 43a that there is a clear deviation at low intensities from Gaussianity. This gives a clear indication of WT in-

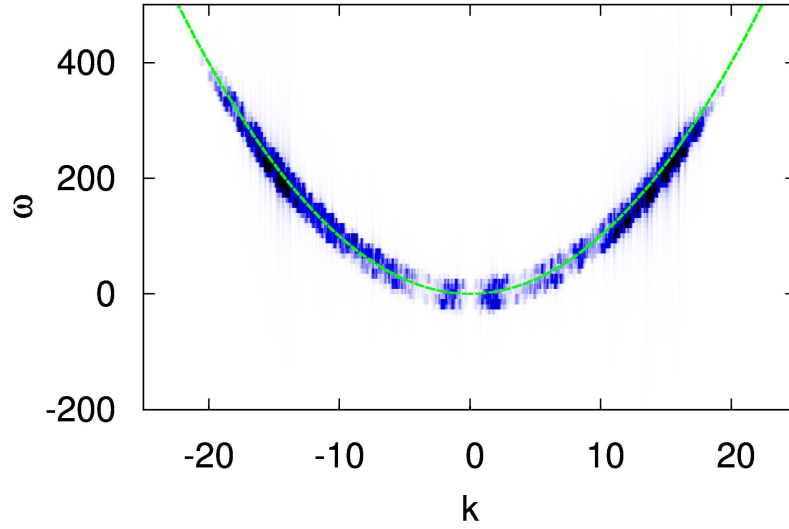


Figure 41: (\mathbf{k}, ω) -plot for the direct cascade simulation of the SWE. The dashed green line represents the linear wave frequency $\omega_k = k^2$.

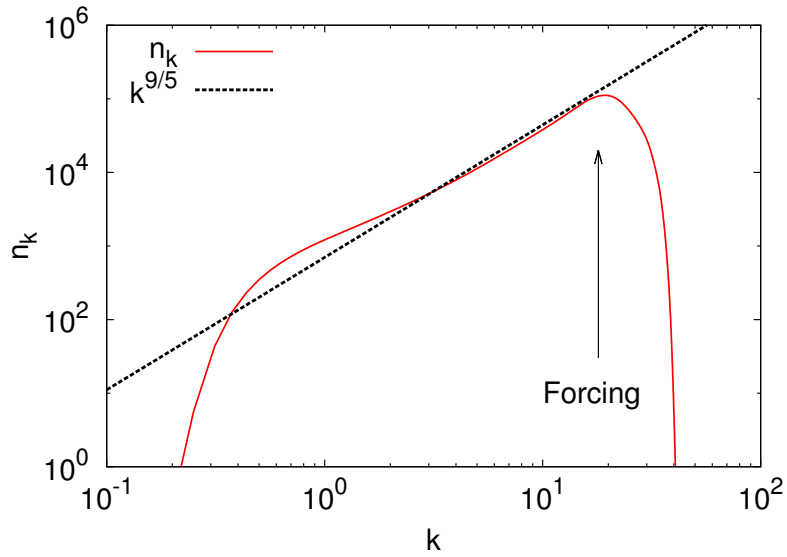


Figure 42: The wave action spectrum $n_{\mathbf{k}}$ in a statistically non-equilibrium stationary state for the inverse cascade simulation for the SWE. The straight line represents the WT prediction of the KZ solution of $n_{\mathbf{k}} \propto k^{-9/5}$.

termittency, with the enhanced frequency of occurrence of dark spots - far greater than what is predicted by a general Gaussian wave field. For $J_{\mathbf{k}}$ seen in figure 43, we see a

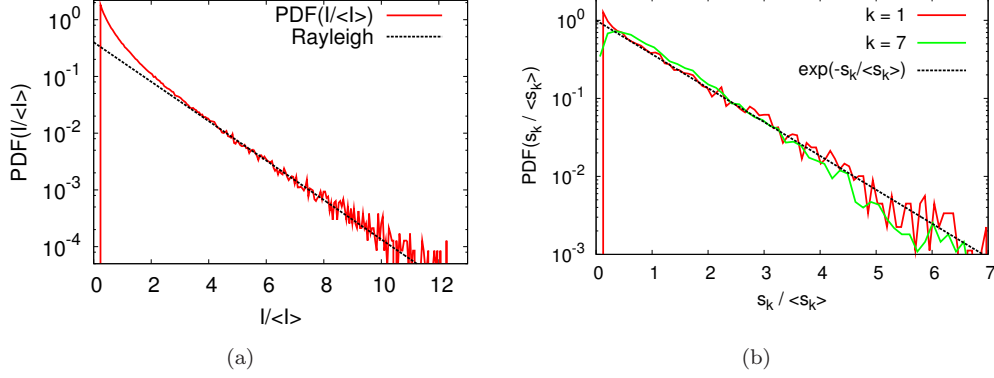


Figure 43: (a) Normalized PDF of the wave intensity in the inverse cascade simulation of the SWE. The straight line corresponds to a fitted Rayleigh distribution. (b) Normalized PDF of $J_{\mathbf{k}}$ at two wave numbers for the inverse cascade in the SWE. The black dashed line represents the Rayleigh distribution.

close agreement at intermediate $J_{\mathbf{k}}$ with the Rayleigh distribution given by the black dashed line, but at large $J_{\mathbf{k}}$ we see some slight deviation. This is a possible sign of WT intermittency, with the depletion of the PDF tail from Gaussianity. Inspection of the (\mathbf{k}, ω) -plots in figure 44 shows a wide spreading of the wave distribution around the linear dispersion curve $\omega_k = k^2$ indicating a nonlinearity level that is quite strong. Moreover, we observe asymmetric behavior of the wave distribution that clearly shifts from negative to positive wave numbers in figures 44b and 44d. This could indicate that there is some symmetry breaking instability associated with the SWE. Furthermore, there is an interesting ‘hair’-like structure around the dispersion curve in figures 44 which align together in a certain direction. It consists of lines in the (\mathbf{k}, ω) -plot indicating a set of coherent structures propagating with speeds that are determined by their slopes. The ‘hair’-like lines are not straight which indicates that the speed of such ‘solitons’ vary with time. Also note that these structures never ‘peel off’ from the wave dispersion curve like it was the case in LWE and, therefore, they never de-couple from the wave component. In figure 45a we plot the distribution of intensity at late times of the simulation over the whole domain. We observe strange behavior, in which soliton like structures are seen bundled together and weakly interacting, while propagating as a bundle with constant speed. These structures are clearly the hair-like objects seen in the (\mathbf{k}, ω) -plots of figures 44. If we take a closer inspection of the coherent structures in figure 45, we see that they meander around the center of the bundle, but remain confined to the bundle. We don’t yet know how to explain this behavior theoretically or how it is related to the KZ spectrum. In figure 45b we show a time slice of the intensity I . We see a low wave number coherent structure with high frequency peaks propagating upon it.

5. Conclusions

We introduced the field of 1D OWT, where waves of light propagating through a nonlinear medium weakly interact. We presented the first ever experiment of OWT,

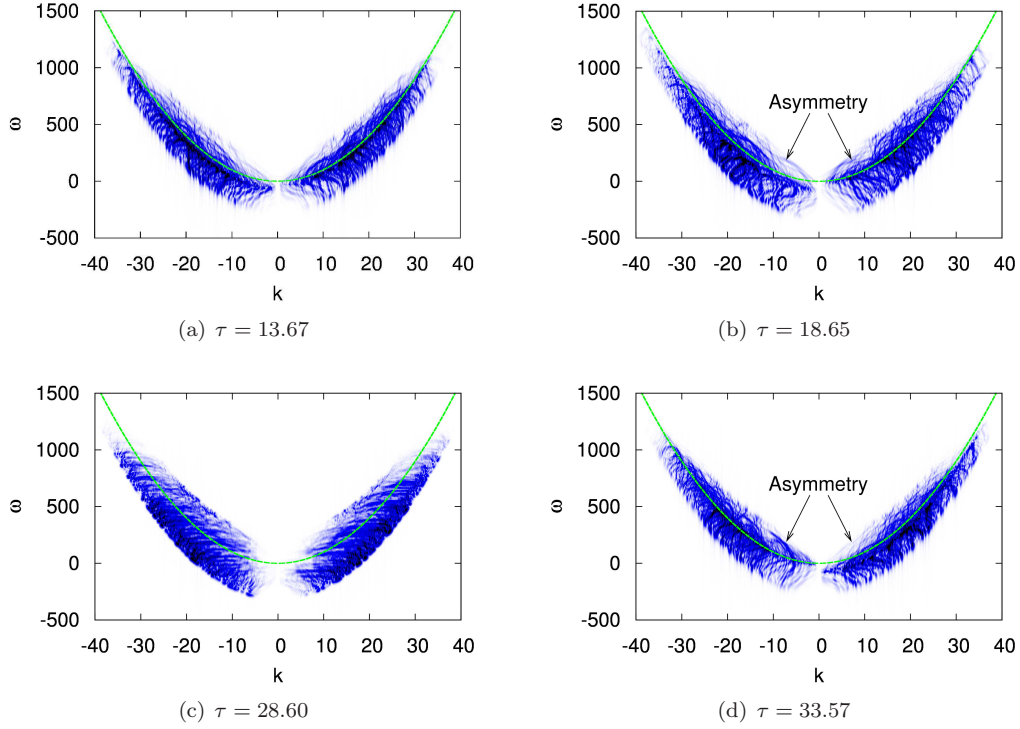


Figure 44: (k, ω) -plots for the inverse cascade simulation of the SWE at four different times $\tau = 13.67, 18.65, 28.60$ and 33.57 , where τ is in units of the linear evolution time T_L of the slowest wave mode in the system. The dashed green line represents the linear wave frequency $\omega_k = k^2$. We observe asymmetry of the dispersion curve in figures (b) and (d) with respect to positive/negative wave numbers.

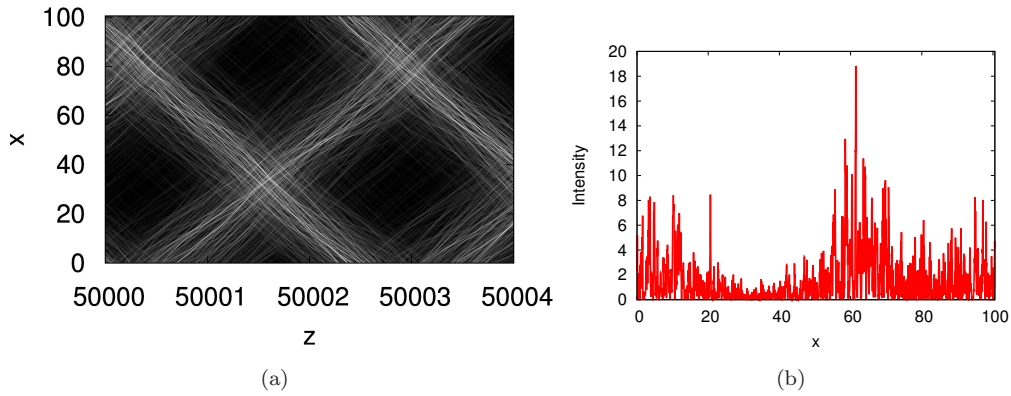


Figure 45: (a) Distribution of $I(x, z)$ at late times in the simulation of the SWE. (b) We plot a time slice $I(x)$ at distance $z = 50001$. In (a) we observe coherent structures propagating with constant speed. In (b) we observe a snapshot of the condensate structure.

which is realized in a 1D setup based on a LC cell, and that serves us as a basic example to which we refer when developing the theoretical framework for 1D OWT. We showed, by starting with an initial condition of weakly nonlinear waves, we were able, by the inverse wave action cascade described by WT theory, to show the formation of strongly nonlinear solitons. One intriguing aspect of OWT is the inverse cascade, where wave action is transported to large scales. This process is analogous to BEC in super-cooled alkali gases. We demonstrated this process in the experimental implementation of 1D OWT. We showed that by injecting high frequency waves into a nonlinear LC cell, we observed a wave turbulent inverse cascade, followed by the condensation of incoherent photons into coherent solitons. Moreover, we supported the experimental findings by performing numerical simulation of the LWE. Analysis of the inverse cascade by WT theory predicted that a pure KZ state was not realizable. Although the KZ spectra are unrealizable, the OWT system is still a very interesting object which is rich in physical effects and mathematical structure. We show how coherent solitons are formed by nonlinear interactions out of random incoherent waves, and analyze the importance of the soliton behavior with the random wave background. Additionally, we determined that the inverse cascade can be described by a mixed wave action spectrum of thermal and non-equilibrium parts. The inverse cascade is associated with the growth of nonlinearity of the system, gradually resulting in the formation of solitons by MI. We observed solitons in both the experiment and numerical simulations, and found that the system relaxes to a state of a single dominant soliton. During the transition to this final state, we observed interactions between solitons and the random wave background. With the aid of WT theory, we developed a strong WT description for the behavior of the system in the form of a WTLC. The WTLC diagrammatically represents the behavior of the coexistence of coherent solitons and the incoherent random wave background.

In addition to the experimental setup, we performed numerical simulations of the LWE and SWE in non-equilibrium stationary regimes in forced-dissipated systems. This allowed for the subsequent testing of the KZ solutions. Theoretically we discovered that the LWE emits fluxes of opposite sign to what is necessary for the KZ states, and this was further verified by a lack of agreement of the wave action spectrum to the KZ solutions. Conversely, this problem does not occur for the SWE. However, we showed that both the KZ for the SWE are non-local and thus should be non-realizable. Nevertheless, we observed good agreements to the KZ predictions for both the direct and inverse cascades. Further investigation into the fluxes yielded a non-constant energy flux for the direct cascade (not shown) - a constant flux being an essential requirement for a local KZ solution. This indicates that we observed a possible non-local wave action spectrum and if so, we are led to ask what non-local process determines this power law? The answer to this can be determined with a development of a non-local theory for 1D OWT in the short-wave limit - which is a future goal of ours. The inverse cascade for the SWE yielded an excellent agreement to the KZ solution and a good indication of a constant negative flux of wave action (not shown). This suggests that the inverse cascade is of KZ type, contradicting the non-locality analysis and thus raising questions in itself. Thus further analysis of the numerical prefactor of the wave action spectrum is required and a possible explanation of the observations via a non-local theory. Further, in the inverse cascade simulation of the SWE, we found a new fascinating physical phenomenon - generation of meandering solitons organized in crisscrossing bundles. Theoretical explanation for such a behavior or possible experimental implementations are yet to be constructed.

In trying to tackle OWT, we have ended with more questions than answers. We have observed very rich behavior with numerous interesting physical effects which potentially could come useful for technological applications insofar as optical solitons are considered as potential candidates for optical interconnect and information processing. However, there remains a lack of a solid theory for explaining the observed results, and some of these results appear to be in contradiction with the classical WT analysis. Thus, we consider this review as a report summarizing the first stage OWT studies, with an open discussion of the observed results, theoretical advances and remaining puzzles. Our analysis has raised several new questions that need to be addressed with additional experiments and numerical simulations. There is yet to be done an experimental investigation of higher dimensional OWT, which we believe is a natural extension to the research presented in this report. In addition, the description of the evolution of solitons, with the possible understanding of their behavior and manipulation would be valuable to any future applications in nonlinear optics. In this context OWT represents a challenging step forward, providing the occurrence of spontaneous increase of coherence of light through weakly nonlinear wave interactions.

6. Acknowledgements

We acknowledge helpful discussions with V. Zakharov and with G. Assanto. We gratefully acknowledge the Referee for precious remarks and suggestions. This work has been partially supported by the Royal Societys International Joint Project grant. U.B. and S.R. acknowledge support of the project ANR-07-BLAN-0246-03, "*turbonde*" and of the ANR international program, project ANR-2010-INTB-402-02 "*COLORS*".

Appendices

A. The Canonical Transformation

In this Appendix, we will outline the details of applying the CT to a six-wave system with non-resonant four-wave interactions. This procedure is adapted from [3], where a CT was used for converting a non-resonant three-wave system into one with resonant four-wave interactions. The fundamental goal of the CT is to remove the leading order non-resonant four-wave interactions by re-defining the canonical variable by a quasi-nonlinear canonical transformation. This will preserve the system's linear dynamics whilst removing the lowest order non-resonant dynamics. The result will be a system that contains resonant wave interactions at its lowest order.

To begin, we must define a new canonical interaction variable, $c_{\mathbf{k}}$, such that it satisfies an auxiliary Hamiltonian, \mathcal{H}_{aux} , in the sense that it contains arbitrary interaction coefficients at all orders⁴. We can define a general auxiliary Hamiltonian, up to order six, for $c_{\mathbf{k}}$ as:

$$\begin{aligned}
\mathcal{H}_{aux} = & \frac{1}{2} \sum_{1,2,3} \tilde{V}_3^{1,2} \delta_3^{1,2} (c_1 c_2 c_3^* + \text{c.c.}) + \frac{1}{6} \sum_{1,2,3} \tilde{U}^{1,2,3} \delta^{1,2,3} (c_1 c_2 c_3 + \text{c.c.}) \\
& + \frac{1}{4} \sum_{1,2,3,4} \tilde{T}_{3,4}^{1,2} \delta_{3,4}^{1,2} c_1 c_2 c_3^* c_4^* + \frac{1}{6} \sum_{1,2,3,4} \tilde{X}_4^{1,2,3} \delta_4^{1,2,3} (c_1 c_2 c_3 c_4^* + \text{c.c.}) \\
& + \frac{1}{24} \sum_{1,2,3,4} \tilde{Y}^{1,2,3,4} \delta^{1,2,3,4} (c_1 c_2 c_3 c_4 + \text{c.c.}) \\
& + \frac{1}{120} \sum_{1,2,3,4,5} \tilde{A}^{1,2,3,4,5} \delta^{1,2,3,4,5} (c_1 c_2 c_3 c_4 c_5 + \text{c.c.}) \\
& + \frac{1}{24} \sum_{1,2,3,4,5} \tilde{B}_5^{1,2,3,4} \delta_5^{1,2,3,4} (c_1 c_2 c_3 c_4 c_5^* + \text{c.c.}) \\
& + \frac{1}{12} \sum_{1,2,3,4,5} \tilde{C}_{4,5}^{1,2,3} \delta_{4,5}^{1,2,3} (c_1 c_2 c_3 c_4^* c_5^* + \text{c.c.}) \\
& + \frac{1}{36} \sum_{1,2,3,4,5,6} \tilde{W}_{4,5,6}^{1,2,3} \delta_{4,5,6}^{1,2,3} c_1 c_2 c_3 c_4^* c_5^* c_6^* \\
& + \frac{1}{120} \sum_{1,2,3,4,5,6} \tilde{Q}_6^{1,2,3,4,5} \delta_6^{1,2,3,4,5} (c_1 c_2 c_3 c_4 c_5 c_6^* + \text{c.c.}) \\
& + \frac{1}{48} \sum_{1,2,3,4,5,6} \tilde{R}_{5,6}^{1,2,3,4} \delta_{5,6}^{1,2,3,4} (c_1 c_2 c_3 c_4 c_5^* c_6^* + \text{c.c.}) \\
& + \frac{1}{36} \sum_{1,2,3,4,5,6} \tilde{S}^{1,2,3,4,5,6} \delta^{1,2,3,4,5,6} (c_1 c_2 c_3 c_4 c_5 c_6 + \text{c.c.}). \tag{A.1}
\end{aligned}$$

⁴We have defined the auxiliary Hamiltonian up to six-wave interactions, which is sufficient for our systems. This will be verified *a posteriori*.

The auxiliary Hamiltonian is completely arbitrary and as such we denote all interaction coefficients with tildes to emphasize this. The idea is to construct a new Hamiltonian, (A.1), for our system in terms of $c_{\mathbf{k}}$ using the original Hamiltonian (16) to determine certain auxiliary interaction coefficients, whilst allowing us to explicitly choose the remaining arbitrary interaction coefficients in (A.1) to eliminate the non-resonant interaction terms of (16).

The CT is weakly nonlinear, thus preserving the linear dynamics of the system. We utilize the fact that the time evolution operator is canonical [3], and then use the Taylor expansion of $a_{\mathbf{k}}$ around $a(\mathbf{k}, 0) = c(\mathbf{k}, 0)$ giving

$$a(\mathbf{k}, z) = c(\mathbf{k}, 0) + z \left(\frac{\partial c(\mathbf{k}, z)}{\partial z} \right) \Big|_{z=0} + \frac{z^2}{2} \left(\frac{\partial^2 c(\mathbf{k}, z)}{\partial z^2} \right) \Big|_{z=0} + \dots \quad (\text{A.2})$$

The coefficients of the CT in (A.2) can be computed using relation (20) applied to the auxiliary Hamiltonian, (A.1), i.e.

$$\left(\frac{\partial c_{\mathbf{k}}}{\partial z} \right)_{z=0} = -i \frac{\delta \mathcal{H}_{aux}}{\delta c_{\mathbf{k}}^*}, \quad (\text{A.3a})$$

$$\left(\frac{\partial^2 c_{\mathbf{k}}}{\partial z^2} \right)_{z=0} = -i \frac{\partial}{\partial z} \frac{\delta \mathcal{H}_{aux}}{\delta c_{\mathbf{k}}^*}. \quad (\text{A.3b})$$

These coefficients will be of the form of summations, involving the canonical variable $c_{\mathbf{k}}$ and the interaction coefficients of the auxiliary Hamiltonian. Coefficient (A.3a) is expressed below, and is simply determined by considering the variational derivative of

the auxiliary Hamiltonian with respect to $c_{\mathbf{k}}^*$:

$$\begin{aligned}
\left(\frac{\partial c(\mathbf{k}, t)}{\partial z}\right)_{t=0} = & -i \left[\frac{1}{2} \sum_{1,2} \tilde{V}_{\mathbf{k}}^{1,2} \delta_{\mathbf{k}}^{1,2} c_1 c_2 + 2 \left(\tilde{V}_2^{\mathbf{k},1}\right)^* \delta_2^{\mathbf{k},1} c_1^* c_2 \right. \\
& + \frac{1}{2} \sum_{1,2} \left(\tilde{U}^{\mathbf{k},1,2}\right)^* \delta^{\mathbf{k},1,2} c_1^* c_2^* + \frac{1}{2} \sum_{1,2,3} \tilde{W}_{\mathbf{k},3}^{1,2} \delta_{\mathbf{k},3}^{1,2} c_1 c_2 c_3^* \\
& + \frac{1}{6} \sum_{1,2,3} \tilde{X}_{\mathbf{k}}^{1,2,3} \delta_{\mathbf{k}}^{1,2,3} c_1 c_2 c_3 + 3 \left(\tilde{X}_3^{\mathbf{k},1,2}\right)^* \delta_3^{\mathbf{k},1,2} c_1^* c_2^* c_3 \\
& + \frac{1}{6} \sum_{1,2,3} \left(\tilde{Y}^{\mathbf{k},1,2,3}\right)^* \delta^{\mathbf{k},1,2,3} c_1^* c_2^* c_3^* \\
& + \frac{1}{24} \sum_{1,2,3,4} \left(\tilde{A}^{\mathbf{k},1,2,3,4}\right)^* \delta^{\mathbf{k},1,2,3,4} c_1^* c_2^* c_3^* c_4^* \\
& + \frac{1}{24} \sum_{1,2,3,4} \tilde{B}_{\mathbf{k}}^{1,2,3,4} \delta_{\mathbf{k}}^{1,2,3,4} c_1 c_2 c_3 c_4 + 4 \left(\tilde{B}_4^{\mathbf{k},1,2,3}\right)^* \delta_4^{\mathbf{k},1,2,3} c_1^* c_2^* c_3^* c_4 \\
& + \frac{1}{12} \sum_{1,2,3,4} 2\tilde{C}_{\mathbf{k},4}^{1,2,3} \delta_{\mathbf{k},4}^{1,2,3} c_1 c_2 c_3 c_4^* + 3 \left(\tilde{C}_{3,4}^{\mathbf{k},1,2}\right)^* \delta_{3,4}^{\mathbf{k},1,2} c_1^* c_2^* c_3 c_4 \\
& + \frac{1}{12} \sum_{1,2,3,4,5} \tilde{T}_{\mathbf{k},4,5}^{1,2,3} \delta_{\mathbf{k},4,5}^{1,2,3} c_1 c_2 c_3 c_4^* c_5^* \\
& + \frac{1}{120} \sum_{1,2,3,4,5} \tilde{Q}_{\mathbf{k}}^{1,2,3,4,5} \delta_{\mathbf{k}}^{1,2,3,4,5} c_1 c_2 c_3 c_4 c_5 \\
& + 5 \left(\tilde{Q}_5^{\mathbf{k},1,2,3,4}\right)^* \delta_5^{\mathbf{k},1,2,3,4} c_1^* c_2^* c_3^* c_4^* c_5 \\
& + \frac{1}{48} \sum_{1,2,3,4,5} 2\tilde{R}_{\mathbf{k},5}^{1,2,3,4} \delta_{\mathbf{k},5}^{1,2,3,4} c_1 c_2 c_3 c_4 c_5^* \\
& + 4 \left(\tilde{R}_{4,5}^{\mathbf{k},1,2,3}\right)^* \delta_{4,5}^{\mathbf{k},1,2,3} c_1^* c_2^* c_3^* c_4 c_5 \\
& \left. + \frac{1}{6} \sum_{1,2,3,4,5} \left(\tilde{S}^{\mathbf{k},1,2,3,4,5}\right)^* \delta^{\mathbf{k},1,2,3,4,5} c_1^* c_2^* c_3^* c_4^* c_5^* \right]. \quad (\text{A.4})
\end{aligned}$$

The second coefficient, (A.3b), is derived by taking the time derivative of (A.4) and then re-substituting the expression for $\dot{c}_{\mathbf{k}}$ from (A.4). As one can expect, this leads to a lengthy formula which we omit from the review due to space restrictions. With the full expression of the CT found in terms of $c_{\mathbf{k}}$ s, we then substitute the CT (A.2) into the Hamiltonian (16). The result will be an expression of the Hamiltonian in terms of the new interaction representation variable $c_{\mathbf{k}}$. The Hamiltonian will involve the interaction coefficients from the auxiliary Hamiltonian (containing tildes) and $T_{3,4}^{1,2}$. The aim is to eliminate the non-resonant four-wave interaction contribution by selecting the values of the arbitrary interaction coefficients. Moreover, as the system conserves wave action, we find that the CT does not result in any additional odd N -wave contributions, hence all arbitrary interaction coefficients for odd orders are automatically zero.

We find that elimination of all non-resonant four-wave contributions can be achieved by selecting

$$\tilde{T}_{3,4}^{1,2} = \frac{-4i \left(T_{3,4}^{1,2}\right)^*}{\omega_1 + \omega_2 - \omega_3 - \omega_4}. \quad (\text{A.5})$$

Relation (A.5) is valid as the denominator does not vanish due to a lack of resonant four-wave interactions (i.e. no non-trivial solutions to the four-wave resonance condition (23)). After selecting (A.5), we find that Hamiltonian (16) reduces to

$$\begin{aligned} \mathcal{H} = & \sum_{\mathbf{k}} \omega_{\mathbf{k}} c_{\mathbf{k}} c_{\mathbf{k}}^* + \frac{1}{36} \sum_{1,2,3,4,5,6} \left[\mathcal{W}_{4,5,6}^{1,2,3} - i(\omega_1 + \omega_2 + \omega_3 - \omega_4 - \omega_5 - \omega_6) \right. \\ & \left. \times \tilde{W}_{4,5,6}^{1,2,3} \right] \delta_{4,5,6}^{1,2,3} c_1 c_2 c_3 c_4^* c_5^* c_6^*. \end{aligned} \quad (\text{A.6})$$

Hamiltonian (A.6) represents Hamiltonian (16) in the new canonical variable $c_{\mathbf{k}}$, up to the leading resonant wave interaction, in this case being of order six. Notice, that within the six-wave contribution there is still an arbitrary contribution, $\tilde{W}_{4,5,6}^{1,2,3}$, that arises from the auxiliary Hamiltonian (A.1). However, its prefactor, $\omega_1 + \omega_2 + \omega_3 - \omega_4 - \omega_5 - \omega_6$, vanishes when the six-wave resonance condition

$$\mathbf{k}_1 + \mathbf{k}_2 + \mathbf{k}_3 = \mathbf{k}_4 + \mathbf{k}_5 + \mathbf{k}_6, \quad (\text{A.7a})$$

$$\omega(\mathbf{k}_1) + \omega(\mathbf{k}_2) + \omega(\mathbf{k}_3) = \omega(\mathbf{k}_4) + \omega(\mathbf{k}_5) + \omega(\mathbf{k}_6), \quad (\text{A.7b})$$

is satisfied. Ultimately, $\tilde{W}_{4,5,6}^{1,2,3}$ does not provide a contribution to the nonlinear wave dynamics. Therefore, we may set $\tilde{W}_{4,5,6}^{1,2,3}$ to equal anything without altering the nonlinear wave dynamics. For convenience we select $\tilde{W}_{4,5,6}^{1,2,3}$ to equal minus the difference of $\mathcal{W}_{4,5,6}^{1,2,3}$ from the value taken when the resonance condition, (A.7), is satisfied. For instance, if we decompose $\mathcal{W}_{4,5,6}^{1,2,3}$ into two parts, the first being its value when the resonant condition is satisfied, say ${}^{RC}\mathcal{W}_{4,5,6}^{1,2,3}$ and the second being its residual ${}^{\perp}\mathcal{W}_{4,5,6}^{1,2,3} = \mathcal{W}_{4,5,6}^{1,2,3} - {}^{RC}\mathcal{W}_{4,5,6}^{1,2,3}$, i.e. we can then express

$$\mathcal{W}_{4,5,6}^{1,2,3} = {}^{RC}\mathcal{W}_{4,5,6}^{1,2,3} + {}^{\perp}\mathcal{W}_{4,5,6}^{1,2,3}. \quad (\text{A.8})$$

By choosing

$$\tilde{W}_{4,5,6}^{1,2,3} = \frac{-i {}^{\perp}\mathcal{W}_{4,5,6}^{1,2,3}}{\omega_1 + \omega_2 + \omega_3 - \omega_4 - \omega_5 - \omega_6}, \quad (\text{A.9})$$

the arbitrary interaction coefficient, $\tilde{W}_{4,5,6}^{1,2,3}$, directly cancels with the residual contribution ${}^{\perp}\mathcal{W}_{4,5,6}^{1,2,3}$. This means that the six-wave interaction coefficient will equal its value on the six-wave resonance condition over the whole of the domain. The final result yields the Hamiltonian expressed as equation (24).

B. Details and Assumptions of Weak Wave Turbulence Theory

In this Appendix, we will outline the main technical details in deriving the evolution equations for the one-mode amplitude PDF and for the wave action density $n_{\mathbf{k}}$. The means to do this is by constructing an evolution equation for a generating functional (GF) that can generate evolution equations for all the statistical quantities in the wave system.

This approach can be applied to a general N -mode wave system⁵. However, we will only concentrate on the one-mode statistics of the system for brevity. Subsequently, we will only need to consider the one-mode amplitude GF defined as

$$\mathcal{Z}_{\mathbf{k}}(\lambda_{\mathbf{k}}) = \left\langle e^{\left(\frac{\lambda}{2\pi}\right)\lambda_{\mathbf{k}}J_{\mathbf{k}}} \right\rangle, \quad (\text{B.1})$$

where $J_{\mathbf{k}} = |a_{\mathbf{k}}|^2$ for wave number \mathbf{k} . Besides from deriving all the statistical moments of the wave field $a_{\mathbf{k}}$ from the GF, we can also obtain the one-mode PDF for wave intensities $J_{\mathbf{k}}$ by taking the inverse Laplace transform of the one-mode amplitude GF:

$$\mathcal{P}_{\mathbf{k}}(s_{\mathbf{k}}) = \frac{1}{2\pi i} \int_{-i\infty+c}^{i\infty+c} e^{-\left(\frac{\lambda}{2\pi}\right)\lambda_{\mathbf{k}}s_{\mathbf{k}}} \mathcal{Z}_{\mathbf{k}}(\lambda_{\mathbf{k}}) d\lambda_{\mathbf{k}}, \quad (\text{B.2})$$

where c is a constant greater than the real part of all singularities.

Now we will derive the evolution equation for the GF starting with the first step - the weak nonlinearity expansion.

B.1. The Weak Nonlinearity Expansion

The WT strategy exploits the separation of the linear and nonlinear timescales. Namely, when considering a weakly nonlinear regime, (when wave amplitudes are small), the linear evolution time,

$$T_{\text{L}} = \frac{2\pi}{\omega_k}, \quad (\text{B.3})$$

is much smaller than the nonlinear evolution time T_{NL} - the characteristic time for the nonlinear transfer of energy between waves. This separation of timescales allows for an expansion in terms of a small parameter and then we make an average over the fast linear dynamics. The result is a description of the nonlinear evolution of the wave system. First of all we note that the leading order nonlinear effects arise from the diagonal terms in the sum corresponding to the nonlinear interaction. These terms correspond to the trivial pairings of wave numbers in equation (27), which do not contribute to the nonlinear exchange of energy between wave modes, but do provide an additional contribution to the frequency. Consequently, before we can proceed, we must isolate this contribution to ensure that the weak nonlinearity expansion will be defined in a self-consistent way [116]. By separating the diagonal terms from the main summation, equation (27) can be expressed as

$$i\dot{c}_{\mathbf{k}} = (\omega_k + \Omega_k) c_{\mathbf{k}} + \frac{1}{12} \sum_{\mathcal{K}_{4,5,6}^{2,3}} \mathcal{W}_{4,5,6}^{\mathbf{k},2,3} c_2^* c_3^* c_4 c_5 c_6 \delta_{4,5,6}^{\mathbf{k},2,3}, \quad (\text{B.4})$$

where

$$\Omega_k = \frac{1}{2} \sum_{7,8} \mathcal{W}_{\mathbf{k},7,8}^{\mathbf{k},7,8} |c_7|^2 |c_8|^2. \quad (\text{B.5})$$

⁵There exist several papers that consider the full N -mode statistics of three-wave and four-wave systems, for instance see [116, 114].

The summation in (B.4) is now taken over the set $\mathcal{K}_{4,5,6}^{2,3} = \{\mathbf{k}_2, \mathbf{k}_3, \mathbf{k}_4, \mathbf{k}_5, \mathbf{k}_6 : \mathbf{k}, \mathbf{k}_2, \mathbf{k}_3 \neq \mathbf{k}_4, \mathbf{k}_5, \mathbf{k}_6\}$. We see that the nonlinear frequency Ω_k acts as a correction to the linear wave frequency, so that the system evolves with an effective wave frequency of $\tilde{\omega}_k = \omega_k + \Omega_k$.

Let us define a scaled interaction representation variable $b_{\mathbf{k}}$, so that it evolves on the slow nonlinear scale. This is achieved by compensating for the fast oscillating factor by

$$b_{\mathbf{k}} = \frac{c_{\mathbf{k}}}{\epsilon} e^{i\omega_k z + i \int_0^z \Omega_k dz'}. \quad (\text{B.6})$$

Note that we have incorporated the nonlinear frequency correction Ω_k into the oscillating factor, so that the variable $b_{\mathbf{k}}$ varies only at the timescale of the energy transfer between the modes. We have also divided the right-hand side by a formal small parameter $\epsilon \ll 1$ for easier power counting of the nonlinearity orders (thus formally defining $b_{\mathbf{k}}$ to be $\mathcal{O}(1)$). Substitution of formula (B.6) into equation (B.4) gives

$$i\dot{b}_{\mathbf{k}} = \frac{\epsilon^4}{12} \sum_{\mathcal{K}_{4,5,6}^{2,3}} \mathcal{W}_{4,5,6}^{\mathbf{k},2,3} b_2^* b_3^* b_4 b_5 b_6 \delta_{4,5,6}^{\mathbf{k},2,3} e^{i\omega_{4,5,6}^{k,2,3} z + i\epsilon^4 \int_0^z \Omega_{4,5,6}^{k,2,3} dz'}, \quad (\text{B.7})$$

where $\omega_{4,5,6}^{k,2,3} = \omega_k + \omega_2 + \omega_3 - \omega_4 - \omega_5 - \omega_6$ and $\Omega_{4,5,6}^{k,2,3} = \Omega_k + \Omega_2 + \Omega_3 - \Omega_4 - \Omega_5 - \Omega_6$. As the nonlinear frequency correction is time-dependent, extra care should be taken when considering its contribution to (B.7). To separate the slow and the fast timescales, let us choose an auxiliary intermediate time T ,

$$T_L \ll T \ll T_{\text{NL}}. \quad (\text{B.8})$$

For small wave amplitudes, $|c_{\mathbf{k}}| \sim \epsilon \ll 1$, the nonlinear timescale for a six-wave process is of the order $T_{\text{NL}} \sim 2\pi/\epsilon^8 \omega_k$, which will be verified *a posteriori*. Thus, to be specific, let us take $T = 2\pi/\epsilon^4 \omega_k$.

The main objective is to seek a solution for $b_{\mathbf{k}}$, at the intermediate time T in the form of an ϵ -expansion

$$b_{\mathbf{k}}(T) = b_{\mathbf{k}}^{(0)} + \epsilon^4 b_{\mathbf{k}}^{(1)} + \epsilon^8 b_{\mathbf{k}}^{(2)} + \dots, \quad (\text{B.9})$$

and then solve each ϵ -order of $b_{\mathbf{k}}(T)$ by an iterative method using evolution equation (B.7). We substitute (B.9) into (B.7), and equate ϵ -orders. The leading $\mathcal{O}(\epsilon^0)$ contribution gives

$$i\dot{b}_{\mathbf{k}}^{(0)}(T) = b_{\mathbf{k}}^{(0)}(0) = b_{\mathbf{k}}(0). \quad (\text{B.10})$$

Result (B.10), implies that at leading order, the wave amplitude $b_{\mathbf{k}}(T)$ is time-independent.

In the following order, $\mathcal{O}(\epsilon^4)$, we get

$$b_{\mathbf{k}}^{(1)}(T) = -\frac{i}{12} \sum_{\mathcal{K}_{4,5,6}^{2,3}} \mathcal{W}_{4,5,6}^{\mathbf{k},2,3} b_2^{(0)*} b_3^{(0)*} b_4^{(0)} b_5^{(0)} b_6^{(0)} \delta_{4,5,6}^{\mathbf{k},2,3} \Delta_T \left(\omega_{4,5,6}^{k,2,3} + {}^{(0)}\Omega_{4,5,6}^{k,2,3} \right). \quad (\text{B.11})$$

Here we have used that $b_{\mathbf{k}}^{(1)}(0) = 0$ and have defined

$$\Delta_T(x) = \int_0^T e^{ixz} dz = \frac{e^{ixT} - 1}{ix}. \quad (\text{B.12})$$

and ${}^{(0)}\Omega_{4,5,6}^{k,2,3} = \Omega_k^{(0)} + \Omega_2^{(0)} + \Omega_3^{(0)} - \Omega_4^{(0)} - \Omega_5^{(0)} - \Omega_6^{(0)}$ where

$$\Omega_k^{(0)} = \frac{\epsilon^4}{2} \sum_{7,8} \mathcal{W}_{\mathbf{k},7,8}^{\mathbf{k},7,8} |b_7^{(0)}|^2 |b_8^{(0)}|^2. \quad (\text{B.13})$$

Note that, even though $\Omega_k^{(0)} \sim \mathcal{O}(\epsilon^4)$, the factor $e^{i^{(0)}\Omega_{4,5,6}^{k,2,3}T}$ is $\mathcal{O}(1)$ because $T \sim \epsilon^{-4}$. Therefore, the ϵ -orders of the left-hand side and the right-hand side are the same. In other words, it would be wrong to expand the exponential function in small ϵ here. The next order correction to Ω_k is indeed small enough ($\sim \epsilon^8$) so that the exponential could be expanded, but its contribution would be nullified by the phase averaging (see below).

Finally, we use formulae (B.10) and (B.11) to determine $b_{\mathbf{k}}^{(2)}(T)$:

$$\begin{aligned} b_{\mathbf{k}}^{(2)} &= \frac{1}{12} \sum_{\substack{\mathcal{K}_{4,5,6}^{2,3} \\ \mathcal{K}_{9,10,11}^{7,8}}} \left[2\mathcal{W}_{4,5,6}^{\mathbf{k},2,3} \left(\mathcal{W}_{9,10,11}^{2,7,8} \right)^* b_3^{(0)*} b_9^{(0)*} b_{10}^{(0)*} b_{11}^{(0)*} b_4^{(0)} b_5^{(0)} b_6^{(0)} b_7^{(0)} b_8^{(0)} \right. \\ &\quad \times \delta_{4,5,6}^{\mathbf{k},2,3} \delta_{9,10,11}^{2,7,8} E_T \left(\left({}^{(0)}\tilde{\omega}_{9,10,11}^{2,7,8} \right)^*, {}^{(0)}\tilde{\omega}_{4,5,6}^{k,2,3} \right) - 3\mathcal{W}_{4,5,6}^{\mathbf{k},2,3} \mathcal{W}_{9,10,11}^{4,7,8} \\ &\quad \left. \times b_2^{(0)*} b_3^{(0)*} b_7^{(0)*} b_8^{(0)*} b_5^{(0)} b_6^{(0)} b_9^{(0)} b_{10}^{(0)} b_{11}^{(0)} \delta_{4,5,6}^{\mathbf{k},2,3} \delta_{9,10,11}^{4,7,8} E_T \left({}^{(0)}\tilde{\omega}_{9,10,11}^{4,7,8}, {}^{(0)}\tilde{\omega}_{4,5,6}^{k,2,3} \right) \right], \end{aligned} \quad (\text{B.14})$$

where we have defined $E_T(x, y)$ as

$$E_T(x, y) = \int_0^T \Delta_z(x) e^{i \int_0^z y dz'} dz, \quad (\text{B.15})$$

and ${}^{(0)}\tilde{\omega}_{4,5,6}^{k,2,3} = \tilde{\omega}_{4,5,6}^{k,2,3} + {}^{(0)}\Omega_{4,5,6}^{k,2,3}$. The symmetry of $\Delta_T(x)$ implies that $E_T(x^*, y) = E_T(-x, y)$. With equations (B.10), (B.11) and (B.14), we have calculated the ϵ -expansion of $b_{\mathbf{k}}$ up to $\mathcal{O}(\epsilon^8)$. This order is sufficient for the analysis contained within this review. The next objective is to substitute the above expansion into the definition of GF, thereby finding the solution for GF at the intermediate time T .

B.2. Equation for the Generating Functional

Recall that the one-mode amplitude GF is defined in (B.1) where we can substitute $J_{\mathbf{k}} = |b_{\mathbf{k}}|^2$. The aim is to calculate the ϵ -expansion of $\mathcal{Z}_{\mathbf{k}}$ at the intermediate time, T , and subsequently, derive an evolution equation, using the results of the previous Subsection. Assume that we can represent the GF in powers of ϵ as

$$\mathcal{Z}_{\mathbf{k}} = \mathcal{Z}_{\mathbf{k}}^{(0)} + \epsilon^4 \mathcal{Z}_{\mathbf{k}}^{(1)} + \epsilon^8 \mathcal{Z}_{\mathbf{k}}^{(2)} + \dots. \quad (\text{B.16})$$

Then to calculate the GF, we must average over random phases, $\langle \cdot \rangle_{\phi}$, and random amplitudes, $\langle \cdot \rangle_J$, in an initial RPA field. Once we have performed these, we can derive the evolution equation for $\mathcal{Z}_{\mathbf{k}}$, and thus any of the one-mode statistical objects we require.

Now we will perform phase and amplitude averaging over a RPA field for the derivation of the evolution equation for the GF. To achieve this, we express the GF in powers of ϵ , and represent each order in terms of the variable $b_{\mathbf{k}}^{(0)}$. At this stage, we can average over phases by assuming a RPA field. Once, phase averaged, we can average over amplitudes and compute the evolution equation.

To begin, we substitute the ϵ -expansion of $b_{\mathbf{k}}$, (B.9), into definition (B.1) and consider terms up to $\mathcal{O}(\epsilon^8)$. Further simplification can be achieved by Taylor expansion of each exponential⁶, thus obtaining

$$\begin{aligned} \mathcal{Z}_{\mathbf{k}} = & \left\langle e^{\left(\frac{L}{2\pi}\right)\lambda_{\mathbf{k}}|b_{\mathbf{k}}^{(0)}|^2} \left[1 + \epsilon^4 \left(\frac{L}{2\pi}\right) \lambda_{\mathbf{k}} \left(b_{\mathbf{k}}^{(0)} b_{\mathbf{k}}^{(1)*} + b_{\mathbf{k}}^{(0)*} b_{\mathbf{k}}^{(1)} \right) \right. \right. \\ & + \epsilon^8 \left(\left(\frac{L}{2\pi}\right) \lambda_{\mathbf{k}} \left(|b_{\mathbf{k}}^{(1)}|^2 + b_{\mathbf{k}}^{(0)} b_{\mathbf{k}}^{(2)*} + b_{\mathbf{k}}^{(0)*} b_{\mathbf{k}}^{(2)} \right) \right. \\ & \left. \left. + \left(\frac{L}{2\pi}\right)^2 \frac{\lambda_{\mathbf{k}}^2}{2} \left(b_{\mathbf{k}}^{(0)} b_{\mathbf{k}}^{(1)*} + b_{\mathbf{k}}^{(0)*} b_{\mathbf{k}}^{(1)} \right)^2 \right] \right\rangle + \mathcal{O}(\epsilon^{12}). \end{aligned} \quad (\text{B.17})$$

We now proceed by averaging each term in expansion (B.17). The leading $\mathcal{O}(\epsilon^0)$ contribution of $\mathcal{Z}_{\mathbf{k}}$ is given by

$$\mathcal{Z}_{\mathbf{k}}^{(0)} = \left\langle e^{\left(\frac{L}{2\pi}\right)\lambda_{\mathbf{k}}|b_{\mathbf{k}}^{(0)}|^2} \right\rangle = \left\langle e^{\left(\frac{L}{2\pi}\right)\lambda_{\mathbf{k}}J_{\mathbf{k}}^{(0)}} \right\rangle = \mathcal{Z}_{\mathbf{k}}(0), \quad (\text{B.18})$$

where $J_{\mathbf{k}}^{(0)} = |b_{\mathbf{k}}^{(0)}|^2$ is the amplitude of the interaction variable $b_{\mathbf{k}}^{(0)}$. For clarity, we shall omit the superscript of $J_{\mathbf{k}}^{(0)}$ which will thus become $J_{\mathbf{k}}$ ⁷. The leading order of the ϵ -expansion is labeled as $\mathcal{Z}_{\mathbf{k}}(0)$, corresponding to the initial value of the GF. The next order yields

$$\mathcal{Z}_{\mathbf{k}}^{(1)} = \left\langle \left(\frac{L}{2\pi}\right) \lambda_{\mathbf{k}} e^{\left(\frac{L}{2\pi}\right)\lambda_{\mathbf{k}}J_{\mathbf{k}}} \left(b_{\mathbf{k}}^{(0)} b_{\mathbf{k}}^{(1)*} + b_{\mathbf{k}}^{(0)*} b_{\mathbf{k}}^{(1)} \right) \right\rangle, \quad (\text{B.19})$$

and subsequently at the final order to be considered, we obtain

$$\begin{aligned} \mathcal{Z}_{\mathbf{k}}^{(2)} = & \left\langle \left(\frac{L}{2\pi}\right) \lambda_{\mathbf{k}} e^{\left(\frac{L}{2\pi}\right)\lambda_{\mathbf{k}}J_{\mathbf{k}}} \left[|b_{\mathbf{k}}^{(1)}|^2 + b_{\mathbf{k}}^{(0)} b_{\mathbf{k}}^{(2)*} + b_{\mathbf{k}}^{(0)*} b_{\mathbf{k}}^{(2)} \right. \right. \\ & \left. \left. + \left(\frac{L}{2\pi}\right) \frac{\lambda_{\mathbf{k}}}{2} \left(2J_{\mathbf{k}}|b_{\mathbf{k}}^{(1)}|^2 + \left(b_{\mathbf{k}}^{(0)} b_{\mathbf{k}}^{(1)*} \right)^2 + \left(b_{\mathbf{k}}^{(0)*} b_{\mathbf{k}}^{(1)} \right)^2 \right) \right] \right\rangle. \end{aligned} \quad (\text{B.20})$$

Having expressed $\mathcal{Z}_{\mathbf{k}}$ in terms of $b_{\mathbf{k}}$, we now proceed by evaluating the ensemble averages.

We must take the phase average before considering the amplitude average. In the expansion for the GF we can identify three distinct terms, these are $\langle b_{\mathbf{k}}^{(0)} b_{\mathbf{k}}^{(1)*} \rangle$, $\langle |b_{\mathbf{k}}^{(1)}|^2 \rangle$, and $\langle b_{\mathbf{k}}^{(0)} b_{\mathbf{k}}^{(2)*} \rangle$. We implement Wick's rule, which states that the only contributions are those where one can pairwise match the wave numbers. However, due to the trivial pairings leading to the nonlinear frequency correction, we are restricted to which wave numbers can be matched⁸. Consequently, for $\langle b_{\mathbf{k}}^{(0)} b_{\mathbf{k}}^{(1)*} \rangle$ no pairings can occur and thus the average is zero. This is also the case for $\langle \left(b_{\mathbf{k}}^{(0)} b_{\mathbf{k}}^{(1)*} \right)^2 \rangle_{\phi}$ and so gives zero.

In the case of $\langle |b_{\mathbf{k}}^{(1)}|^2 \rangle$, we are able to match the wave numbers in such a way as to not contradict the restrictions of the summations. Applying Wick's rule, we find that

$$\begin{aligned} & \left\langle b_2^{(0)*} b_3^{(0)*} b_9^{(0)*} b_{10}^{(0)*} b_{11}^{(0)*} b_4^{(0)} b_5^{(0)} b_6^{(0)} b_7^{(0)} b_8^{(0)} \right\rangle_{\phi} = (\delta_7^2 \delta_8^3 + \delta_8^2 \delta_7^3) \\ & \times \left[\delta_9^4 (\delta_{10}^5 \delta_{11}^6 + \delta_{11}^5 \delta_{10}^6) + \delta_{10}^4 (\delta_9^5 \delta_{11}^6 + \delta_{11}^5 \delta_9^6) + \delta_{11}^4 (\delta_9^5 \delta_{10}^6 + \delta_{10}^5 \delta_9^6) \right]. \end{aligned} \quad (\text{B.21})$$

⁶This will not alter the the accuracy of the derivation.

⁷Note that now $J_{\mathbf{k}}$ is not the amplitude of the *full* interaction variable $b_{\mathbf{k}}$, as defined in Section 3.

⁸See the definition of set $\mathcal{K}_{4,5,6}^{2,3}$.

This gives

$$\left\langle |b_{\mathbf{k}}^{(1)}|^2 \right\rangle_{\phi} = \frac{1}{12} \sum_{\mathcal{K}_{4,5,6}^{2,3}} |\mathcal{W}_{4,5,6}^{\mathbf{k},2,3}|^2 J_2 J_3 J_4 J_5 J_6 \delta_{4,5,6}^{\mathbf{k},2,3} |\Delta_T(\omega_{4,5,6}^{k,2,3})|^2. \quad (\text{B.22})$$

Applying a similar approach to $\langle b_{\mathbf{k}}^{(0)} b_{\mathbf{k}}^{(2)*} \rangle_{\phi}$, which also does not average to zero, we arrive at

$$\begin{aligned} \langle b_{\mathbf{k}}^{(0)} b_{\mathbf{k}}^{(2)*} \rangle_{\phi} &= \frac{1}{12} \sum_{\mathcal{K}_{4,5,6}^{2,3}} |\mathcal{W}_{4,5,6}^{\mathbf{k},2,3}|^2 J_{\mathbf{k}} (J_2 + J_3) J_4 J_5 J_6 \delta_{4,5,6}^{\mathbf{k},2,3} E_T \left(\left(\omega_{4,5,6}^{k,2,3} \right)^*, \omega_{4,5,6}^{k,2,3} \right) \\ &\quad - \frac{1}{12} \sum_{\mathcal{K}_{4,5,6}^{2,3}} |\mathcal{W}_{4,5,6}^{\mathbf{k},2,3}|^2 J_{\mathbf{k}} J_2 J_3 (J_4 J_5 + J_4 J_6 + J_5 J_6) \delta_{4,5,6}^{\mathbf{k},2,3} \\ &\quad \times E_T^* \left(\omega_{k,2,3}^{4,5,6}, \omega_{4,5,6}^{k,2,3} \right). \end{aligned} \quad (\text{B.23})$$

By defining the wave action spectrum $n_{\mathbf{k}}$, and the derivative of the GF with respect to $\lambda_{\mathbf{k}}$ as

$$n_{\mathbf{k}} = \left(\frac{L}{2\pi} \right) \langle J_{\mathbf{k}} \rangle_J, \quad (\text{B.24a})$$

$$\frac{\partial \mathcal{Z}_{\mathbf{k}}}{\partial \lambda_{\mathbf{k}}} = \frac{\partial}{\partial \lambda_{\mathbf{k}}} \left\langle e^{i \left(\frac{L}{2\pi} \right) \lambda_{\mathbf{k}} J_{\mathbf{k}}} \right\rangle_J = \left\langle \left(\frac{L}{2\pi} \right) J_{\mathbf{k}} e^{i \left(\frac{L}{2\pi} \right) \lambda_{\mathbf{k}} J_{\mathbf{k}}} \right\rangle_J, \quad (\text{B.24b})$$

and using our formulae (B.22) and (B.23), equation (B.16) can be written in the form,

$$\begin{aligned} \mathcal{Z}_{\mathbf{k}}(T) - \mathcal{Z}_{\mathbf{k}}(0) &= \left(\frac{2\pi}{L} \right)^4 \frac{\epsilon^8}{12} \sum_{\mathcal{K}_{4,5,6}^{2,3}} |\mathcal{W}_{4,5,6}^{\mathbf{k},2,3}|^2 \delta_{4,5,6}^{\mathbf{k},2,3} \left[\left(\lambda_{\mathbf{k}} \mathcal{Z}_{\mathbf{k}} + \lambda_{\mathbf{k}}^2 \frac{\partial \mathcal{Z}_{\mathbf{k}}}{\partial \lambda_{\mathbf{k}}} \right) \right. \\ &\quad \times n_2 n_3 n_4 n_5 n_6 \left| \Delta_T \left(\omega_{4,5,6}^{k,2,3} \right) \right|^2 \\ &\quad + 2 \lambda_{\mathbf{k}} \frac{\partial \mathcal{Z}_{\mathbf{k}}}{\partial \lambda_{\mathbf{k}}} (n_2 + n_3) n_4 n_5 n_6 \Re \left[E_T \left(\left(\omega_{4,5,6}^{k,2,3} \right)^*, \omega_{4,5,6}^{k,2,3} \right) \right] \\ &\quad - 2 \lambda_{\mathbf{k}} \frac{\partial \mathcal{Z}_{\mathbf{k}}}{\partial \lambda_{\mathbf{k}}} n_2 n_3 (n_4 n_5 + n_4 n_6 + n_5 n_6) \\ &\quad \left. \times \Re \left[E_T^* \left(\omega_{k,2,3}^{4,5,6}, \omega_{4,5,6}^{k,2,3} \right) \right] \right], \end{aligned} \quad (\text{B.25})$$

up to $\mathcal{O}(\epsilon^{12})$ corrections.

In equation (B.25), we now take the large box and long evolution time (or equivalently the weak nonlinearity) limits. The order in which the limits are taken is essential. We must take the large box limit, $N \rightarrow \infty$, before the weak nonlinearity limit, $T \sim 1/\epsilon^4 \rightarrow \infty$, otherwise the width of the nonlinear resonance broadening will be smaller than the frequency grid spacing, and will therefore result in a zero contribution. For the large box limit, the summations are replaced by integrations of the form: $\lim_{N \rightarrow \infty} \sum_{2,3,4,5,6} = \left(\frac{L}{2\pi} \right)^5 \int d\mathbf{k}_2 d\mathbf{k}_3 d\mathbf{k}_4 d\mathbf{k}_5 d\mathbf{k}_6$ and the Kronecker delta function is transformed into a Dirac delta function with a prefactor of $2\pi/L$. In the weak nonlinearity limit, we can calculate the asymptotic limits of $\Delta_T(x)$:

$$\lim_{T \rightarrow \infty} |\Delta_T(x)|^2 = 2\pi T \delta(x), \quad (\text{B.26})$$

and of $E_T(x, y)$:

$$\lim_{T \rightarrow \infty} \Re[E_T(-x, x)] = \pi T \delta(x). \quad (\text{B.27})$$

Moreover, as the intermediate time T , at which point we want to seek a solution, is smaller than the nonlinear evolution time T_{NL} , we can make an approximation for the time derivative of $Z_{\mathbf{k}}$ by:

$$\dot{Z}_{\mathbf{k}} \approx \frac{Z_{\mathbf{k}}(T) - Z_{\mathbf{k}}(0)}{T}. \quad (\text{B.28})$$

The large box and weak nonlinearity limits, together with results (B.26), (B.27) and (B.28), gives the continuous description of the evolution of the GF:

$$\dot{Z}_{\mathbf{k}} = \lambda_{\mathbf{k}} \eta_{\mathbf{k}} Z_{\mathbf{k}} + (\lambda_{\mathbf{k}}^2 \eta_{\mathbf{k}} - \lambda_{\mathbf{k}} \gamma_{\mathbf{k}}) \frac{\partial Z_{\mathbf{k}}}{\partial \lambda_{\mathbf{k}}}, \quad (\text{B.29})$$

where $\eta_{\mathbf{k}}$ and $\gamma_{\mathbf{k}}$ are defined in the main text as equations (29a) and (29b) respectively. By taking the inverse Laplace transform of (B.29), we get the evolution equation for the amplitude PDF (28).

C. The Zakharov Transform

The ZT is used to find steady state solutions to the KE. The transformation utilizes symmetries of the KE to overlap six disjoint regions of the domain of the collision integral on to one another. From the resulting integrand, one can straightforwardly derive the steady states of the KE. In Section 3.4, we presented the transform on one of these regions. In this Appendix, we give the four remaining transformations:

$$\tilde{\mathbf{k}}_1 = \frac{\tilde{\mathbf{k}}\tilde{\mathbf{k}}'_1}{\tilde{\mathbf{k}}'_2}, \quad \tilde{\mathbf{k}}_2 = \frac{\tilde{\mathbf{k}}^2}{\tilde{\mathbf{k}}'_2}, \quad \tilde{\mathbf{k}}_3 = \frac{\tilde{\mathbf{k}}\tilde{\mathbf{k}}'_3}{\tilde{\mathbf{k}}'_2}, \quad \tilde{\mathbf{k}}_4 = \frac{\tilde{\mathbf{k}}\tilde{\mathbf{k}}'_4}{\tilde{\mathbf{k}}'_2} \quad \text{and} \quad \tilde{\mathbf{k}}_5 = \frac{\tilde{\mathbf{k}}\tilde{\mathbf{k}}'_5}{\tilde{\mathbf{k}}'_2}, \quad (\text{C.1a})$$

with Jacobian $J = -\left(\tilde{\mathbf{k}}/\tilde{\mathbf{k}}'_2\right)^6$.

$$\tilde{\mathbf{k}}_1 = \frac{\tilde{\mathbf{k}}\tilde{\mathbf{k}}'_4}{\tilde{\mathbf{k}}'_3}, \quad \tilde{\mathbf{k}}_2 = \frac{\tilde{\mathbf{k}}\tilde{\mathbf{k}}'_5}{\tilde{\mathbf{k}}'_3}, \quad \tilde{\mathbf{k}}_3 = \frac{\tilde{\mathbf{k}}^2}{\tilde{\mathbf{k}}'_3}, \quad \tilde{\mathbf{k}}_4 = \frac{\tilde{\mathbf{k}}\tilde{\mathbf{k}}'_1}{\tilde{\mathbf{k}}'_3} \quad \text{and} \quad \tilde{\mathbf{k}}_5 = \frac{\tilde{\mathbf{k}}\tilde{\mathbf{k}}'_2}{\tilde{\mathbf{k}}'_3}, \quad (\text{C.1b})$$

with Jacobian $J = -\left(\tilde{\mathbf{k}}/\tilde{\mathbf{k}}'_3\right)^6$.

$$\tilde{\mathbf{k}}_1 = \frac{\tilde{\mathbf{k}}\tilde{\mathbf{k}}'_5}{\tilde{\mathbf{k}}'_4}, \quad \tilde{\mathbf{k}}_2 = \frac{\tilde{\mathbf{k}}\tilde{\mathbf{k}}'_3}{\tilde{\mathbf{k}}'_4}, \quad \tilde{\mathbf{k}}_3 = \frac{\tilde{\mathbf{k}}\tilde{\mathbf{k}}'_2}{\tilde{\mathbf{k}}'_4}, \quad \tilde{\mathbf{k}}_4 = \frac{\tilde{\mathbf{k}}^2}{\tilde{\mathbf{k}}'_4} \quad \text{and} \quad \tilde{\mathbf{k}}_5 = \frac{\tilde{\mathbf{k}}\tilde{\mathbf{k}}'_1}{\tilde{\mathbf{k}}'_4}, \quad (\text{C.1c})$$

with Jacobian $J = -\left(\tilde{\mathbf{k}}/\tilde{\mathbf{k}}'_4\right)^6$.

$$\tilde{\mathbf{k}}_1 = \frac{\tilde{\mathbf{k}}\tilde{\mathbf{k}}'_3}{\tilde{\mathbf{k}}'_5}, \quad \tilde{\mathbf{k}}_2 = \frac{\tilde{\mathbf{k}}\tilde{\mathbf{k}}'_4}{\tilde{\mathbf{k}}'_5}, \quad \tilde{\mathbf{k}}_3 = \frac{\tilde{\mathbf{k}}\tilde{\mathbf{k}}'_1}{\tilde{\mathbf{k}}'_5}, \quad \tilde{\mathbf{k}}_4 = \frac{\tilde{\mathbf{k}}\tilde{\mathbf{k}}'_2}{\tilde{\mathbf{k}}'_5} \quad \text{and} \quad \tilde{\mathbf{k}}_5 = \frac{\tilde{\mathbf{k}}^2}{\tilde{\mathbf{k}}'_5}, \quad (\text{C.1d})$$

with Jacobian $J = -\left(\tilde{\mathbf{k}}/\tilde{\mathbf{k}}'_5\right)^6$.

We re-iterate that these transformations are only applicable if the collision integral is proven to be convergent upon the KZ solutions. If not, then the KZ solutions are deemed non-local and the solutions found using the ZT are unphysical.

D. Expansion of the Long-Wave Six-Wave Interaction Coefficient

As the LWE contains two nonlinear terms, the resulting four-wave interaction coefficient (18a), will also contain two expressions. WT theory relies on that fact that the interaction coefficients are scale invariant. However, both of these expressions express different scalings with respect to the wave number \mathbf{k} (where all four wave numbers are of the same order, i.e. $k_1, k_2, k_3, k_4 \propto k$). However, for the LWE this does not pose a problem because the long-wave limit $kl_\xi \ll 1$, provides a small parameter for us to determine a leading order, scale invariant, contribution to the four-wave interaction coefficient. The final six-wave interaction coefficient $\mathcal{W}_{4,5,6}^{1,2,3}$, of the LWE can be represented as a sum of three contributions:

$${}^L\mathcal{W}_{4,5,6}^{1,2,3} = {}^1\mathcal{W}_{4,5,6}^{1,2,3} + {}^2\mathcal{W}_{4,5,6}^{1,2,3} + {}^3\mathcal{W}_{4,5,6}^{1,2,3}, \quad (\text{D.1a})$$

where each term is of a different scaling with k . The exact expressions are given by

$${}^1\mathcal{W}_{4,5,6}^{1,2,3} = -\frac{1}{8} \sum_{\substack{i,j,m=1 \\ i \neq j \neq m \neq i}}^3 \sum_{\substack{p,q,r=4 \\ p \neq q \neq r \neq p}}^6 \frac{{}^1T_{p,q}^{p+q-i,i} {}^1T_{j,m}^{j+m-r,r}}{\omega_{j,m}^{j+m-r,r}} + \frac{{}^1T_{i,j}^{i+j-p,p} {}^1T_{q,r}^{q+r-m,m}}{\omega_{q,r}^{q+r-m,m}}, \quad (\text{D.1b})$$

$$\begin{aligned} {}^2\mathcal{W}_{4,5,6}^{1,2,3} &= -\frac{1}{8} \sum_{\substack{i,j,m=1 \\ i \neq j \neq m \neq i}}^3 \sum_{\substack{p,q,r=4 \\ p \neq q \neq r \neq p}}^6 \frac{{}^1T_{p,q}^{p+q-i,i} {}^2T_{j,m}^{j+m-r,r}}{\omega_{j,m}^{j+m-r,r}} + \frac{{}^1T_{i,j}^{i+j-p,p} {}^2T_{q,r}^{q+r-m,m}}{\omega_{q,r}^{q+r-m,m}} \\ &\quad -\frac{1}{8} \sum_{\substack{i,j,m=1 \\ i \neq j \neq m \neq i}}^3 \sum_{\substack{p,q,r=4 \\ p \neq q \neq r \neq p}}^6 \frac{{}^2T_{p,q}^{p+q-i,i} {}^1T_{j,m}^{j+m-r,r}}{\omega_{j,m}^{j+m-r,r}} + \frac{{}^2T_{i,j}^{i+j-p,p} {}^1T_{q,r}^{q+r-m,m}}{\omega_{q,r}^{q+r-m,m}} \end{aligned} \quad (\text{D.1c})$$

and

$${}^3\mathcal{W}_{4,5,6}^{1,2,3} = -\frac{1}{8} \sum_{\substack{i,j,m=1 \\ i \neq j \neq m \neq i}}^3 \sum_{\substack{p,q,r=4 \\ p \neq q \neq r \neq p}}^6 \frac{{}^2T_{p,q}^{p+q-i,i} {}^2T_{j,m}^{j+m-r,r}}{\omega_{j,m}^{j+m-r,r}} + \frac{{}^2T_{i,j}^{i+j-p,p} {}^2T_{q,r}^{q+r-m,m}}{\omega_{q,r}^{q+r-m,m}}, \quad (\text{D.1d})$$

where 1T and 2T are defined in equation (18a).

The three contributions of ${}^L\mathcal{W}_{4,5,6}^{1,2,3}$ given in equations (D.1), each are of different orders in kl_ξ - the small parameter arising from the long-wave limit. Therefore, ${}^1\mathcal{W}_{4,5,6}^{1,2,3} \sim \mathcal{O}((kl_\xi)^4)$ is the leading contribution to the six-wave dynamics, followed by ${}^2\mathcal{W}_{4,5,6}^{1,2,3} \sim \mathcal{O}((kl_\xi)^6)$ and finally ${}^3\mathcal{W}_{4,5,6}^{1,2,3} \sim \mathcal{O}((kl_\xi)^8)$.

The first term in expansion (D.1), ${}^1\mathcal{W}_{4,5,6}^{1,2,3}$, is generated from the coupling of the leading cubic nonlinear term, 1T , of (7) with itself. If we were to consider the 1D NLSE, then the six-wave interaction coefficient would only consist of this contribution, ${}^1\mathcal{W}_{4,5,6}^{1,2,3}$, as ${}^2T_{3,4}^{1,2} \equiv 0$. Integrability of the 1D NLSE should imply that the six-wave interaction coefficient ${}^1\mathcal{W}_{4,5,6}^{1,2,3}$ is zero when the six-wave resonance condition is satisfied. We verified that this is indeed the case by using parametrization (E.1) and utilizing the `Mathematica` package.

Therefore, the main contribution to the six-wave dynamics for the LWE arise from the second (the first non-zero) term in (D.1), ${}^2\mathcal{W}_{4,5,6}^{1,2,3}$. This contribution, with the use of (E.1), gives a \mathbf{k} -independent result:

$${}^L\mathcal{W}_{4,5,6}^{1,2,3} \approx {}^2\mathcal{W}_{4,5,6}^{1,2,3} = \frac{9\varepsilon_0^2 n_a^8 l_\xi^6 k_0^4}{16K^2}. \quad (\text{D.2})$$

We shall approximate the six-wave interaction coefficient of the LWE by the constant given by (D.2).

E. Locality of the Kinetic Equation Collision Integral

In this Appendix, we will derive the necessary criteria for the convergence of the collision integral in the KE. We will check for convergence in the limits where a combination of wave numbers diverge to infinity or tend to zero. The Dirac delta functions present in the collision integral imply that the six-wave resonance condition (A.7) is always satisfied. To make our analysis easier we will use a parametrization for the six-wave resonance condition. This parametrization is defined by making the values of two wave numbers functions of the remaining four such that the six-wave resonance condition is satisfied. This procedure leads to the parametrization:

$$\mathbf{k}_2 = \frac{(\mathbf{k}_4 - \mathbf{k})(\mathbf{k}_3 - \mathbf{k}_4)}{\mathbf{k} + \mathbf{k}_3 - \mathbf{k}_4 - \mathbf{k}_6} + \mathbf{k}_6, \quad (\text{E.1a})$$

$$\mathbf{k}_5 = \frac{(\mathbf{k}_4 - \mathbf{k})(\mathbf{k}_3 - \mathbf{k}_4)}{\mathbf{k} + \mathbf{k}_3 - \mathbf{k}_4 - \mathbf{k}_6} + \mathbf{k} + \mathbf{k}_3 - \mathbf{k}_4. \quad (\text{E.1b})$$

We begin by checking for convergence in the IR region of \mathbf{k} -space, by determining the \mathbf{k} -scaling of the KE as one wave number, say $k_6 \rightarrow 0$. Therefore, we must find the IR \mathbf{k} -scaling of each contribution in the collision integral. We will present our analysis for a general six-wave KE. So we assume that the six-wave interaction coefficient has the following scaling as $k_6 \rightarrow 0$:

$$\lim_{k_6 \rightarrow 0} \mathcal{W}_{4,5,6}^{\mathbf{k},1,2} \propto k_6^\xi, \quad (\text{E.2})$$

where $\xi \in \mathbb{R}$. Then in the same limit, the following term in the KE behaves as

$$\begin{aligned} \lim_{k_6 \rightarrow 0} n_{\mathbf{k}} n_2 n_3 n_4 n_5 n_6 (n_{\mathbf{k}}^{-1} + n_2^{-1} + n_3^{-1} - n_4^{-1} - n_5^{-1} - n_6^{-1}) \\ \propto n_{\mathbf{k}} n_2 n_3 n_4 n_5 n_6 (n_{\mathbf{k}}^{-1} + n_2^{-1} + n_3^{-1} - n_4^{-1} - n_5^{-1}) \propto n_6 \propto k_6^{-x}, \end{aligned} \quad (\text{E.3})$$

where x is the wave action spectrum exponent for $n_{\mathbf{k}}$ from (42). Thus, we can factorize out the integral over \mathbf{k}_6 in the KE and write it as

$$\int k_6^{2\xi} n_6 d\mathbf{k}_6 \propto 2 \int_0 k_6^{2\xi-x} dk_6. \quad (\text{E.4})$$

Ultimately, convergence of the KE in the IR limit corresponds to convergence of integral (E.4) as $k_6 \rightarrow 0$. Hence, convergence of the collision integral is satisfied when

$$x < 1 + 2\xi. \quad (\text{E.5})$$

Note that all other integrals over $\mathbf{k}_2, \mathbf{k}_3, \mathbf{k}_4, \mathbf{k}_5$ diverge in exactly the same manner as the integral over \mathbf{k}_6 . Moreover, we can check for IR divergence if two wave numbers are simultaneously small. When two wave numbers on the same side of the six-wave resonance sextet are small, i.e. \mathbf{k}_2 and \mathbf{k}_3 or \mathbf{k}_4 and \mathbf{k}_6 , then we see an integral proportional to the square of (E.4) - doubling the rate of divergence.

If the two wave numbers are on opposite sides of the sextet, then we get convergence because of an additional vanishing contribution arising from the term

$$\lim_{\mathbf{k}_2, \mathbf{k}_6 \rightarrow 0} (n_{\mathbf{k}}^{-1} + n_2^{-1} + n_3^{-1} - n_4^{-1} - n_5^{-1} - n_6^{-1}) \rightarrow 0. \quad (\text{E.6})$$

Total convergence and thus locality of the KZ solutions (49) is only assured if we have convergence in both IR and UV limits of \mathbf{k} -space. Therefore, we will now proceed in calculating the condition of UV convergence of the collision integral.

To check for UV convergence, we will consider the scaling of the collision integral as one wave number diverges to infinity. The conservation of momentum, implied by the Dirac delta function of wave numbers, means that if one wave number diverges, so must a second from the opposite side of the sextet⁹. This can be verified by parametrization (E.1), i.e. if we force \mathbf{k}_6 to diverge, then so must \mathbf{k}_2 . Indeed, due to this second divergence, we must integrate over the second diverging wave number and additionally compute the \mathbf{k} -scaling of the resulting Jacobian.

To begin, let us assume that the six-wave interaction coefficient scales in the following way with the diverging wave number \mathbf{k}_6 :

$$\lim_{\mathbf{k}_6 \rightarrow \infty} \mathcal{W}_{4,5,6}^{\mathbf{k},2,3} \propto k_6^\eta, \quad (\text{E.7})$$

where $\eta \in \mathbb{R}$. Due to the integration of an additional diverging wave number (in this case \mathbf{k}_2), we must consider the \mathbf{k} -scaling of the Jacobian corresponding to the transformation between \mathbf{k}_6 and \mathbf{k}_2 . The Jacobian is expressed as

$$\left| \frac{\partial \omega_{4,5,6}^{k,2,3}}{\partial \mathbf{k}_2} \right|^{-1} = \frac{1}{2|\mathbf{k} + \mathbf{k}_3 - \mathbf{k}_4 - \mathbf{k}_6|}, \quad (\text{E.8})$$

where we have used the fact that $\mathbf{k}_5 = \mathbf{k} + \mathbf{k}_2 + \mathbf{k}_3 - \mathbf{k}_4 - \mathbf{k}_6$. From equation (E.8), we observe that the Jacobian produces a contribution to the collision integral $\propto k_6^{-1}$, and moreover, we find that the following expression in the collision integral scales as

$$\begin{aligned} \lim_{\mathbf{k}_6 \rightarrow \infty} & (n_{\mathbf{k}}^{-1} + n_2^{-1} + n_3^{-1} - n_4^{-1} - n_5^{-1} - n_6^{-1}) n_{\mathbf{k}} n_2 n_3 n_4 n_5 n_6 \\ & \propto k_6^{-1-2x} (k_6^0 + k_6^{-2}). \end{aligned} \quad (\text{E.9})$$

The first term on the right-hand side is a contribution arising from the Jacobian and the product of $n_{\mathbf{k}}$ s. The second term stems from the difference of $n_{\mathbf{k}}$ s (shown in the brackets in equation (34)) giving rise to two contributions. The k_6^0 scaling results from the difference of the four non-divergent $n_{\mathbf{k}}$ s, while the k_6^{-2} factor comes from the leading order

⁹Divergence of two wave numbers on the same side of the sextet would violate the Dirac delta function involving frequencies.

Taylor expansion of the two divergent $n_{\mathbf{k}s}$. Therefore, collecting all the contributions together, we find that the condition for the UV convergence of the collision integral is given by

$$\eta < x. \quad (\text{E.10})$$

Subsequently, the overall locality region for the KZ solutions for the six-wave KE is given by

$$\eta < x < 1 + 2\xi. \quad (\text{E.11})$$

F. Derivation of the Differential Approximation Model

In this Appendix we will outline the derivation of the DAM from the KE. If one assumes that only super-local wave interactions occur, then the KE can be simplified into a differential model. The DAM will describe the evolution of the wave action density $n_{\mathbf{k}}$ in ω -space - the space determined by angle averaging over wave vectors. This results in a dimensional-independent description for $n_{\mathbf{k}}$. Consequently, the wave action density in ω -space is defined as

$$N_{\omega} = n_{\omega} \frac{d\mathbf{k}}{d\omega_k}, \quad (\text{F.1})$$

so that the total wave action is equal to

$$\int N_{\omega} d\omega = \int n_{\mathbf{k}} d\mathbf{k}. \quad (\text{F.2})$$

The KE (34), can then be re-expressed in terms of ω :

$$\begin{aligned} \frac{\partial N_{\omega}}{\partial z} &= \int S_{4,5,6}^{\omega,2,3} n_{\omega} n_2 n_3 n_4 n_5 n_6 \left(\frac{1}{n_{\omega}} + \frac{1}{n_2} + \frac{1}{n_3} - \frac{1}{n_4} - \frac{1}{n_5} - \frac{1}{n_6} \right) \\ &\quad \times d\omega_2 d\omega_3 d\omega_4 d\omega_5 d\omega_6, \end{aligned} \quad (\text{F.3})$$

where we have defined a new interaction coefficient given by

$$S_{4,5,6}^{\omega,2,3} = \left\langle \frac{\epsilon^8 \pi}{6} |\mathcal{W}_{4,5,6}^{\mathbf{k},2,3}|^2 \delta_{4,5,6}^{\mathbf{k},2,3} \right\rangle \frac{d\mathbf{k}}{d\omega_k} \frac{d\mathbf{k}_2}{d\omega_2} \frac{d\mathbf{k}_3}{d\omega_3} \frac{d\mathbf{k}_4}{d\omega_4} \frac{d\mathbf{k}_5}{d\omega_5} \frac{d\mathbf{k}_6}{d\omega_6}. \quad (\text{F.4})$$

$S_{4,5,6}^{\omega,2,3}$ has the same symmetry properties as $\mathcal{W}_{4,5,6}^{\mathbf{k},2,3}$ given in (26). The strategy in deriving the DAM from the KE is outlined in [50], and involves multiplying (F.3) by some arbitrary smooth function, $f(\omega) = f_{\omega}$, and then integrating with respect to $d\omega$. Using the symmetry of the interaction coefficient $S_{4,5,6}^{\omega,2,3}$, this procedure gives

$$\begin{aligned} \int \dot{n}_{\omega} f(\omega) \omega^{-1/2} d\omega &= \frac{1}{6} \int S_{4,5,6}^{\omega,2,3} n_{\omega} n_2 n_3 n_4 n_5 n_6 \\ &\quad \times \left(\frac{1}{n_{\omega}} + \frac{1}{n_2} + \frac{1}{n_3} - \frac{1}{n_4} - \frac{1}{n_5} - \frac{1}{n_6} \right) \\ &\quad \times (f_{\omega} + f_2 + f_3 - f_4 - f_5 - f_6) d\omega_2 d\omega_3 d\omega_4 d\omega_5 d\omega_6, \end{aligned} \quad (\text{F.5})$$

where $f_i = f(\omega_i)$, with $i = k, 2, 3, 4, 5, 6$. The super-locality assumption of wave interactions implies that each ω_i with $i = 2, 3, 4, 5, 6$ can be considered to be close to ω_k , such

that each ω_i is within a small deviation p_i of ω_k , i.e. $\omega_i = \omega_k(1 + p_i)$ for $i = 2, 3, 4, 5, 6$. This permits the Taylor expansion of the two brackets involving n_ω^{-1} s and f s around the deviations up to $\mathcal{O}(p^3)$. Furthermore, by approximating $n_\omega n_2 n_3 n_4 n_5 n_6 \approx n_\omega^6$ and using the scale invariance property of $S_{4,5,6}^{\omega,2,3}$, we gain the following equation:

$$\int \dot{n}_\omega f(\omega) \omega^{-1/2} d\omega = S_0 \int \omega^{9/2} n_\omega^6 \frac{\partial^2}{\partial \omega^2} \left(\frac{1}{n_\omega} \right) \frac{\partial^2 f}{\partial \omega^2} d\omega, \quad (\text{F.6})$$

where

$$S_0 = \frac{1}{24} \int S(1, 1 + p_2, 1 + p_3, 1 + p_4, 1 + p_5, 1 + p_6) \times (p_2^2 + p_3^2 - p_4^2 - p_5^2 p_6^2)^2 \delta_{p_4, p_5, p_6}^{p_2, p_3} dp_2 dp_3 dp_4 dp_5 dp_6. \quad (\text{F.7})$$

Then from applying integration by parts we get

$$\int \dot{n}_\omega f(\omega) \omega^{-1/2} d\omega = S_0 \int \left(\frac{\partial^2}{\partial \omega^2} \left[\omega^{9/2} n_\omega^6 \frac{\partial^2}{\partial \omega^2} \left(\frac{1}{n_\omega} \right) \right] \right) f(\omega) d\omega. \quad (\text{F.8})$$

As $f(\omega)$ is an arbitrary function, the two integrals must be satisfied for all choices of $f(\omega)$. Therefore, their integrands must equal one another. This results in the formulation of the DAM:

$$\dot{n}_\omega = S_0 \omega^{1/2} \frac{\partial^2}{\partial \omega^2} \left[\omega^{9/2} n_\omega^6 \frac{\partial^2}{\partial \omega^2} \left(\frac{1}{n_\omega} \right) \right]. \quad (\text{F.9})$$

G. The Bogoliubov Dispersion Relation

We will derive the expression for the Bogoliubov dispersion relation for the description of waves upon a condensate background. The dynamics of waves propagating in the presence of a condensate differ from the pure linear waves of the system. The Bogoliubov dispersion relation comprises of a nonlinear correction to the linear frequency that emerges due to the existence of a strong condensate. The strategy in deriving the formula for the Bogoliubov dispersion relation is to consider the expansion the wave function $\psi(x, z)$ around a homogeneous condensate background. In the most ideal situation, the condensate is represented as the dynamics of the zeroth Fourier mode. However, in reality the condensate may be described by a range of Fourier modes situated at low \mathbf{k} . For simplicity, we shall consider a perturbative expansion of small disturbances on a uniform (zeroth mode) condensate.

The condensate is described by an x -independent solution to the LWE, (7), i.e. a solution of the form $\psi(x, z) = \psi_c(z)$, where $\psi_c(z)$ is given by

$$\psi_c(z) = \psi_0 \exp(-i\omega_c z/2q), \quad (\text{G.1})$$

with $\omega_c = -I_0/2\tilde{\psi}^2 l_\xi^2$ and where $I_0 = |\psi_0|^2$ is the intensity of the condensate (zeroth mode). Solution $\psi_c(z)$ describes the background rotation of a uniform condensate in (7) with a rotation frequency of ω_c .

We expand the LWE in powers of $\phi(x, z)$, the wave function for disturbance upon the condensate, and linearize with respect to this perturbation, where we have defined

$$\psi(x, z) = \psi_c(z) [1 + \phi(x, z)], \quad (\text{G.2})$$

with $|\phi(x, z)| \ll 1$. Substituting relation (G.2) into the LWE, (7), and linearizing to the first order in $\phi(x, z)$, gives a linear evolution equation for $\phi(x, z)$. Assuming the disturbance $\phi(x, z)$ takes the form of a single monochromatic plane wave:

$$\phi(x, z) = A \exp\left(i\mathbf{k}x - \frac{i\Omega_k z}{2q}\right) + A^* \exp\left(-i\mathbf{k}x + \frac{i\Omega_k z}{2q}\right), \quad (\text{G.3})$$

where A is a complex amplitude of the wave and Ω_k is the frequency of the waves (disturbances) upon the condensate. Then by equating both types of exponentials, we can derive the dispersion relation for the propagation of weakly nonlinear waves upon the condensate:

$$\Omega_k = \sqrt{\left(1 + \frac{I_0}{\tilde{\psi}^2}\right) k^4 - \frac{I_0}{\tilde{\psi}^2 l_\xi^2} k^2}. \quad (\text{G.4})$$

To obtain the Bogoliubov frequency of the original wave function $\psi(x, z)$, we must include the frequency in which the condensate is rotating, ω_c . Therefore, the Bogoliubov dispersion relation for a weakly nonlinear wave in the presence of a condensate is given by

$$\begin{aligned} \omega_k &= \omega_c + \Omega_k, \\ &= -\frac{I_0}{2\tilde{\psi}^2 l_\xi^2} + \sqrt{\left(1 + \frac{I_0}{\tilde{\psi}^2}\right) k^4 - \frac{I_0}{\tilde{\psi}^2 l_\xi^2} k^2}. \end{aligned} \quad (\text{G.5})$$

H. Non-Dimensionalization

The dimensional models for 1D OWT contain several physical constants and parameters. For convenience and clarity, it is preferred to consider the dimensionless forms of the equations. Therefore in this Appendix, we present our non-dimensional descriptions for the LWE, (7) and the SWE, (9). We follow the non-dimensionalization that was performed in [78]:

$$\psi = (\tilde{\psi}/\sqrt{\alpha})\psi^*(x^*, z^*), \quad x^* = x/x_c\sqrt{\alpha}, \quad z^* = z/z_c\alpha \quad (\text{H.1})$$

with $\tilde{\psi}^2 = 2K/\varepsilon_0 k_0^2 n_a^4 l_\xi^4$, $z_c = 2ql_\xi^2$ and $x_c = l_\xi$. The electrical coherence length of the LC is defined as $l_\xi = \sqrt{\pi K/2\Delta\varepsilon(d/V_0)}$.

Non-dimensionalization (H.1), expresses the LWE in the form:

$$i\frac{\partial\psi}{\partial z} = -\frac{\partial^2\psi}{\partial x^2} - \frac{1}{2}\psi|\psi|^2 - \frac{1}{2\alpha}\psi\frac{\partial^2|\psi|^2}{\partial x^2}, \quad (\text{H.2})$$

where α is a tunable parameter that adjusts the strength of the second nonlinear term and for clarity we have dropped the superscripts on the non-dimensional variables. The nonlinearity of the system can be adjusted by increasing or decreasing the magnitude of the wave function $\psi(x, z)$, however, parameter α provides additional control of the ratio of the the two nonlinear terms. Indeed, the LWE was derived in a regime of a long-wave limit that implies that $(k^*)^2/\alpha \ll 1$ (where k^* is the dimensionless wave number), and therefore we must ensure that the long-wave limit it satisfied.

Similarly, we can derive a dimensionless expression for the SWE using the same dimensionless variables given in (H.1). This gives the dimensionless version of the SWE as

$$i \frac{\partial \psi}{\partial z} = -\frac{\partial^2 \psi}{\partial x^2} + \frac{1}{2} \psi \frac{\partial^{-2} |\psi|^2}{\partial x^{-2}}. \quad (\text{H.3})$$

Notice, that in (H.3) α does not appear.

I. The Intensity Spectrum

Experimentally, due to the difficulty in measuring the phase of the wave function $\psi(x, z)$, we cannot determine $n_{\mathbf{k}}$ easily. However, we can measure the spectrum of wave Intensity $N_{\mathbf{k}} = |(|\psi|^2)_{\mathbf{k}}|^2$. Theoretically, we are able to relate the k -scaling for $N_{\mathbf{k}}$ with that of the KZ solution derived from the KE, (34). In this Appendix, we present the derivation of this relationship. First, we must consider the expression for the light intensity in \mathbf{k} -space. We begin by considering the usual definition for the Fourier transform in \mathbb{R} , this implies

$$I_{\mathbf{k}} = (|\psi|^2)_{\mathbf{k}} = \int \psi(x) \psi^*(x) e^{-i\mathbf{k}x} dx, \quad (\text{I.1a})$$

$$= \int a_1 a_2^* \delta_1^{\mathbf{k},2} d\mathbf{k}_1 d\mathbf{k}_2. \quad (\text{I.1b})$$

Hence, for the intensity spectrum $N_{\mathbf{k}} = \langle |I_{\mathbf{k}}|^2 \rangle$ this gives

$$\langle |I_{\mathbf{k}}|^2 \rangle = \int \langle a_1 a_2 a_3^* a_4^* \rangle \delta_1^{\mathbf{k},4} \delta_3^{\mathbf{k},2} d\mathbf{k}_1 d\mathbf{k}_2 d\mathbf{k}_3 d\mathbf{k}_4. \quad (\text{I.2})$$

The next step is to average over phases, in a RPA wave field. This implies that only wave number pairings $\mathbf{k}_1 = \mathbf{k}_4$, $\mathbf{k}_2 = \mathbf{k}_3$ and $\mathbf{k}_1 = \mathbf{k}_3$, $\mathbf{k}_2 = \mathbf{k}_4$ will contribute to the intensity spectrum. Therefore, the intensity spectrum can be expressed as

$$N_{\mathbf{k}} = \int \langle |a_1|^2 \rangle \langle |a_2|^2 \rangle \delta^{\mathbf{k}} \delta^{\mathbf{k}} d\mathbf{k}_1 d\mathbf{k}_2 + \int \langle |a_1|^2 |a_2|^2 \rangle \delta_1^{\mathbf{k},2} \delta_1^{\mathbf{k},2} d\mathbf{k}_1 d\mathbf{k}_2 \quad (\text{I.3a})$$

$$= \left(\int n_1 \delta^{\mathbf{k}} d\mathbf{k}_1 \right)^2 + \int n_1 n_2 \delta_1^{\mathbf{k},2} d\mathbf{k}_1 d\mathbf{k}_2. \quad (\text{I.3b})$$

We will examine the intensity spectrum, when the system is in a statistically non-equilibrium stationary state and when the KZ solution is realized. Therefore, we can assume that the wave action spectrum is of the KZ form, i.e. $n_{\mathbf{k}} = Ck^{-x}$, where C is a constant determining the amplitude of the spectrum and x is the spectrum exponent. The first term of equation (I.3b) contains a Dirac delta function, centered around $\mathbf{k} = 0$. This implies that the contribution from this term will only appear at the zeroth mode¹⁰. On the other hand, the second term in equation (I.3b) will contribute on the whole of \mathbf{k} -space, and will determine the k -scaling for the intensity spectrum. The k -scaling of

¹⁰Numerically and experimentally this may be seen as a contribution at low wave numbers around $\mathbf{k} = 0$.

the intensity spectrum will only be observed if the integral of the second term is finite. We proceed by determining a sufficient condition for its convergence. We can re-express the second term by using the Dirac delta function to eliminate one of the integration variables, i.e.

$$\begin{aligned} \int n_1 n_2 \delta_1^{\mathbf{k},2} d\mathbf{k}_1 d\mathbf{k}_2 &= \int n_1 n_{1-\mathbf{k}} d\mathbf{k}_1 \\ &= C^2 \int k_1^{-x} |\mathbf{k}_1 - \mathbf{k}|^{-x} d\mathbf{k}_1. \end{aligned} \quad (\text{I.4})$$

If expression (I.4) converges on the KZ solution, then the integral will yield the intensity spectrum power-law scaling. To check for convergence, we change the integration variable to a non-dimensional variable $s = \mathbf{k}_1/\mathbf{k}$. Then, the intensity spectrum can be approximated by the integral:

$$\begin{aligned} N_{\mathbf{k}} &\approx C^2 k^{-2x+1} \int_{-\infty}^{\infty} s^{-x} |s-1|^{-x} ds. \\ &\approx C^2 k^{-2x+1} \int_0^{\infty} s^{-x} (|s-1|^{-x} + |s+1|^{-x}) ds. \end{aligned} \quad (\text{I.5})$$

Convergence must be checked in the regions where $s \rightarrow 0$ and $s \rightarrow \infty$. As $s \rightarrow 0$, relation (I.5) behaves as

$$\int_0 s^{-x} (|s-1|^{-x} + |s+1|^{-x}) ds \propto \int_0 s^{-x} ds, \quad (\text{I.6})$$

and therefore, the integral converges for $x < 1$.

In the limit when $s \rightarrow \infty$, integral (I.5) can be written as

$$\int_0^{\infty} s^{-x} (|s-1|^{-x} + |s+1|^{-x}) ds \propto \int_0^{\infty} s^{-2x} ds. \quad (\text{I.7})$$

The right-hand side of expression (I.7) converges for $x > 1/2$. Therefore, the intensity spectrum integral, (I.5), is convergent in the region:

$$1/2 < x < 1, \quad (\text{I.8})$$

where x is exponent of the power-law for the KZ solution of the KE. Experimentally at present, we can only produce the inverse cascade scenario and subsequently, we are only interested in measuring the intensity spectrum in the inverse cascade regime. The exponent of the KZ solution for the inverse cascade is given in equation (51b) ($x = 3/5$), which lies inside the region of convergence (I.8), (and so the intensity spectrum is observable) and corresponds to an intensity spectrum of

$$N_{\mathbf{k}} \propto k^{-1/5}. \quad (\text{I.9})$$

References

- [1] V. Zakharov and N. Filonenko, “The Energy Spectrum for Stochastic Oscillation of a Fluid’s Surface,” *Doklady Akademii Nauk*, vol. 170, pp. 1292–1295, 1966.
- [2] —, “Weak Turbulence of Capillary Waves,” *J. Appl. Mech. Tech. Phys.*, vol. 4, pp. 506–515, 1967.
- [3] V. Zakharov, V. Lvov, and G. Falkovich, *Kolmogorov Spectra of Turbulence I: Wave Turbulence*. Springer, 1992.
- [4] M. Onorato, A. Osborne, M. Serio, D. Resio, A. Pushkarev, V. Zakharov, and C. Brandini, “Freely Decaying Weak Turbulence for Sea Surface Gravity Waves,” *Physical Review Letters*, vol. 89, no. 144501, 2002.
- [5] S. Annenkov and V. Shrira, “Numerical Modelling of Water-Wave Evolution Based on the Zakharov Equation,” *Journal of Fluid Mechanics*, vol. 449, pp. 341–371, 2001.
- [6] —, “Role of Non-Resonant Interactions in the Evolution of Nonlinear Random Water Wave Fields,” *Journal of Fluid Mechanics*, vol. 561, pp. 181–207, 2006.
- [7] —, “Direct Numerical Simulation of Downshift and Inverse Cascade for Water Wave Turbulence,” *Physical Review Letters*, vol. 96, no. 204501, 2006.
- [8] S. Nazarenko, “Sandpile Behaviour in Discrete Water-Wave Turbulence,” *Journal of Statistical Mechanics*, no. L02002, 2006.
- [9] P. Denissenko, S. Lukaschuk, and S. Nazarenko, “Gravity Wave Turbulence in a Laboratory Flume,” *Physical Review Letters*, vol. 99, no. 014501, 2007.
- [10] S. Lukaschuk, S. Nazarenko, S. McLelland, and P. Denissenko, “Gravity Wave Turbulence in Wave Tanks: Space and Time Statistics,” *Physical Review Letters*, vol. 103, no. 044501, 2009.
- [11] —, “Statistics of Surface Gravity Wave Turbulence in the Space and Time Domains,” *Journal of Fluid Mechanics*, vol. 642, pp. 395–420, 2010.
- [12] Y. L’vov, S. Nazarenko, and B. Pokorni, “Discreteness and its Effects on Water-Wave Turbulence,” *Physica D*, vol. 218, pp. 24–35, 2006.
- [13] C. Connaughton, S. Nazarenko, and A. Pushkarev, “Discreteness and Quasi-Resonances in Weak Turbulence of Capillary Waves,” *Physical Review E*, vol. 63, no. 046306, 2001.
- [14] E. Falcon, C. Laroche, and S. Fauve, “Observation of Gravity-Capillary Wave Turbulence,” *Physical Review Letters*, vol. 98, no. 094503, 2007.
- [15] E. Falcon, S. Fauve, and C. Laroche, “Observation of Intermittency in Wave Turbulence,” *Physical Review Letters*, vol. 98, no. 154501, 2007.
- [16] C. Falcón, E. Falcon, U. Bortolozzo, and S. Fauve, “Capillary Wave Turbulence on a Spherical Fluid Surface in Low Gravity,” *Europhysics Letters*, vol. 86, no. 14002, 2009.
- [17] P. Caillol and V. Zeitlin, “Kinetic Equations and Stationary Energy Spectra of Weakly Nonlinear Internal Gravity Waves,” *Dynamics of Atmospheres and Oceans*, vol. 32, pp. 81–112, 2000.
- [18] Y. L’vov and E. Tabak, “Hamiltonian Formalism and the Garrett-Munk Spectrum of Internal Waves in the Ocean,” *Physical Review Letters*, vol. 87, no. 168501, 2001.
- [19] S. Galtier, “Weak Inertial-Wave Turbulence Theory,” *Physical Review E*, vol. 68, no. 015301, 2003.
- [20] M. Longuet-Higgins, A. Gill, and K. Kenyon, “Resonant Interactions between Planetary Waves and Discussion,” *Proceedings of the Royal Society of London A*, vol. 299, no. 1456, pp. 120–144, 1967.
- [21] V. Zakharov and L. Piterbarg, “Canonical Variables for Rossby Waves and Plasma Drift Waves,” *Physics Letters A*, vol. 126, no. 8–9, pp. 497–500, 1988.
- [22] A. Morin and L. Piterbarg, “On the Kinetic Equation of Rossby-Blinova Waves,” *Doklady Akademii Nauk SSSR*, vol. 295, pp. 816–820, 1987.
- [23] A. Balk and S. Nazarenko, “On the Physical Realizability of Anisotropic Kolmogorov Spectra of Weak Turbulence,” *JETP Letters*, vol. 70, pp. 1031–1041, 1990.
- [24] A. Balk, S. Nazarenko, and V. Zakharov, “On the Nonlocal Turbulence of Drift Type Wave,” *Physics Letters A*, vol. 146, pp. 217–221, 1990.
- [25] —, “New Invariant for Drift Turbulence,” *Physics Letters A*, vol. 152, no. 5–6, pp. 276–280, 1991.
- [26] P. Iroshnikov, “Turbulence of a Conducting Fluid in a Strong Magnetic Field,” *Soviet Astronomy*, vol. 7, pp. 566–571, 1964.
- [27] E. Falgarone and T. Passot, Eds., *Turbulence and Magnetic Fields in Astrophysics*, ser. Lecture Notes in Physics. Springer, 2003.
- [28] S. Galtier, S. Nazarenko, A. Newell, and A. Pouquet, “A Weak Turbulence Theory for Incompressible MHD,” *Journal of Plasma Physics*, vol. 63, pp. 447–488, 2000.

- [29] —, “Anisotropic Turbulence of Shear-Alfvén Waves,” *The Astrophysical Journal Letters*, vol. 564, pp. 49–52, 2002.
- [30] S. Galtier, S. Nazarenko, and A. Newell, “On Wave Turbulence in MHD,” *Nonlinear processes in Geophysics*, vol. 8, pp. 141–150, 2001.
- [31] S. Galtier and S. Nazarenko, “Large-Scale Magnetic Field Re-Generation by Resonant MHD Wave Interactions,” *Journal of Turbulence*, vol. 9, no. 40, pp. 1–10, 2008.
- [32] P. Goldreich and S. Sridhar, “Toward a Theory of Interstellar Turbulence. 2: Strong Alfvénic Turbulence,” *Astrophysical Journal*, vol. 438, no. 2, pp. 763–775, 1995.
- [33] S. Nazarenko, “2D Enslaving of MHD Turbulence,” *New Journal of Physics*, vol. 9, no. 307, 2007.
- [34] B. Bigot, S. Galtier, and H. Politano, “An Anisotropic Turbulent Model for Solar Coronal Heating,” *Astronomy and Astrophysics*, vol. 490, pp. 325–337, 2008.
- [35] A. Alexakis, B. Bigot, H. Politano, and S. Galtier, “Development of Anisotropy in Incompressible Magnetohydrodynamic Turbulence,” *Physical Review E*, vol. 78, no. 066301, 07.
- [36] J. Saur, H. Politano, A. Pouquet, and W. Matthaeus, “Evidence for Weak MHD Turbulence in the Middle Magnetosphere of Jupiter,” *Astronomy and Astrophysics*, vol. 386, pp. 699–708, 2002.
- [37] J. Saur, “Turbulent Heating of Jupiter’s Middle Magnetosphere,” *The Astrophysical Journal Letters*, vol. 602, no. 2, pp. 137–140, 2004.
- [38] W. Vinen and J. Niemela, “Quantum Turbulence,” *Journal of Low Temperature Physics*, vol. 128, no. 516, 2002.
- [39] E. Kozik and B. Svistunov, “Kelvin-Wave Cascade and Decay of Superfluid Turbulence,” *Physical Review Letters*, vol. 92, no. 3, 2004.
- [40] W. Vinen, M. Tsubota, and A. Mitani, “Kelvin-Wave Cascade on a Vortex in Superfluid He4 at Very Low Temperature,” *Physical Review Letters*, vol. 91, no. 135301, 2003.
- [41] S. Nazarenko, “Differential Approximation for Kelvin-Wave Turbulence,” *JETP Letters*, vol. 83, p. 198, 2006.
- [42] V. L’vov, S. Nazarenko, and O. Rudenko, “Bottleneck Crossover between Classical and Quantum Superfluid Turbulence,” *Physical Review B*, vol. 76, no. 024520, 2007.
- [43] —, “Gradual Eddy-Wave Crossover in Superfluid Turbulence,” *Journal of Low Temperature Physics*, vol. 153, pp. 140–161, 2008.
- [44] J. Laurie, V. L’vov, S. Nazarenko, and O. Rudenko, “Interaction of Kelvin Waves and Non-Locality of the Energy Transfer in Superfluids,” *Physical Review B*, vol. 81, no. 10, 2010.
- [45] V. L’vov and S. Nazarenko, “Spectrum of Kelvin-Wave Turbulence in Superfluids,” *JETP Letters*, vol. 91, no. 8, pp. 428–434, 2010.
- [46] L. Boué, R. Dasgupta, J. Laurie, V. L’vov, S. Nazarenko, and I. Procaccia, “Exact Solution for the Energy Spectrum of Kelvin-Wave Turbulence in Superfluids,” *Physical Review B*, vol. 84, no. 064516, 2011.
- [47] S. Nazarenko and M. Onorato, “Wave Turbulence and Vortices in Bose-Einstein Condensation,” *Physica D*, vol. 219, pp. 1–12, 2006.
- [48] —, “Freely Decaying Turbulence and Bose-Einstein Condensation in Gross-Pitaevskii Model,” *Journal of Low Temperature Physics*, vol. 146, pp. 31–46, 2007.
- [49] D. Proment, S. Nazarenko, and M. Onorato, “Quantum Turbulence Cascades in the Gross-Pitaevskii Model,” *Physical Review A*, vol. 80, no. 051603, 2009.
- [50] S. Dyachenko, A. Newell, A. Pushkarev, and V. Zakharov, “Optical Turbulence: Weak Turbulence, Condensates and Collapsing Filaments in the Nonlinear Schrödinger Equation,” *Physica D*, vol. 57, p. 96, 1992.
- [51] U. Bortolozzo, J. Laurie, S. Nazarenko, and S. Residori, “Optical Wave Turbulence and the Condensation of Light,” *Journal of Optical Society of America B*, vol. 26, no. 12, pp. 2280–2284, 2009.
- [52] A. Vedenov, *Reviews of Plasma Physics*. Consultants Bureau, New York, 1967, vol. 3, ch. Theory of Weakly Turbulent Plasma, p. 229.
- [53] R. Sagdeev and A. Galeev, *Nonlinear Plasma Theory*, ser. Frontiers in Physics. W.A. Benjamin, New York, 1969.
- [54] A. Galeev and R. Sagdeev, *Review of Plasma Physics*. Consultants Bureau, New York, 1979, vol. 7.
- [55] G. Düring, C. Josserand, and S. Rica, “Weak Turbulence for a Vibrating Plate: Can One Hear a Kolmogorov Spectrum?” *Physical Review Letters*, vol. 97, no. 025503, 2006.
- [56] S. Nazarenko, *Wave Turbulence*, ser. Lecture Notes in Physics. Springer, 2011.
- [57] F. Arechi, G. Giacomelli, P. Ramazza, and S. Residori, “Vortices and Defect Statistics in Two-Dimensional Optical Chaos,” *Physical Review Letters*, vol. 67, pp. 3749–3752, 1991.

- [58] G. Swartzlander Jr. and C. Law, “Optical Vortex Solitons Observed in Kerr Nonlinear Media,” *Physical Review Letters*, vol. 69, pp. 2503–2506, 1992.
- [59] C. Barsi, W. Wan, C. Sun, and J. W. Fleischer, “Dispersive Shock Waves with Nonlocal Nonlinearity,” *Optics Letters*, vol. 32, pp. 2930–2932, 2007.
- [60] S. Musher, A. Rubenchik, and V. Zakharov, “Hamiltonian Approach to the Description of Nonlinear Plasma Phenomena,” *Physics Reports*, vol. 129, pp. 285–366, 1985.
- [61] S. Nazarenko and V. Zakharov, “Dynamics of the Bose-Einstein Condensation,” *Physica D*, vol. 201, pp. 203–211, 2005.
- [62] C. Connaughton, C. Josserand, A. Picozzi, Y. Pomeau, and S. Rica, “Condensation of Classical Nonlinear Waves,” *Physical Review Letters*, vol. 95, no. 236901, 2005.
- [63] R. Kraichnan, “Inertial Ranges in Two Dimensional Turbulence,” *Physics of Fluids*, vol. 10, p. 1417, 1967.
- [64] —, “Inertial-Range Transfer in Two- and Three-Dimensional Turbulence,” *Journal of Fluid Mechanics*, vol. 47, pp. 525–535, 1971.
- [65] M. Anderson, J. Ensher, M. Matthews, C. Wieman, and E. Cornell, “Observation of Bose-Einstein Condensation in a Dilute Atomic Vapor,” *Science*, vol. 269, pp. 198–201, 1995.
- [66] L. Pitaevskii and S. Stringari, *Bose-Einstein Condensation*. Clarendon Press, Oxford, 2003.
- [67] S. Bose, “Plancks Gesetz und Lichtquantenhypothese,” *Zeitschrift für Physik*, vol. 26, pp. 178–181, 1924.
- [68] R. Chiao and J. Boyce, “Bogoliubov Dispersion Relation and the Possibility of Superfluidity for Weakly Interacting Photons in a Two-Dimensional Photon Fluid,” *Physical Review A*, vol. 60, pp. 4114–4121, 1999.
- [69] A. Majda, D. McLaughlin, and E. Tabak, “A One-Dimensional Model for Dispersive Wave Turbulence,” *Journal of Nonlinear Science*, vol. 6, pp. 9–44, 1997.
- [70] D. Cai, A. Majda, D. McLaughlin, and E. Tabak, “Dispersive Wave Turbulence in One Dimension,” *Physica D*, vol. 152–153, pp. 551–572, 2001.
- [71] V. Zakharov, F. Dias, and A. Pushkarev, “One-Dimensional Wave Turbulence,” *Physics Reports*, vol. 398, pp. 1–65, 2004.
- [72] A. C. Newell and J. V. Moloney, *Nonlinear Optics*, ser. Advanced Topics in Interdisciplinary Mathematical Sciences. Addison-Wesley, 1992.
- [73] N. Tabiryan, A. Sukhov, and V. Zeldovich, “The Orientational Optical Nonlinearity of Liquid Crystals,” *Molecular Crystals and Liquid Crystals*, vol. 136, p. 1, 1986.
- [74] I. Khoo, *Liquid Crystals: Physical Properties and Nonlinear Optical Phenomena*. Wiley, 1995.
- [75] E. Braun, L. Faucheux, and A. Libchaber, “Strong Self Focusing in Nematic Liquid Crystals,” *Physical Review A*, vol. 48, pp. 611–622, 1993.
- [76] M. Peccianti, C. Conti, G. Assanto, A. D. Luca, and C. Umeton, “Routing of Anisotropic Spatial Solitons and Modulational Instability in Liquid Crystals,” *Nature*, vol. 432, p. 733, 2004.
- [77] M. Peccianti, C. Conti, and G. Assanto, “Optical Modulational Instability in a Nonlocal Medium,” *Physical Review E*, vol. 68, no. 025602, 2003.
- [78] C. Conti, M. Peccianti, and G. Assanto, “Complex Dynamics and Configurational Entropy of Spatial Optical Solitons in Nonlocal Media,” *Optics Letters*, vol. 31, no. 13, pp. 2030–2032, 2006.
- [79] E. Kozik and B. Svistunov, “Scale-Separation Scheme for Simulating Superfluid Turbulence: Kelvin-Wave Cascade,” *Physical Review Letters*, vol. 94, no. 025301, 2005.
- [80] V. Zakharov, A. Pushkarev, V. Shvets, and V. Yan’kov, “Soliton Turbulence,” *JETP Letters*, vol. 48, no. 2, pp. 83–87, 1988.
- [81] B. Rumpf and A. Newell, “Coherent Structures and Entropy in Constrained, Modulationally Unstable, Nonintegrable Systems,” *Physical Review Letters*, vol. 87, p. 5, 2001.
- [82] —, “Localization and Coherence in Nonintegrable Systems,” *Physica D*, vol. 184, pp. 162–191, 2003.
- [83] B. Barviau, B. Kibler, A. Kudlinski, A. Mussot, H. Millot, and A. Picozzi, “Experimental Signature of Optical Wave Thermalization Through Supercontinuum Generation in Photonic Crystal Fiber,” *Optical Express*, vol. 17, p. 7392, 2009.
- [84] A. Eisner and B. Turkington, “Nonequilibrium Statistical Behavior of Nonlinear Schrödinger Equations,” *Physica D*, vol. 213, pp. 85–97, 2006.
- [85] R. Jordan and C. Josserand, “Self-Organization in Nonlinear Wave Turbulence,” *Physical Review E*, vol. 61, p. 1, 2000.
- [86] T. C. K.Ø. Rasmussen and P. Kevrekidis, “Statistical Mechanics of a Discrete Nonlinear System,” *Physical Review Letters*, vol. 84, p. 17, 2000.
- [87] R. Jordan, B. Turkington, and C. Zirbel, “A Mean-Field Statistical Theory for the Nonlinear

- Schrödinger Equation,” *Physica D*, vol. 137, pp. 353–378, 2000.
- [88] A. Picozzi, S. Pitois, and G. Millot, “Spectral Incoherent Solitons: a Localized Soliton Behavior in the Frequency Domain,” *Physical Review Letters*, vol. 101, no. 093901, 2008.
- [89] S. Pitois, S. Langrange, H. Jauslin, and A. Picozzi, “Velocity Locking of Incoherent Nonlinear Wave Packets,” *Physical Review Letters*, vol. 97, no. 033902, 2006.
- [90] V. Petviashvili and V. Yan’kov, “Solitons and Turbulence,” *Reviews of Plasma Physics*, vol. 14, 1987.
- [91] A. C. N. Benno Rumpf and V. E. Zakharov, “Turbulent Transfer of Energy by Radiating Pulses,” *Physical Review Letters*, vol. 103, p. 074502, 2009.
- [92] H. Talbot, “Facts Relating to Optical Science,” *Phil. Mag.*, vol. 9, pp. 401–407, 1836.
- [93] M. Berry, I. Marzoli, and W. Schleich, “Quantum Carpets, Carpets of Light,” *Physics World*, pp. 1–6, 2001.
- [94] W. Kath and N. Smyth, “Soliton evolution and radiation loss for the nonlinear Schrödinger equation,” *Physical Review E*, vol. 51, no. 1484, 1995.
- [95] M. Onorato, A. Osborne, and M. Serio, “Modulational Instability in Crossing Sea States: A Possible Mechanism for the Formation of Freak Waves,” *Physical Review Letters*, vol. 96, no. 014503, 2006.
- [96] D. R. Solli, C. Ropers, P. Koonath, and B. Jalali, “Optical Rogue Waves,” *Nature*, vol. 450, no. 1054, 2007.
- [97] N. Akhmediev, A. Ankiewicz, and M. Taki, “Waves that Appear from Nowhere and Disappear Without a Trace,” *Physics Letters A*, vol. 373, no. 675, 2009.
- [98] A. Montina, U. Bortolozzo, S. Residori, and F. Arecchi, “Non-Gaussian Statistics and Extreme Waves in a Nonlinear Optical Cavity,” *Physical Review Letters*, vol. 103, p. 173901, 2009.
- [99] A. N. Ganshin, V. B. Efimov, G. V. Kolmakov, L. P. Mezhev-Deglin, and P. V. E. McClintock, “Observation of an Inverse Energy Cascade in Developed Acoustic Turbulence in Superfluid Helium,” *Physical Review Letters*, vol. 101, p. 065303, 2008.
- [100] A. I. Dyachenko and V. E. Zakharov, “On the Formation of Freak Waves on the Surface of Deep Water,” *JETP Letters*, vol. 88, no. 307, 2008.
- [101] B. Kibler, K. Hammani, C. Michel, C. Finot, and A. Picozzi, “Rogue Waves, Rational Solitons and Wave Turbulence Theory,” *Physics Letters A*, vol. 375, no. 3149, 2011.
- [102] Y. S. Kivshar and G. Agrawal, *Optical Solitons: From Fibers to Photonic Crystals*. Academic, New York, 2003.
- [103] N. Akhmediev and A. Ankiewicz, *Dissipative Solitons*. Springer, Berlin, 2005.
- [104] O. Descalzi, M. Clerc, S. Residori, and G. Assanto, *Localized States in Physics: Solitons and Patterns*. Springer, Berlin, 2010.
- [105] E. G. Turitsyna, G. Falkovich, V. K. Mezentsev, and S. K. Turitsyn, “Optical Turbulence and Spectral Condensate in Long-Fiber Lasers,” *Physical Review E*, vol. 80, no. 031804R, 2009.
- [106] P. Suret, S. Randoux, H. R. Jauslin, and A. Picozzi, “Anomalous Thermalization of Nonlinear Wave Systems,” *Physical Review Letters*, vol. 104, no. 054101, 2010.
- [107] P. D. Gennes and J. Prost, *The Physics of Liquid Crystals*. Oxford Science Publications, 1992.
- [108] V. Zakharov and S. Manakov, “On the Complete Integrability of a Nonlinear Schrödinger Equation,” *Journal of Theoretical and Mathematical Physics*, vol. 19, pp. 551–559, 1974.
- [109] V. Krasitskii, “On Reduced Equations in the Hamiltonian Theory of Weakly Nonlinear Surface Waves,” *Journal of Fluid Mechanics*, vol. 272, pp. 1–20, 1994.
- [110] G. Boffetta, A. Celani, D. Dezzani, J. Laurie, and S. Nazarenko, “Modeling Kelvin Wave Cascades in Superfluid Helium,” *Journal of Low Temperature Physics*, no. 3-6, pp. 193–214, 2009.
- [111] V. Zakharov, “Stability of Periodic Waves of Finite Amplitude on the Surface of a Deep Fluid,” *J. Appl. Mech. Tech. Phys.*, vol. 9, pp. 190–194, 1968.
- [112] L. Biven, S. Nazarenko, and A. Newell, “Wave Turbulence and Intermittency,” *Physica D*, vol. 152/153, no. 1, pp. 520–550, 2001.
- [113] B. Rumpf and A. Newell, “Wave Turbulence,” *Annual Reviews of Fluid Mechanics*, vol. 43, pp. 59–78, 2001.
- [114] Y. Choi, Y. L’vov, S. Nazarenko, and B. Pokorni, “Anomalous Probability of High Amplitudes in Wave Turbulence,” *Physical Review A*, vol. 339, no. 3-5, pp. 361–369, 2004.
- [115] Y. L’vov and S. Nazarenko, “Noisy Spectra, Long Correlations and Intermittency in Wave Turbulence,” *Physical Review E*, vol. 69, no. 066608, 2004.
- [116] Y. Choi, Y. L’vov, and S. Nazarenko, “Wave Turbulence,” *Recent Res. Devel. Fluid Dynamics*, no. 5, 2004.
- [117] —, “Joint Statistics of Amplitudes and Phases in Wave Turbulence,” *Physica D*, no. 201, pp.

- 121–149, 2005.
- [118] S. Nazarenko and B. Quinn, “Triple Cascade Behavior in Quasi-geostrophic and Drift Turbulence and Generation of Zonal Jets,” *Physical Review Letters*, vol. 103, no. 118501, 2009.
 - [119] R. Fjørtoft, “On the Changes in the Spectral Distribution of Kinetic Energy for Two-Dimensional Nondivergent Flow,” *Tellus*, vol. 5, pp. 225–230, 1953.
 - [120] S. V. Nazarenko and A. A. Schekochihin, “Critical balance in magnetohydrodynamic, rotating and stratified turbulence: towards a universal scaling conjecture,” *Journal of Fluid Mechanics*, 2011.
 - [121] C. Leith, “Diffusion Approximation to Inertial Energy Transfer in Isotropic Turbulence,” *Physics of Fluids*, vol. 10, p. 1409, 1967.
 - [122] —, “Diffusion Approximation for Turbulent Scalar Fields,” *Physics of Fluids*, vol. 11, p. 1612, 1968.
 - [123] C. Connaughton and S. Nazarenko, “Warm Cascades and Anomalous Scaling in a Diffusion Model of Turbulence,” *Physical Review Letters*, vol. 92, no. 044501, 2004.
 - [124] S. Hasselmann and K. Hasselmann, “Computations and Parameterizations of the Nonlinear Energy Transfer in Gravity Wave Apectrum,” *Journal of Physical Oceanography*, vol. 15, pp. 1369–1377, 1985.
 - [125] R. Iroshnikov, “Possibility of a Non-Isotropic Spectrum of Wind Waves by their Weak Nonlinear Interaction,” *Soviet Physics. Dokl.*, vol. 30, p. 126, 1985.
 - [126] V. Zakharov and A. Pushkarev, “Diffusion Model of Interacting Gravity Waves on the Surface of Deep Fluid,” *Nonlinear Processes in Geophysics*, vol. 6, pp. 1–10, 1999.
 - [127] V. L’vov, S. Nazarenko, and G. Volovik, “Energy Spectra of Developed Superfluid Turbulence,” *JETP Letters*, vol. 80, p. 535, 2004.
 - [128] V. L’vov and S. Nazarenko, “Differential Models for 2D Turbulence,” *JETP Letters*, vol. 83, pp. 635–639, 2006.
 - [129] V. L’vov, S. Nazarenko, and L. Skrbek, “Energy Spectra of Developed Turbulence in Helium Superfluids,” *Journal of Low Temperature Physics*, vol. 145, p. 125, 2006.
 - [130] D. Proment, S. Nazarenko, P. Asinari, and M. Onorato, “Warm turbulence in the Boltzmann equation,” *EPL*, vol. 96, no. 24004, 2011.
 - [131] T. Benjamin and J. Feir, “The Disintegration of Wave Trains on Deep Water Part 1. Theory,” *Journal of Fluid Mechanics*, vol. 27, pp. 417–430, 1967.
 - [132] C. Connaughton, B. Nadiga, S. Nazarenko, and B. Quinn, “Modulational instability of Rossby and drift waves and the generation of zonal jets,” *J. Fluid Mech.*, vol. 654, 2010.
 - [133] B. Fornberg, *A Practical Guide to Pseudospectral Methods*. Cambridge University Press, 1998.
 - [134] C. Canuto, M. Hussaini, A. Quarteroni, and T. Zang, *Spectral Methods: Fundamentals in Single Domains*. Springer, 2006.
 - [135] A. Dyachenko, V. Zakharov, A. Pushkarev, V. Shvets, and V. Yan’kov, “Soliton Turbulence in Nonintegrable Wave Systems,” *JETP Letters*, vol. 69, no. 6, pp. 1144–1147, 1989.